STUDIES OF CELL-BIOMATERIAL INTERACTIONS AND STEM CELL DYNAMICS USING CONFOCAL/MULTI-PHOTON FLUORESCENCE MICROSCOPY AND HIGH CONTENT IMAGING BASED MODELING

By

ER LIU

A Dissertation submitted to the

Graduate School-New Brunswick

Rutgers, The State University of New Jersey

University of Medicine and Dentistry of New Jersey

Graduate School of Biomedical Sciences

in partial fulfillment of the requirements

for the degree of

Doctor of Philosophy

Graduate Program in Biomedical Engineering

written under the direction of

Prabhas V. Moghe

and approved by

_____

_____

_____

_____

_____

New Brunswick, New Jersey

January, 2011

ABSTRACT OF THE DISSERTATION

STUDIES OF CELL-BIOMATERIAL INTERACTIONS AND STEM CELL DYNAMICS USING CONFOCAL/MULTI-PHOTON FLUORESCENCE MICROSCOPY AND HIGH CONTENT IMAGING BASED MODELING

By ER LIU

Dissertation Director:

Professor Prabhas V. Moghe

A strategy in regenerative medicine involves the restitution of functional tissues using biomaterials pre-populated with transplanted cells such as human mesenchymal stem cells (hMSC). However, current design and optimization of extracellular environments to controllably promote tissue-specific regeneration are guided by empiricism, and there is a lack of structure-activity relations underlying cell-biomaterial interactions. This dissertation is focused on using high resolution confocal/multiphoton fluorescence imaging for developing quantifiable descriptors of cell-biomaterial interactions under complex microenvironments, including three-dimensional scaffolds, textural gradients of

polymer substrates, and soluble biochemical factors that stimulate differentiation or cancerous transformation.

In the first project (Chapter 2), we demonstrated the feasibility of using multiphoton imaging to quantitatively characterize microstructure of 3D biomaterial scaffolds and pseudo-3D cell morphology. This approach was further expanded, in the second project (Chapter 3), to a multidimensional space of cellular and subcellular features (termed cell descriptors) derived from: morphology, reporter protein expression, localization and spatial organization of protein reporters. Using spatially graded polymer blend substrates of both continuous roughness and discrete chemical compositions, we combined high throughput screening with high content analysis to identify both "global" and “high-content” structure-property relationships between cell adhesion and biomaterial properties such as polymer chemistry and topography.

In the next project (Chapter 4), we developed a novel molecular screening tool based on the high content descriptors of a nuclear reporter, nuclear mitotic apparatus (NuMA). Using high content imaging, data dimension reduction and machine learning techniques we mapped the nuclear features to different stem cell phenomena, specifically, stem cell lineage commitment to osteogenic versus adipogenic lineages. We reported that NuMA based nuclear descriptors captured the early lineage commitment of hMSC vs self-renewal. Moreover, a combined cytoskeletal and nuclear based “composite” profiling was demonstrated to be a robust tool to parse out not only lineage commitment vs self-renewal but within different lineages (e.g. osteogenic vs adipogenic). In the

final project (Chapter 5), nuclear feature based modeling was used to discern early subcellular changes during oncogenic transformation. The utility of this approach was demonstrated by parsing a library of synthetic polymer substrates based on their differential potential to modulate carcinogen-induced transformation of stem cells.

Acknowledgements

The road to PhD is full of failure, frustration, and frenzies. It is barely possible to walk to the finish line by myself without other people's support, not only personal but also scientific. Therefore, my sincere acknowledgements go to the following:

First and foremost, I owe my deepest gratitude to my advisor, Dr Prabhas Moghe, for his guidance, encouragement, patience and understanding during my graduate studies at Rutgers University. His mentorship provided me a valuable experience consistent with my long-term career goals. He encouraged me to think critically as a scientist and a principal investigator, as opposed to an engineer or technical specialist. I have learned to develop my individuality and communication skills in the interdisciplinary community. I am indebted to many of my colleagues who supported me on the high content profiling project: Dr. Patric Johnson, Dr. Robert Dubin, Hiral Patel, Parth Patel, Stacey Mont, Devang Patel, Hira Rizvi, Vani Mathur, Tony Kulesa, Simon Gordonov, Sebastian Vega, Joe Kim and Dr. Matt Treiser. We were a fantastic team and I really enjoy it. I would also like to thank all of the Moghe Group members past and present, with a list too long to name, it was always a great pleasure to have scientific and social interactions with them.

I would like to show my gratitude to members from Dr. Kohn's group and the RESBIO project for providing a great resource for my PhD research. Specifically, I would like to thank Dr. Kohn for providing combinatorially designed biomaterials for my research project, the utility of my research project would not

be meaningful without these polymers. I would also like to thank Dr. Matt Becker for his support for providing wonderful gradient substrates and Qdot probes, which accelerated my research pace to a great extent. My acknowledgement also goes to Dr. Hak-Joon Sung for his guidance and personal support. He acted as a mentor for me, offering endless input not only in scientific research but also in my personal life. I enjoyed our weekly research meetings over the past few years. I enjoyed going to conferences with him. It is an honor for me to thank Dr. Jared Bushman for his guidance and discussion research-wise, thanks for being a great help for the past year. More thanks go to Dr. Li Cai, who also gave me plenty of scientific and personal input on my thesis.

I would like to show my gratitude to all BME graduate students of the fall 2004 term, especially Mike Wininger, Arnold Luk, Eric Yang, Aaron Seto, Tiffany Morris, Nilay Shah, and Jessica Remboulis. I still recall the time when we spent together studying for the qualifier and playing sports. Acknowledgements are also warranted to the administrative staffs from BME and NJCBM past and present: Ursula wolf, Larry Stemberg, Linda Johnson, Robin Yarborough, Stratos Loukidis, Dr. Linda Anthony, Julia Colvin, Dr. Narayanan, Kathy Piano, and Melissa Aranzamendez.

I would also like to thank my friends, Dr. Minya Xu, Dr. Jixin Li, Yu Shi, Dr. Xin Qi, Dr. Lin Yang, all of whom have made available their support in a number of ways.

Finally, and most importantly, I am especially grateful to my family members: My wife, Wei Tong and my daughter, Jasmine Liu, who have made

my graduate life colorful and relaxing; My parents, who devoted their endless love and dedication to me since I was born and continue to give their love to my Jasmine; and my grandparents, who loved me more than anyone else. I am grateful to my “in-laws” for their support and love.

Thank you all.

Dedication

There is no royal road to science, and only those who do not dread the fatiguing climb of its steep paths have a chance of gaining its luminous summits.

- Karl Marx (1818-1883)

"Our greatest glory is not in never falling but in rising every time we fall."

- Confucius quotes (China's most famous philosopher, 551-479 BC)

This dissertation is dedicated to my grandparents who always offer endless encouragement on me, to my parents who have unconditional faith in me, to my wife and my daughter who have unlimited enthusiasm about me. This thesis would not have been possible without you.

Table of Contents

List of Tables

List of Figures

1 Introduction

1.1 Regenerative Medicine and Tissue engineering

Each year millions of people suffer from degenerative diseases which result in tissue loss and organ failure. Tissue and organ failure, caused by diabetes, heart disease, bone disease, strokes, to cancer, is a growing problem for the aging population[1,2]. The direct healthcare cost of organ replacement and assistance is more than $350 billion, including kidney dialysis, implanted replacement devices, and organ transplants. Over decades, a tremendous amounts of effort has been put into the treatment of tissue/organ failure; however, currently there is no satisfactory approach available[1,3-5]. Thus there is need for regenerative medicine that holds the promise of repairing damaged tissue and growing replacement tissues and whole organs.

Regenerative medicine, sometimes termed tissue engineering, is an emerging interdisciplinary field with applications focusing on repair, replacement or regeneration of cells, tissue or organs to restore impaired function resulting from any cause of tissue/organ damage, including congenital defects, disease, injury, trauma and aging[1-3,6]. The initial focus involved developing ex vivo creation of replacement tissues intended for subsequent in vivo implantation, for instance, skin substitutes and bone substitutes. By the start of the 21st century the emphasis on tissue replacement with ex vivo manufactured products had evolved to include strategies to induce both in vivo constructive remodeling of cell-based and cell-free scaffold materials and tissue regeneration. The

implementation of these strategies involves the use of several technological approaches in biology, material sciences, and related engineering principles that move it beyond traditional transplantation and replacement therapies. These approaches may include, but not limited to, the use of soluble molecules, gene therapy, stem cell transplantation, nanotechnology, biomaterials and reprogramming of cells[1,7-11]. These approaches allow for substantial advantages over current medicine, with the most significant impact being that regenerative medicine has the potential to provide a cure to failing or impaired tissues, thus eliminating the cost of recurring treatments for chronic disease and their subsequent complications. A wide range of diseases can benefit from regenerative medicine, including diabetes (through regeneration of islet), heart disease (through regeneration of heart), bone disease (through bone regeneration), and even cancer (via replacing the removed cancerous tissue with externally grown healthy tissue).

Despite the potential for regenerative medicine to develop revolutionary clinical therapies that will address unmet patient needs, the scientific advancement and clinical translation of regenerative medicine are still lagged behind the time line necessary for products to reach the patient bedside. The total market on tissue engineering and regenerative medicine in 2008 was less than $2 billion, and it is expected to reach $3 billion in 2010 and $4.5 billion by 2014, these statistics represents only a fraction of the potential market, with expectation of over $120 billion by 2013, and $500 billion by 2020 according to “2020-A new vision: a future for regenerative medicine” from a US NEWS 2010

September commentary. There are many hurdles that limit the current development and commercialization of tissue engineering and regenerative medicine products. These range from understanding the basic biology; to biomaterial scaffolds and matrix; to the enabling tools that will be necessary, and issues of scale-up, translation, and regulatory[1]. Funding agencies and specialized inter-agency groups have identified critical priorities for the advancement of modern regenerative medicine and tissue engineering, such as:

1) Cell sourcing and characterization.

2) Clinical understanding of cells and their interaction with microenvironment.

3) Immunologic understanding and control.

4) Enabling technologies (biomarker development, advanced imaging modalities, computational modeling and system biology).

5) Regulatory for translation and sustainable commercialization.

Among these priorities, understanding and controlling the cells and their interactions with the microenvironment and the technologies that enable monitoring cell-microenvironment interactions are the most urgently needed. Since the discovery of stem cells with potential to differentiate into multiple distinct cell phenotypes, research on the biology of stem cells (e.g. human adult stem cells, progenitor cells from various tissues, embryonic stem cells and, more recently, induced pluripotent stem cells) became a mainstream research thrust in regenerative medicine strategy for tissue regeneration. Stem cells interact actively with the microenvironment, also known as stem cell niche. The stem cell niche parameters include pH, ionic potential, nutrients, hormones, cytokine,

oxygen concentration, mechanical forces, and substrate properties, all of which are in a state of dynamic equilibrium in temporal and spatial patterns unique to each tissue and organ[12-15]. Therefore, an understanding of stem cell-niche interactions can guide the rational design of an appropriate niche for targeted tissue regeneration while eliminating undesirable behaviors such as formation of teratoma or uncontrolled cell proliferation (oncogenic transformation). To achieve this goal, screening tools that enable efficient monitoring and potentially predict stem cell-niche interactions are needed.

1.2 Bone Tissue Regeneration

Bone tissue engineering is a heavily investigated area of regenerative medicine and tissue engineering. Ten million individuals in the US are thought to already have bone-related diseases and almost 34 million more are estimated to have low bone mass[17]. It is estimated that as many as 50,000 Americans suffer from osteogenesis imperfecta, a genetic disorder characterized by bones with a poor quantity or quality of collagen that results in weak bones[18]. Patients with these diseases are susceptible to fracture and even more severe bone injury. Bone cancers, primarily osteosarcoma, are generally treated with multimodal therapeutic interventions with the combination of adjuvant chemotherapy followed by complete surgical resection of the primary tumor and any metastasis sites[19-22]. Moreover, there are other instances that call for bone replacement or regeneration such as joint replacement, spinal arthrodesis, maxillofacial surgery, and implant fixation[17,23].

Early bone tissue engineering strategy used cell-free bio-inert materials to provide temporary support. Up to now, three strategies were commonly applied in bone tissue engineering: 1) transplantation of cells, including stem cells, isolated from the patient's own or cultured from other sources; 2) the use of scaffold materials emitting biochemical signals to spur cells, especially stem cells, into action; 3) incorporation of both stem cells and biomaterials for accelerated bone regeneration processes

1.2.1 Biomaterials for bone tissue engineering—need for rational design and optimization of biomaterials

The earliest strategy for healing bone defects was transplantation of natural bone tissue using either autograft or xenograft. However, there are limited sites from which bone may be harvested without loss of function[24,25]. Moreover, disease transmission and immunologic rejection are serious concerns for autograft and xenografts[26]. Metals and ceramics have been widely used to fill a defect to provide internal fixation. However, several ongoing problems of metal implants such as fatigue, corrosion, tissue infection and poor material-tissue interface keep these metal implants from further utility. Degradable biomaterials for implants have caught intensive attention in the past thirty years. This is due to the following reasons: 1) a degradable implant does not have to be removed surgically since they degrade in the human body over time, especially in instances that only require short-term functions of the devices; 2) the use of degradable biomaterials can circumvent long-term safety issue of permanently

implanted devices. In general, there are two subdivisions of degradable biomaterials: natural and synthetic.

- Natural degradable biomaterials are those obtained from natural sources, such as animal or plant sources. The most popular natural polymers are collagen, fibrinogen, chitosan, starch, hyaluronic acid (HA), and poly(hydroxybutyrate) [27-35]. The main advantage of these natural materials is their low immunogenic potential, the potential bioactive behavior and the capability of interacting with host tissue, and chemical versatility.
- Synthetic degradable biomaterials present chemical versatility and processability based on their structure and nature. The major advantage of synthetic biomaterials over ceramics is flexibility. The mechanical and degradation properties of a polymer can be modified by composition and processing conditions. Molecular weight, hydrophobicity/hydrophilicity, crystallinity, material surface roughness and topography are variables that can be tailored for specific applications[17,36-40].

Although synthetic biodegradable polymers represent a promising alternative to current biomaterials for bone tissue engineering applications, the choice of available degradable biomaterials is still very limited. poly(L-lactic acid) (PLLA) and poly(Lactic-glycolic acid) (PLGA) are the most widely used. They are capable of delivering cells or growth factors to target tissue and they can be processed into three-dimensional scaffolds for tissue growth[23,28,36,41]. They degrade by hydrolysis into nontoxic biocompatible components, but their weak mechanical properties may not meet the needs for load-bearing applications.

There are also a few other synthetic polymers investigated for bone tissue engineering, such as: poly(propylene fumarates) (PPE), poly(phosphazenes)[21,42-46]. In addition, polycarbonates derived from the amino acid, L-tyrosine, also demonstrated great potential in bone tissue engineering applications[47].

The aforementioned polymers have demonstrated biocompatibility with relatively non-toxic and non-immunogenic degradation products and have a degradation rate comparable to the healing process of the bone wounds. However, a few issues have to be addressed for some of these degradable polymers, such as loss of mechanical strength and accumulation of acidic components during degradation process (in the case of PLGA). This stimulates the need for material optimization for controllable bone tissue regeneration. Some researchers have investigated the processing of polymeric materials by chemically modifying the surface structure, mixing with other biomaterials/biomimetic materials such as hydroxyapatitie or beta-tricalcium phosphate(β-TCP)[36,48-50], or physically rendering surface features such as surface topography and topology. However, the material design and optimization protocols in the biomaterials industry are largely based on “trial-and-error”, which makes the design of improved materials laborious and empirical. This impedes the exploration of the biomaterials feature space (chemical, physical, mechanical, etc) to fulfill specific bone tissue engineering applications. Therefore, there is a growing need for rationally designed and optimized biomaterials to promote desired bone regeneration.

1.2.2 Cell Source for Bone Tissue Regeneration

Apart from cell-free biomaterial scaffold approach, another strategy for bone regeneration is transplantation of cells. More recently, a combined strategy of cell transplantation and biomaterial scaffold has been proposed, which allows culturing osteogenic cells within three-dimensional biomaterial scaffolds under conditions supporting bone formation. Ideally, the osteogenic cell source should have the desired properties such as easy expandability, non-immunogenic, non-transplant rejection and having a protein expression pattern similar to the tissue to be regenerated. Osteoblasts and mesenchymal stem cells (from bone marrow, adipose tissue or umbilical cord blood) are the most commonly used cell source for the regeneration of bone tissues[3,4,51-65].

Osteoblasts are the immature bone cells responsible for bone matrix synthesis and subsequent mineralization. They are descendent from osteoprogenitor cells (e.g.mesenchymal stem cells). Autologous osteoblasts have been used for bone regeneration because of their non-immunogenicity. However, osteoblast cell transplantation based strategy is limited by low extraction efficiency from tissue and low expansion rates.

The use of mesenchymal stem cells for bone regeneration can be dated as early as the 1960s, when Petrakova et al. showed that implanting pieces of bone marrow under the renal capsule generated an osseous tissue[66]. In 1987, Friedenstein et al. showed that cells existing in bone marrow can differentiate to different cell types, including osteoblasts[67]. In 1991 and 1994, Caplan named them “mesenchymal stem cells (MSC)” and described that these cells, when

placed in the adequate culture conditions, could be differentiated into cells with mesenchymal origin and give rise to bone, cartilage, fat, muscle skin, tendon and other tissues (**Figure 1.1**)[68,69]. This finding spurred a spate of different studies using MSC, in combination with biomaterials, for bone tissue engineering studies. Temenoff et al. used an injectable and biodegradable polymer, oligo [poly (ethylene glycol) fumarate], as a cell carrier[70]. Rat bone marrow stromal cells were encapsulated within the hydrogel and cultured with osteogenic supplements and osteogenic differentiation was confirmed by matrix mineralization in the crosslinked hydrogels. Boo et al. reported rapid bone formation by rat bone marrow stromal cells cultured on porous HA scaffolds with osteogenic supplements[71]. They demonstrated the enhanced bone formation rate in these implants compared with that of fresh bone marrow or undifferentiated MSC. Mikos and his colleagues studied factors that can influence the osteoblastic differentiation of marrow stromal cells when cultivated on three-dimensional tissue engineering scaffolds[43,72,73]. They used a flow perfusion bioreactor to investigate hMSC cell differentiation and proliferation behavior in degradable polymer scaffolds. The bioreactor eliminates mass transport limitations to the scaffold interior and provides mechanical stimulation to the seeded cells through fluid shear. Their studies reported that scaffold properties such as pore size impact cell differentiation, especially in flow perfusion culture. In addition, the bone-like extracellular matrix created by the in vitro culture of marrow stromal cells on porous scaffolds creates an osteoinductive environment for the differentiation of other marrow stromal cell populations.

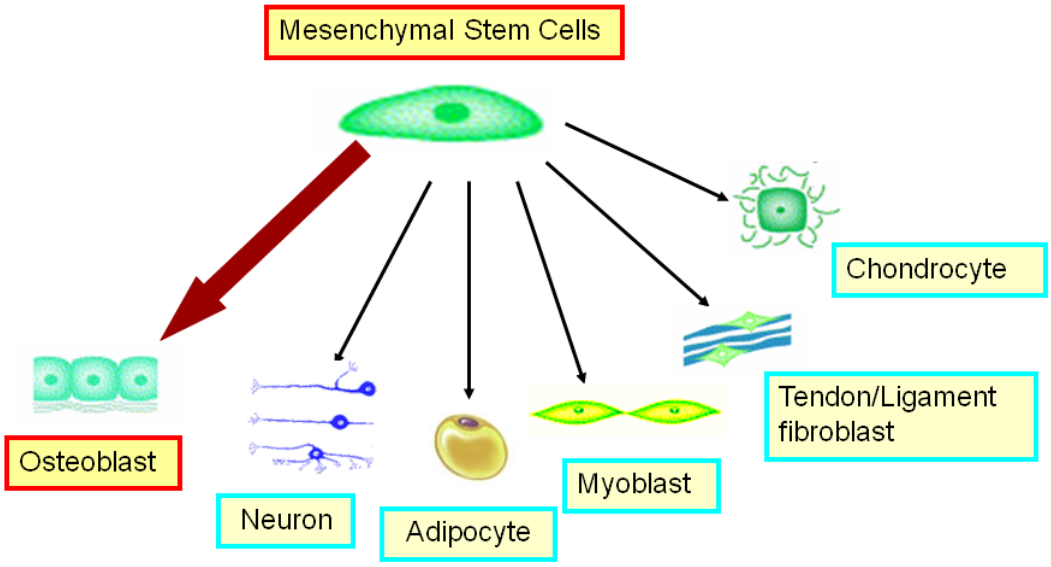

Figure 1.1: Multilineage differentiation potential of mesenchymal stem cells (MSC).

MSC are able to undergo extensive self-renewal prior to differentiation into a range of mesenchymal tissue and cell types, including bone, cartilage, muscle, tendon, and adipose. Evidence has suggested they also have the ability to differentiate into non-mesenchymal tissues including liver, heart, skin and nervous tissues.

Although the potential therapeutic aspects of MSC, especially for bone regeneration, continue to be well-researched, the possible hazards of MSC, in particular their oncogenic capacity are poorly understood. The risk for malignant transformation exists in each stage of the clinical lifecycle of MSC, including malignant transformation during in vitro expansion, during insertion of potentially therapeutic transgenes, and finally in vivo via interactions with surrounding microenvironment and tumor stroma.

Several reports of long-term cultures of bone marrow derived MSC and adipose derived MSC (≥5 months, ≥ 30 doublings) indicated changes in cell cycle kinetics and the possibility of abnormal karyotype development, leading to malignant cell transformation[33,74-79]. Moreover, biomaterials, not only metal (e.g. titanium, nickel chromium, cobalt, vanadium) but also polymers (e.g. polyethylene, aliphatic polyurethane, polyvinyl chloride, polymethylmethacrylate) were documented to induce abnormal cell transformation[80-84]. The mechanism for the stem cell transformation is not yet clear. However, numerous studies pointed out that spontaneous transformation and biomaterials induced transformation shared some of the molecular pathways, such as reactive oxygen species (ROS) mediated cell transformation mechanisms (**Figure 1.2**)[82,85,86]. It is clear that future studies need examination of the interaction and crosstalk of multiple pathways, which can further unravel the mechanism of cell transformation process at a systemic level. Taken together, these studies identified some limitations of stem cell *ex vivo* manipulation, which should be taken into consideration and explored further to ensure the biosafety of mesenchymal stem cells before clinical application.

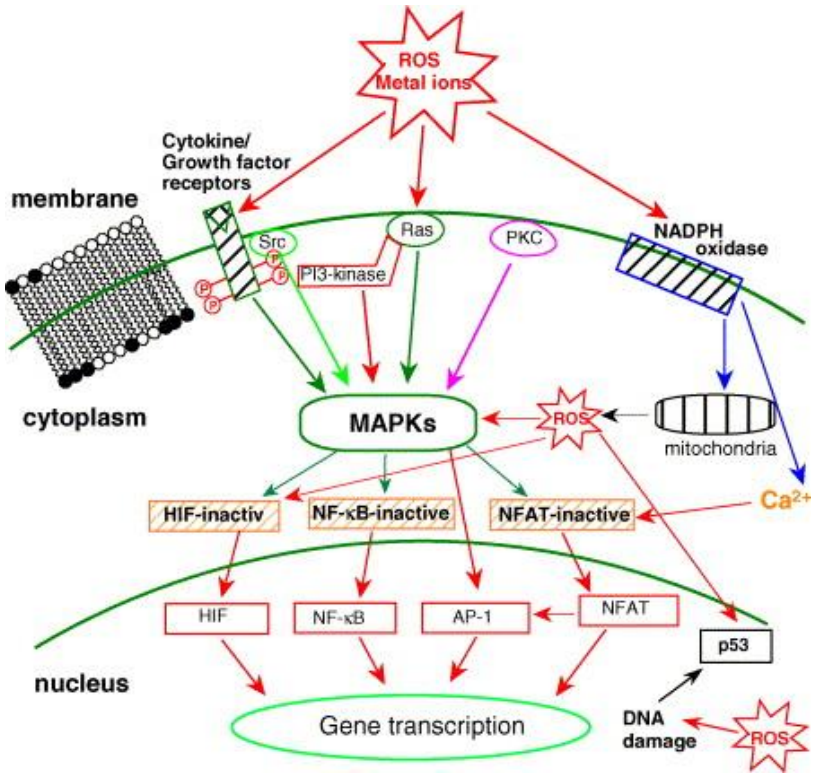

Figure 1.2: Some ROS mediated pathways for cell oncogenic transformation.

Certain growth factor receptors for EGF, VEGF, PDGF, Ras signaling, mitogen-activated protein kinases, nuclear transcription factors NF-kB, AP-1, p53, NFAT, and HIF-1 can contribute to cell oncogenic transformation by both ROS-dependent or ROS-independent mechanisms. Figure used by permission from Elsevier (Liscense number 2554441411943).

Additionally, the knowledge regarding the mechanisms and pathways that lead to the final functional differentiation in the context of biomaterial scaffolds is still scarce, thus necessitating the need for building correlations between the phenotypes of cultured cells and their potential for functional differentiation. Moreover, further investigations are also needed to understand the oncogenic

and tumor-supporting potential of MSC, especially within the context of cancer treatment.

Finally, characterization methods employed in laboratories and clinical trials to date either lack long term follow-up or adequate screening potential to detect the onset of transformation, thus calling for high content assays to efficiently identify the early events preceding state change of stem cells, which will be discussed in the next section.

1.3 Need for High Throughput / High Content Screening to Evaluate Cellular Response to Biomaterials and Various Extracellular Stimuli

Regenerative medicine, in the future, will require customizable cell/biomaterial products to meet the needs of specific individuals. The advancement of future regenerative medicine makes it necessary for scientists to investigate fundamental cellular-extracellular systems relationships and develop techniques for controllable cellular production and preservation. Therefore, the implementation of future regenerative medicine relies largely on the elucidation of stem cell responses to extracellular stimuli, including but not limited to biomaterial and soluble factors.

Biomaterials differing in chemical properties, post-processing physical properties, and geometries have been shown to cause various changes in cellular processes by way of alterations in protein adsorption, cell adhesion and spreading, and extracellular matrix production[87,88]. Parameters such as hydrophobicity, physicomechanics, architecture, and protein permissivity

represent powerful determinants of both cell function and phenotypic expression[47,89-91]. Most of the studies to date depend on traditional characterization assays and a limited number of material conditions. Moreover, some assays are qualitative and fail to capture minute changes of cellular responses. The limitation of the biomaterial property space available for traditional characterization represents a significant shortcoming as interesting cellular behaviors elicited in response to incremental but unselected experimental conditions may be overlooked.

Current trends in polymeric biomaterials discovery have evolved from the synthesis of a few potential materials to combinatorial design of biomaterial libraries[92-95]. These libraries permit the exploration of a large "property" space while simultaneously promoting the development of detailed structure-function relationships relating material parameters to cellular actions[96-98]. Advances in instrumentation for the synthesis and assembly of large polymer libraries have expanded the size and complexity of available material arrays[99]. The advantage of such sizable material test sets lies in the more thorough examination of cell-material interactions that would have otherwise gone unnoticed when investigating smaller test sets. However, the full impact of combinatorial biomaterial libraries will be realized only with the development of methods that are able to evaluate material performance on the scale of the synthesis[93]. Unfortunately, traditional approaches to the biological screening of materials are not amenable to the rapid evaluation on biomaterials of large sets and therefore, necessitate the development of novel screening approaches that can

quantitatively profile multiple cellular responses in one single experimental substrate.

One technique that garnered significant interests is the creation of single substrates with spatially resolved chemistries, roughness, and/or microstructures[100-103]. Single substrate approaches allowed for the assay of cellular response to materials of differing properties with equivalent processing conditions and faster data acquisition, thereby providing lower experimental error[104,105]. Additionally, studies which varied both chemistry and temperature and utilize gradient-based technology permitted the simultaneous study of continuous ranges of chemical and topographical properties[98,102,106,107]. These methods were potentially useful as they mapped the near complete experimental space of binary blends with roughness. The matrix of chemistries and surface physical properties further facilitated the identification of potentially new structure-function relationships that could help biomaterial scientists to rationally design materials to meet specific applications.

On the other hand, to establish cell-material relationships, it is necessary to isolate individual material parameters and their effects on specific responses. For example, previously, Bailey et al. utilized discrete binary blends of two tyrosine-derived polycarbonates, poly(DTE carbonate) and poly(DTO carbonate), respectively, and used phase separation-induced topography to determine how changes in material surface energy and roughness affect cells grown on these surfaces[100]. Zapata et al. employed continuous temperature gradients to assess osteoblast response to demixed polymer blends[102]. These

studies demonstrated that surface microstructure and topography strongly influenced cell attachment, spreading, and proliferation. One limitation highlighted by the authors in these studies was that, because the topographical features of the surface were dependent on composition and temperature, universal structure-function correlations regarding roughness, surface chemistry, and cell responses could not be readily ascertained.

Rapid screening of cell outcomes, which was generally implemented through detecting fluorescence under microscopes with low magnification objectives, may not be sufficient to denote intracellular response of cells to material cues due to the inherent low resolution of this methodology. The spatial temporal changes inside the cell as a result to biomaterial cues cannot be discerned simply through rapid screening, thus calling for high content approaches where capturing multiple intracellular responses is possible. A desirable high content screening system should enable high-resolution subcellular imaging to collect quantitative readouts from complex biological systems in addition to low-resolution high throughput screening.

The concept of “high content imaging/screening (HCS)” was originally introduced to meet the need for automation of information-rich cellular assays in the pharmaceutical industry and is now also closely associated with the implementation of large-scale cell biology research. HCS was first utilized to characterize preclinical drug candidates in pharmaceutical industry and is now integrated into all stages of contemporary drug discovery processes, including primary compound screening, post-primary screening capable of supporting

structure–activity relationships, and early evaluation of absorption, distribution, metabolism and excretion/toxicity properties and complex multivariate drug profiling[108-110]. Moreover, the growing availability of libraries of compounds and small molecules spurred widespread interests in applications to study biology systems, e.g. stem cell biology[110-112]. HCS was utilized, in combination with chemical genetics, to define protein functions and to disect signaling pathways[109]. More recently, combined with genome-wide RNA interference (RNAi) technology, HCS has allowed for probing gene function in mammalian cell culture systematically[113].

Despite these dramatic advances of HCS, a number of significant challenges remain to be addressed with regards to the utility of HCS to more biology- and disease-relevant cell systems. These challenges include the development of informative reagents/reporters to measure and manipulate cellular events, and the seamless integration of imaging modalities with data management and informatics[109,110,112,114,115].

The most widely adopted imaging modalities in high content imaging system are wide field fluorescence microscopy and confocal microscopy. Conventional fluorescence microscopy enables live cell imaging and can provide image resolution as low as 250nm. It is generally employed in intensity based screening, such as multi-protein markers expression. However, conventional epifluorescence microscopy cannot provide satisfactory high quality images for cell morphology, texture and protein localization based screening. This is due to the fact that images acquired from conventional optical microscopy are diffraction

limited. Moreover, taking surface images of 3D objects using conventional optical microcopy can often cause some degree of localized blurring of sections of images. Therefore, supplementary mathematical deconvolution processes are needed to retrieve high resolution images[116-118]. Confocal imaging modalities, including laser scanning microscopy (CLSM) and multiphoton microscopy (MPM), enable high resolution live cell imaging with 3D sectioning capabilities and are now widely used in the imaging of biological specimens, biomaterials, non-biological samples. They are potential candidates for high content imaging to investigate spatial temporal intracellular response to material features[90,117,119-123].

On the other hand, morphometric analysis of cellular response on biomaterial substrates differing in chemistry was an important aspect of the biological characterization of materials, but lacked reproducible, quantifiable results and largely remains in the domain of qualitative observations[90,103,123-127]. In the past decade, “high content” cell morphological based screening approaches were developed for the screening of potential pharmaceuticals and biologically active small molecules[82,111,128-130]. Recently, we published a technique whereby high-content CLSM/MPM imaging of cell morphology yielded a large number of quantifiable descriptors that can be used to potentially discern combinatorial variations in substrate composition[47].

One question raised from the high content screening is that what should be the appropriate molecule(s) to probe? There is no definite answer to this question yet. It varies and depends largely on applications. Generally, cell spreading, adhesion, proliferation, differentiation and transformation can be

probed through the use of a variety of reporters including whole cell reporter, subcellular reporters (e.g. cytoskeletal proteins, focal adhesion proteins), signaling molecules (protein farnesylation, Rac, Rho), and even cell nuclear proteins. What is known is cellular outcomes result from the "outside-in" signaling emanating from the extracellular microenvironment to cellular functions (differentiation, transformation, etc.), which will be discussed in the next section.

1.4 Subcellular Components as Signatures of Cellular Response

An increasing number of investigations have demonstrated that the state change of stem cells (self-renewal, differentiation and transformation) is the result of selective expression and suppression of genes, accompanied by acquisition of defined cell morphology and subcellular architecture (e.g. spatial organization of key cytoskeleton proteins), and functional/phenotypical marker expression[131-142]. Therefore, genes, proteins, and even larger scale markers can all be the candidate for screening purposes.

Previous studies showed that gene expression profiles associated with a particular cell type during state change did not only include genes primarily or solely expressed in that tissue. Among differentiation-specific genes were genes responsible for the changes in cellular morphology (e.g. genes coding for adhesion molecules and cytoskeleton proteins) necessary for tissue differentiation[143,144]. It was also found that a number of genes that are transcriptionally altered fell into six categories including: cell and tissue structure dynamics, cell cycle and apoptosis, intercellular communication, metabolism and

regulation of gene expression. In some of these categories, especially the categories of cell and tissue structure genes (e.g. integrins, keratins, and actin), gene expression changes were correlated to morphological modification. Thus, the state change of stem cells required the regulation of genes necessary to achieve a particular type of morphology, as well as genes necessary to assure the specific functions of that cell phenotype. One interesting finding during these studies was that precursor cells appeared to already contain uniquely expressed genes, suggesting that signaling pathways that were important for the differentiation of these particular cells are in place early-on[64,134,143,145].

At the protein level, a continuous link between cell adhesion complexes responsible for the cell's interaction with extracellular components, the cytoskeleton and the nuclear structure were extensively studied[90,126,135,138,139,146-151]. Cells physically bind to the extra cellular matrix (ECM) by making contact with specific ECM molecules via cell membrane receptors (**Figure 1.3a**). ECM induces changes in cellular morphology and signaling resulting from soluble molecules. The ECM is composed of a meshwork of fibrillar molecules such as collagens, elastin, and glycoproteins (e.g. fibronectin, laminin, and hydrophilic proteoglycans). Cell-ECM adhesion elicits intracellular signaling that can be divided into biochemical signal transduction (via phosphorylation cascades and protein translocation to the cell nucleus) and mechano-transduction (via cytoskeleton rearrangement)[152,153]. Mechano-transduction is also activated upon ECM-induced modification of cell shape, in which case actin is considered to be an essential part. Mechanical forces are transmitted to the cell nucleus via

envelope proteins such as nesprin that couple the cytoskeleton and chromatin. By interacting with different cytoskeleton networks, these nuclear envelope protein complexes link the ECM, the cytoskeleton and the cell nucleus[148,149]. A nuclear protein, emrin also exists in the mechano-transduction between nucleus compartment and cytoskeleton. It bridges the actin cytoskeleton and the nuclear actin polymer via the lamina, made of intermediate filament proteins lamin A/C and lamin B, thus providing tension forces within the cell nucleus[152,154-157]. Some other studies also showed that nuclear lamina contributed to chromatin organization; as a result, some regions were associated with transcriptional silencing state.

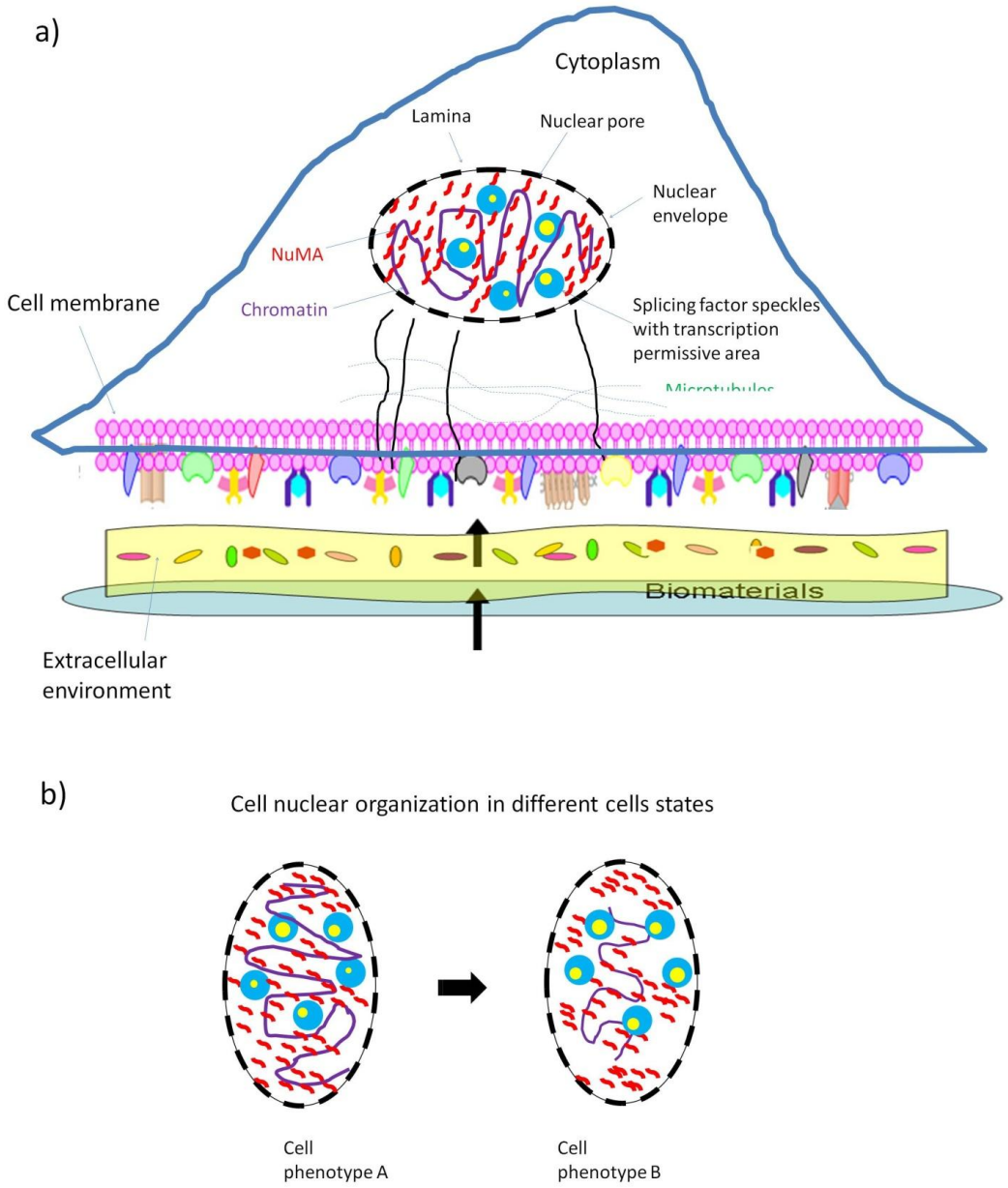

Figure 1.3: Cellular responses to extracellular stimuli.

A) Schematic of cellular response to extracellular stimuli. Cell membrane receptors recognize small molecules from extracellular matrix, and then pass the information into cell nucleus through various signaling events. **B)** Cell nuclear structure and organization of different cell phenotypes.

The study of the inner organization of the cell nucleus is emerging as a critical avenue to further understanding of controllable stem cell differentiation and transformation. Many of the compartments of the cell nucleus (e.g. nucleoli, the higher organization of chromatin into heterochromatin and euchromatin regions, non-chromatin domains) have been identified to be important in stem cell state change, especially differentiation[156,158-164]. Some of the nuclear organizational features of the cell nucleus were observed in the nuclei of non-differentiating cells, like the concentration of heterochromatin at the nuclear periphery and the presence of transcription permissive areas around splicing factor speckles (**Figure 1.3b**). However, a specific organization of the cell nucleus, including chromatin and nonchromatin regions, was also observed upon phenotypically normal differentiation (**Figure 1.3b**). The major characteristics reported so far, regardless of tissue phenotype, were the concentration of heterochromatin domains around a central nucleolus and at the nuclear periphery, DNAase sensitive chromatin at the nuclear periphery, and the formation of large and fewer splicing factor speckles compared to non-differentiated cells[148,158,164]. Sophie and her group members accessed the impact of nuclear organization on differentiation by directly altering elements that contribute to such nuclear organization in differentiated cells[131,165-167]. They demonstrated that nuclear organization is important for the maintenance of breast acinar differentiation by altering directly the organization of a nuclear protein, nuclear mitotic apparatus (NuMA), using peptides and antibodies targeted against this protein. NuMA is a cell nuclear matrix protein first described

to have an exclusively nuclear localization in interphase cells but to associate with the spindle poles during mitosis. Moreover, the cell differentiation phenotype and oncogenic status can be captured through the NuMA protein expression and spatial organization features. Altering NuMA organization in breast acinar cells led to the loss of differentiation capability. Likewise, when NuMA was silenced during differentiation, glandular differentiation was not achieved. The action on NuMA was accompanied with drastic changes in chromatin structure, as shown by the redistribution of histone acetylation and histone methylation patterns, prior to phenotypic changes.

As of now, extracellular stimuli, subcellar morphology and organization, and transcription factors, which all contribute to the modulation of gene expression in the cell nucleus, are likely to converge on the nuclear mechanisms, making study of the inner organization of the cell nucleus critical for the understanding of gene expression control during stem cell differentiation. The factors that trigger nuclear reorganization have yet to be fully indentified. Further investigations are needed to fully understand how extracellular stimuli (e.g. mechanical, biological and biochemical stimuli) converge on the cell nucleus and integrate to alter stem cell response (differentiation, transformation), although it is difficult to identify specific factors that trigger the changes. For instance, in MSC differentiation, a number of molecules that participate in biochemical signaling cascades can be activated upon mechanical stress such as Rho-GTPases altering the actin and intermediate filament cytoskeleton networks via activation of secondary messengers that additionally modify a variety of signaling pathways. However,

the ability to quantitatively capture nuclear features during stem cell state change can bridge the understanding of the contribution of nuclear organization to differentiation and further help delineating correlations of epigenetic control of gene expression and stem cell differentiation.

1.5 Hypothesis and Thesis Aims

The motivation of this dissertation is to address some of the critical priorities in the advancement of regenerative medicine, such as the need to rationally design and optimize the stem cell-niche/biomaterial interactions behavior and lack of rapid quantitative bio-relevant evaluation of stem cell responses (self-renewal, differentiation, transformation). In this thesis, it is proposed that a high content cell imaging based composite profiling platform enables quantitative evaluation of biomaterial scaffolds, characterization and prediction of stem cell fates in response to soluble factors and biomaterials. This high content imaging based platform will characterize cellular response to combinatorially designed biomaterials and soluble factors that are involved in the modulation of cell behavior. This profiling platform captures not only quantitative features of 3D biomaterial scaffolds, but it captures the subcellular features from the whole cell, including the cytoskeleton and the cell nucleus/nuclear proteins. Furthermore, it identifies the correlation between these subcellular features to cell behavior to various extracellular stimuli.

It was observed that some organizational features of cells, especially in the cell nucleus are representative of stem cells undergoing differentiation or

transformation. Based on these observations, it has been proposed that the specific nuclear organization observed in differentiated cells might be important to lock gene expression in place by maintaining genes in a silent state, enabling the expression of a small number of genes necessary for state change. The overall hypothesis of this study is that subcellular features of cells provide a composite signature that serves as an early marker of stem cell phenotypic changes such as lineage commitment, transformation. In this dissertation, the major interest is human mesenchymal stem cell differentiation and transformation. This dissertation will develop cell descriptors for high content profiling stem cell responses and demonstrate the utility of this platform through the following three aims:

1. To develop a confocal/multiphoton imaging based characterization platform to identify microstructure descriptors of 3D biomateirial scaffolds.
2. To develop a high content, quantitative, cell-descriptor-based screening methodology to evaluation cell responses and applications to combinatorially designed chemistry and roughness gradient substrates.
3. To extend the “high content” imaging based profiling platform to identify long term stem cell differentiation and transformation. Further determination of early predictability of the nuclear descriptors of stem cells in response to various extracellular stimuli.

2 Development of Quantitative Platform for Screening Cellular Response in 3-D Scaffolds

Note: This chapter is reproduced from the following publication:

Er Liu, Matthew D. Treiser, Patrick A. Johnson, Parth Patel, Aarti Rege, Joachim Kohn, and Prabhas V. Moghe. 2007. Quantitative biorelevant profiling of material microstructure within 3-D porous scaffolds via multiphoton fluorescence microscopy. 2007. J Biomed Mater Res B Appl Biomater. 82(2):284-97.

2.1 Introduction

Numerous studies document the role of three-dimensional porous polymer scaffolds for tissue engineering by serving as substrates for induction of cell activation, preservation of tissue density volume, provision of temporary mechanical function, and organization of new tissues[168-173]. The morphology and micro-architecture of a scaffold, once implanted, can influence the rate of cell growth, migration, morphogenesis, and transport of nutrients, which can alter the overall tissue functions[174]. In the past two decades several specialized techniques have been developed to produce hierarchical 3-D scaffolds to attain desired mechanical function and mass transport properties. These techniques include solvent casting/particulate leaching[175], gas foaming[176], fiber meshes/fiber bonding[177], phase separation[178], melt molding[179], emulsion freeze drying/freeze drying[180], solution casting[181], computational topology design[182], and solid free-form fabrication[171]. Consequently, there is an increasing need for

complementary techniques to visualize and quantify local scaffold microstructure and to correlate these to cell growth, attachment, and migration within the scaffold. While the structure and functionality of 2-D substrates or surfaces of 3-D scaffolds continue to be extensively studied[183-190], robust and efficient imaging techniques for mapping cell-material interactions within 3-D scaffolds non-invasively are limited.

The conventional methods for the indirect characterization of scaffold microstructure are mercury intrusion porosimetry (MIP), while direct imaging approaches include scanning electron microscopy (SEM), light microscopy & confocal microscopy, micro-computer tomography (MicroCT) and optical coherence microscopy[191-193]. Scanning electron microscopy can provide surface topography of the scaffolds on the scale of few nanometers[190]. Longitudinal and transverse sections can be easily visualized to reveal the microstructure of the scaffold[189,194,195]. There are also methodologies to render 3D images acquired from SEM[196]; however, it is neither amenable to real-time imaging nor quantitative analysis[197]. Contrastly, the real-time quantitative microstructural study of biodegradable tissue analog scaffolds was accomplished using direct imaging based on confocal laser scanning microscopy (CLSM)[198],multiphoton microscopy[199], micro-computerized tomography (MicroCT)[184,200-204] and optical coherence microscopy (OCM)[191-193].

None of the above reviewed techniques alone can satisfactorily provide non-invasive three-dimensional sections of images with a resolution of less than one micrometer. Typically this requires characterization based on two or more

techniques. For example, a combination of SEM and mercury intrusion porosimetry was used to characterize porous micro-particles[195] and scaffolds[189,205]. MicroCT was used to study the micro-architectural and mechanical characterization of oriented porous polymer scaffolds[206]. An interesting study that combined multiple techniques of SEM, MIP, CLSM and MicroCT was applied to evaluate the microstructure of PLGA scaffolds using carbon dioxide as a solvent[194]. Cartmell et al. utilized microCT and histological staining to perform quantitative analysis of mineralization within 3D scaffolds in vitro[207]. Similarly, OCM was utilized for characterizing tissue engineering medical products[191-193,208]. OCM, as a confocal technique enhanced by interferometric rejection of out-of-plane photon scattering, can image composites with a thickness of < 1 cm with high spatial resolution (1mm). It's a good tool for cell/scaffold structure imaging; however, cell function imaging may not be accessible unless combined with fluorescence CLSM imaging. Confocal microscopy has been utilized in situ for the assessment of cell viability and 3D cellular morphology within biodegradable polymer matrices[188,209,210]. CLSM is now widely used in the imaging of biological specimens, biomaterials, as well as non-biological samples[211-213]. Although CLSM is an attractive imaging modality it has several significant draw backs including: photobleaching and phototoxicity of the image probe, fast signal attenuation rate with regard to penetration depth of the sample[214-217], and the large degree of internal scattering, particularly within three-dimensional tissue/material specimens.

Multiphoton microscopy is regarded as an alternative to CLSM in visualizing tissue explants and living biological samples because of the deeper optical penetration (2-3x of confocal microscopy) with less photobleaching and phototoxicity, enhanced spectral accessibility and flexibility[218-220]. The term MPM encompasses two photon excitation microscopy, three photon excitation microscopy, second harmonic generation multiphoton microscopy, and third harmonic generation multiphoton microscopy[221,222]; all based on nonlinear excitation to generate fluorescence limited within a thin raster-scanned plane. With the advent of ultrafast (femto-second pulsed) lasers, such as Ti:Sapphire laser and Nd:YLF laser[223,224], multiphoton microscopy (MPM) has become a viable tool to monitor complex biological samples.

The present study focuses on comparing MPM with traditional CLSM/SEM technologies for the characterization of the macro and microstructure of porous, biodegradable polymer scaffolds and cell-scaffold interactions. In this study, we utilized two new tyrosine-derived polycarbonates (**Figure 2.1**) for scaffold fabrication. These two polymers, referred to as poly(DTE carbonate) and poly(DTO carbonate) form immiscible, phase-separated blends[225,226]. Depending on the blend composition, cells growing on these scaffolds are exposed not only to different surface compositions, but also to changes in the scaffold's pore architecture. These variations provide a challenging test system for the imaging of cell-scaffold interactions. Although the polymers are weakly auto-fluorescent, we found that contrast and image quality can be significantly enhanced by doping the polymer matrix with a minute quantity of a hydrophobic

fluorescent marker prior to scaffold fabrication. The resulting fluorescent scaffolds greatly enhanced the quantitative analysis of scaffold architecture. In addition, cell organization, morphology, and cytoskeleton distribution were imaged locally within a scaffold using genetically engineered fluororeporter cells. These studies demonstrate the unique advantages as well as the viability of MPM as an imaging modality for the non-invasive, real-time profiling of cell-substrate characterization in 3-D constructs in comparison to conventional imaging techniques (e.g. CLSM and SEM).

2.2 Materials and Methods

2.2.1 Polymeric Scaffolds

Biomaterials used in this study were from the family of tyrosine-derived polycarbonates synthesized utilizing previous published procedures[97]. Polymers derived from desaminotyrosyl tyrosine alkyl ester monomers were named poly(DTR carbonate)s with R = ethyl (E) or octyl (O). Copolymers of *x* mole% desaminotyrosyl tyrosine alkyl ester with *y* mole% desaminotyrosyl tyrosine with a free acid (DT) and *z*% Poly(ethylene glycol) (PEG) blocks of 1000 units were identified as poly(*x*%DTE-co-*y*%DT-co-*z*%-PEG_{1000} carbonate). In this study, five types of scaffolds were fabricated, including scaffolds made of pure poly(DTE carbonate) and poly(DTO carbonate) (see chemical structure in **Figure 2.1**), as well as scaffolds made of different poly(DTE carbonate)/poly(DTO carbonate) weight ratio blends (70%:30%), (50:50%), and (30%:70%). The analysis of the polymer composition and surface characterization were performed using

established procedures. Porous polymer sponges were fabricated by a combination of liquid-liquid phase separation, freeze drying and particulate leaching. The polymer solution was prepared by mixing 300 mg of polymer, 300 uL of nanopure water, 3 mL of 1,4 Dioxane (Sigma-Aldrich Inc., anhydrous, 99.8%) and 10 uL of Texas Red indicator dye (Sigma Genosys:GE-TXRD100, Fisher Scientific. USA) in a vortex mixer. The vial was sealed with parafilm during mixing, to avoid solvent evaporation. Once a homogeneous solution was obtained, 11 g of sodium chloride (size 212 um to 425 um) was placed in a Teflon Petri dish and the polymer solution was slowly poured over the salt and kept undisturbed for 1 h to allow for the penetration of the viscous polymer solution throughout the bed of salt. The mixture was then rapidly cooled in liquid nitrogen for 5 –10 min and was dried overnight in a freeze drier. The dried polymer scaffold was carefully punched into 8 mm-diameter by 5mm-height cylinders for imaging purposes. The cylinder-shaped scaffolds were incubated and rinsed with nanopure water at least 7 times until the silver nitrate test was negative, indicating that absence of chloride ions in the washings. The scaffolds were maintained under vacuum for 24-48 h and then stored in an 8-well plate sealed with tin foil to protect them from light and dust.

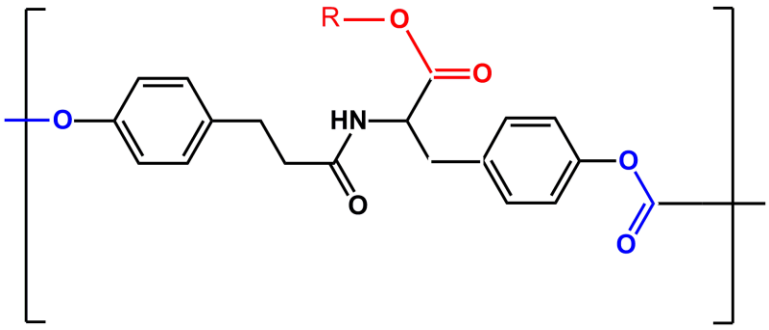

Figure 2.1: General chemical structure of poly (DTR carbonate).

The pendent R groups of the polycarbonates consist of either ethyl or octyl esters, corresponding to poly (DTE carbonate) or poly (DTO carbonate), respectively. A wide range of compositions were used in this study, ranging from 100 to 0%, 70 to 30%, 50 to 50%, 30 to 70%, and 0 to 100% combinations of poly (DTE carbonate) and poly (DTO carbonate).

2.2.2 Cell Culture and Scaffold Seeding

A Green Fluorescent Protein (GFP)-fibroblast (extracted from a GFP engineered rat) cell line was used as a model cell line to probe the morphology and organization of cells cultured within the scaffolds. GFP-fibroblast cells were cultured in Dulbecco's Modified Eagle Medium (Mediatech Inc., Herndon, VA) supplemented with 5% FBS, 1% Penicillin-streptomycin/ 1% L-glutamine. The porous scaffolds were first sterilized by exposure to UV light in a Spectro XL-1500 UV Crosslinker (Spectronics Corporation) for 15 min and kept immersed in the DMEM medium for 60 min in tissue culture plates or the imaging chamber prior to cell seeding. A 12 mL GFP-fibroblast cell-medium suspension with a density of 200,000 cells/mL was seeded into the scaffold by pumping the cell suspension through the scaffold at least seven times at 3 mL/min infusion/refill rate using a Remote Infusion/Withdrawal PHD 22/2000 Syringe Pump (Harvard Apparatus Inc) at room temperature. This technique produced relatively uniform distributions of cells within the scaffolds.

2.2.3 Imaging Methods of Scaffold Microstructure and Cellular Dynamics

Multiphoton Microscopy (MPM) and Confocal Laser Scanning Microscopy (CLSM)

Multiphoton imaging was performed on a Leica TCS SP2 system (Leica Microsystems, Inc., Exton, PA). The polymer scaffolds were placed on a cover-glass bottom microwell dish (MatTek Corp., Ashland, MA) and illuminated using a titanium: sapphire femtosecond laser with a tunable wavelength from 780 nm to 920 nm (Mai Tai, repetition rate80Mhz, 100 fs pulse duration, 800 mW). Texas Red-dyed scaffolds were imaged at 10x and 63 x magnifications, 890 nm two photon excitation, and 572.5-647.5 nm emission. A HC Plan APO CS 10x/0.4 air lens was employed for imaging macro pores, while an oil immersion type HCX Plan APO CS 63x/1.3 glycerol immersion lens was used to obtain micro pore images. Images were acquired for each sample at 0.7, 1 or 5 um intervals along the vertical axis (z-axis). 10x and 63x images were taken at depths of 250um and 60-75um respectively. For cell adhesion and spreading imaging, another 500-550 nm band-pass filter channel was used to detect GFP emission parallel to the 572.5-647.5 nm band-pass filter channel for detecting Texas Red emission only. For comparison with conventional 1-photon excitation methods, single photon confocal images were acquired using a 488-nm and 594-nm excitation with a 500-535nm and 600-700nm emission channel respectively. All image frames underwent two line and frame averaging.

Scanning Electron Microscopy

The pore structure and morphology of the polymeric scaffolds were validated using scanning electron microscopy on an AMRAY1830 microscope. Scaffold samples were dried, sectioned, and sputter-coated for scanning electron microscopy. Details of accelerating voltage, magnification and working distance are noted on the bottom of the corresponding SEM micrographs.

2.2.4 Image Analysis

Fluorescence Signal to Noise Ratio Calculation

Maximum signal to noise ratio (SNR) was calculated for qualitative evaluation of the effectiveness of single photon CLSM and MPM. To this end, multiphoton and confocal images were processed with ImageJ freeware (NIH USA, V1.37a). The CLSM and MPM images were imported within ImageJ and transformed into a pseudo-stack. Three brightest regions of interest (ROIs) of 1000 pixels each were designated as noise-free areas, and three darkest ROIs represented area of background. The average pixel intensity and standard deviation for CLSM and MPM images were measured. The SNR values were calculated as follows:

$$SNR = 20 \times \log\left(\frac{A_{signal}}{A_{noise}}\right) \qquad \text{(Equation 2-1)}$$

In this equation A_{signal} and A_{noise} are the root mean square amplitudes of the signal and the noise, respectively.

3D image Reconstruction

Images acquired through multiphoton microscopy were processed with a combination of commercially available and freeware software. The sequential

analysis was conducted as follows. First, 3-D maximum projection and 3-D view of image stacks were performed using a Leica TCS SP2 microscope; subsequently, raw images were exported to Image Pro Plus (Version 5.1 for windows, Media Cybernetics, Inc. MD.USA) for image analysis. Data resulting from that analysis were used to quantify the properties of scaffold void regions. All further analysis was implemented in Matlab 7.0 (The MathWorks Inc., MA).

Quantitative Image Based Feature Extraction

The methodology of analyzing the scaffold microstructure is shown schematically in **Figure 2.2**. The image slices first underwent image enhancement optimization (image contrast, brightness and gamma value adjusting) to highlight the contrast of void/pore area to the scaffold backbone (**Figure 2.2b**). These contrast enhanced images were then low-pass filtered (e.g., Gaussian filter, average filter or non-linear filters applied to the raw image) to reduce high frequency noise (**Figure 2.2c**). The smoothed images then underwent an adaptive thresholding process in which the 2D image stacks were thresholded according to a base value and the values beneath a moving mask of radius N. This segmentation technique converted an intensity image to a binary image where “object” or “background” was represented as a Boolean variable “1” or “0” respectively.

Morphological operations (e.g., erosion, dilation, opening) were applied to the binarized images to smooth object contours and break narrow connected structures (**Figure 2.2e**). The binarized image was subjected to size filters for sieving misrecognized voids/pores or noncontiguous speckles in the frame

(**Figure 2.2f**). Further, a median filter was applied to extremely bright spots/points (**Figure 2.2g**). This was accomplished by replacing the center pixel within a square/rectangular neighborhood by the median value of the neighborhood. Thus, the filtering step counted the number of white and black pixels in the neighborhood and assigned the median value to the pixel. Individual objects (pores) within the image frame were then labeled and stored in an excel spread sheet with selected features of each pore/void: (1) the area of the pore, (2) the perimeter of the pore, (3) major axis and minor axis of the ellipse equivalent to the object(an ellipse with the same first and second order moments of inertia as the pore), (4) the mean diameter of the circle with the same geometric moment of inertia(area) as the pore, (5) angle of primary axis of the ellipse to the horizontal axis. The strut size characterizations were done manually by drawing a straight line between pores using Leica LCS Lite (Leica Microsystems Inc., Exton PA).

Porosity analysis was performed using both visual assessment and quantitative morphometry located in a region of interests (three ROIs: 400 by 400 pixels of pore images were randomly chosen) following image segmentation using Image Pro. After the image processing steps, the pores were recognized as binary images and porosity was calculated as the void area/ (void area+strut area). The pore interconnectivity analysis was performed using ImageJ software (version 1.37a, NIH). The image stacks were first read in as 3-D slice series and subjected to image enhancement and smooth filtering, similar to the steps described in **Figure 2.2**. The segmentation process was performed using a 3D

adaptive thresholding plug-in (Adaptive 3DThreshold_.java, v 1.22, per Christian Henden and Jens Bache-Wiig).

The binarized 3-D stacks were inverted and subjected to 3-D object counting (courtesy Fabrice Cordelières, Institut Curie, Orsay, France), another ImageJ plug-in that counts the number of 3-D objects in a stack and displays the volume, the surface, the center of mass and the center of intensity for each object. Thus, the total number of objects recognized in 3-D image stacks was determined. Similar object counting can be done with a single collapsed image along the vertical axis of the 3-D stacks of the scaffold (Z-projection image) using the algorithm described in **Figure 2. 2**. If all the pores were interconnected in the 3-D stack, the number of 3-D objects recognized in the image stacks should be one. If no pores were interconnected in the 3-D stack, the number of objects recognized in 3-D image stacks should equal to number of objects recognized in the Z projection images. The following equation gave a calculation of pore interconnectivity.

$$Interconnectivity = 1 - \frac{\#objects\ \ recognized\ \ \ in\ 3D\ image\ \ stacks - 1}{\#objects\ \ recognized\ \ \ in\ Z\ projecti\ \ on\ images} \qquad \text{(Equation 2-2)}$$

Imaging of Cell Organization and Morphology in Scaffolds

The biorelevant profiling capabilities of MPM were examined by (a) comparing image contrast for cells within scaffolds using both multiphoton and single photon confocal laser scanning microscopy (CLSM); and (b) quantifying cellular morphology within the scaffolds as a function of the underlying polymer composition.

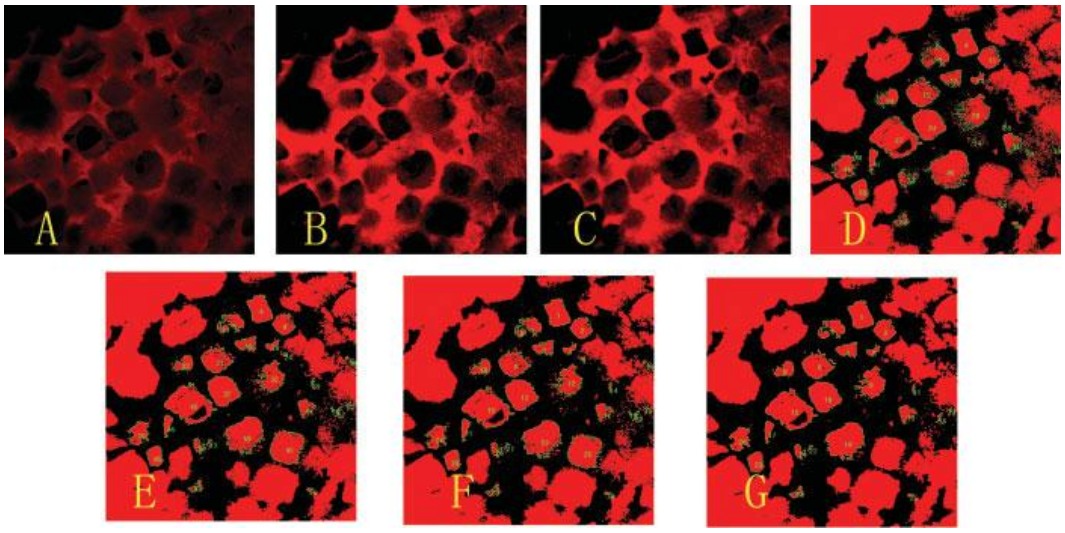

Figure 2.2: Methodology of sequential processing of images obtained by multiphoton microscopy for quantitation of polymeric scaffold microstructure.

(A) Raw image slice, 1024 by 1024 pixels in size, obtained by imaging poly(DTR carbonate) scaffolds stained with Texas Red through excitation at 594nm, and signal collection at 605-700nm; **(B)** Contrast enhanced image; **(C)** Low pass filtered image; **(D)** Binarized image; **(E)** Morphologically filtered image (open); **(F)** Size filtered image; **(G)** Final void distribution

Utilizing conventional CLSM and MPM, GFP engineered rat fibroblasts were imaged after seeding within the porous scaffolds fabricated from poly(DTE carbonate)/poly(DTO carbonate) blend. The clarity of cell visualization against the polymer substrate was compared for MPM versus CLSM. The ability of CLSM and MPM to discern the underlying microstructural details of the polymer substrate was compared.

The three-dimensional morphology of GFP-fibroblasts was analyzed based on the maximum intensity projection of image stacks obtained via multiphoton fluorescence microscopy. Cell morphology was characterized in terms of cell area, A, perimeter, P, and shape factor, ∅, which describes the morphologic polarization of the cell defined as $\emptyset = \frac{P^2}{4\pi A}$ (Equation 2-3). The average cell area and the cell perimeter were quantitatively measured using ImageJ software. Shape factor values of unity are representative of rounded cells, whereas values larger than unity indicate the increased morphological asymmetry.

2.2.5 Statistical Analysis

Statistical analysis was performed using ANOVA test. The differences were considered significant for $p<0.05$. Error bars indicate the standard deviation around the mean.

2.3 Results

2.3.1 Qualitative Microstructure Analysis of Polymeric Scaffolds

Using both conventional confocal imaging and multiphoton imaging techniques, it is possible to resolve polymeric scaffolds to a depth of a few hundred microns without the destruction of the sample. **Figure 2.3** illustrates the macro pore structure of the scaffolds at low magnifications and the micro pore structure at higher magnifications. A comparison of CLSM and MPM images is shown here. The maximum intensity projection images and orthogonal view of

the image stacks indicates that images acquired using multiphoton excitation were brighter and had a higher signal-to-noise (SNR) ratio than those taken via single photon excitation. The experimental maximum SNR in **figure 2.4** demonstrates a decline of SNR in both CLSM and MPM images as objective magnification increases: the SNR in CLSM images declined from 18.8 db to 6.3 db, while the SNR of the MPM images declined from 23.4db to 18.5db. The SNR in MPM images at higher magnifications (63x objective) is three times higher than that taken with the same objective via CLSM. Additionally, the SNR observed at higher magnifications via MPM was greater than then SNR observed via CLSM at lower magnifications (10x objective).

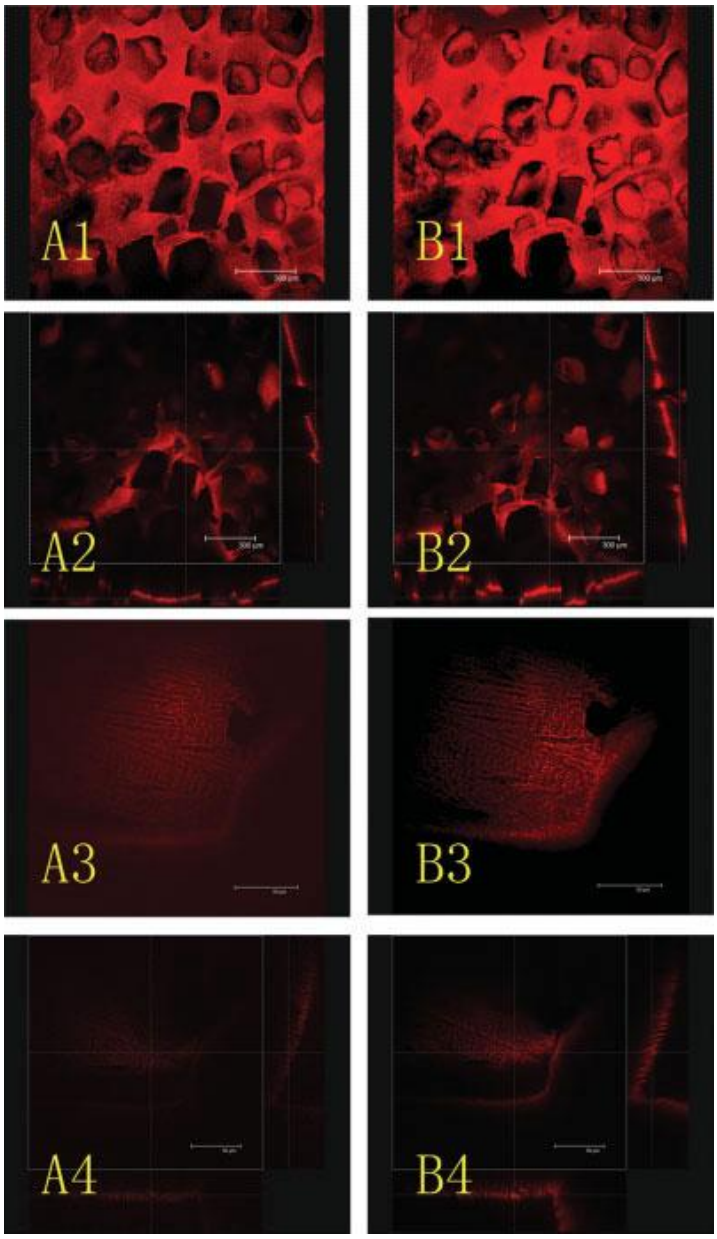

Figure 2.3: Comparative evaluation of the microstructure of porous scaffolds of poly (DTE carbonate) using confocal single photon microscopy (CLSM) and multiphoton microscopy (MPM).

Images marked with “a*” represent MPM images, images marked with “b*” represent CLSM images. **a1-b1**: maximum intensity projection of 10x image stacks, z depth=250um; **a2-b2**: orthogonal view of 10x image stacks, z

depth=250um; **a3-b3**: maximum intensity projection of 63x image stacks, z depth=61.34um; **a4-b4**: orthogonal view of 63x image stacks, z depth=61.34um;

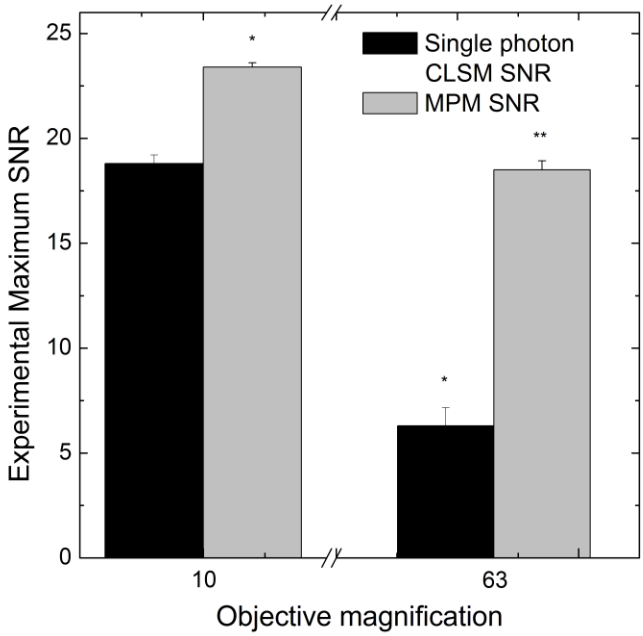

Figure 2.4: **Comparison of experimental maximum signal-to-noise ratio of CLSM and MPM images at different objective magnifications (10x and 63x respectively).**

Images of Texas Red dyed p (DTE carbonates) scaffolds with macro and micro pores were obtained. Scaffolds were excited at 594nm (single photon CLSM) and 880nm (MPM), and emission signals were collected at 605-700nm (CLSM channel) and 610±37.5nm (MPM channel). MPM images shows pronounced improved signal-to-noise ratio over CLSM images, especially at high magnifications. Values are the average of 3 experiments performed in triplicates. Error bars represent standard error around the mean. * A statistically significant difference, $P<0.05$, compared with 10x single photon CLSM images. ** A

statistically significant difference, $P<0.05$, compared with 63x single photon CLSM images.

2.3.2 Quantitative Analysis of Polymer Scaffold Microstructure

The microstructure of porous, biodegradable, polymer scaffolds made from a series of five blend compositions of poly(DTE carbonate) and poly(DTO carbonate) were imaged using two-photon excitation microscopy at vertical depth of 200-250um and 60-75um respectively, and independently examined via scanning electron microscopy (for qualitative validation). Both SEM images and MPM images showed a relatively homogeneous distribution of pores. **Table 2.1** classifies the scaffolds and their respective blend compositions (items A through E). Images of the scaffold structures (macro pores and micro pores) of the polymer family members obtained via MPM and SEM are illustrated in **Figure 2.5**. The macro and micro pore sizes on the raw SEM images were manually analyzed as a comparison to digital image analysis process (thresholding, filters, and morphological operators) to validate the effectiveness and repeatability of the digital image analysis on the MPM images. Ten interceptive lines were drawn on each pore in SEM images, the distance between the points, where the lines intercepted the pixels of the scaffold, were measured and averaged. Comparing the analysis results on MPM images with that on SEM images (**Table 2.2**), it was found that only one of the ten metrics analyzed was significantly different from its respective control (the analysis on raw SEM images).

Table 2.1: Pore quantification results of the scaffold of poly (DTE carbonate)/poly (DTO carbonate) blends.

Pore size/strut size/porosity/interconnectivity were analyzed on three MPM image slices/stacks of three scaffold samples of the same chemistry each. * A statistically significant difference, $P<0.05$, between the values for a given condition and respective control (poly (DTE carbonate) scaffold).

	Scaffold	**A**	**B**	**C**	**D**	**E**
	DTE(%)	**100**	**70**	**50**	**30**	**0**
	DTO(%)	**0**	**30**	**50**	**70**	**100**
MACRO PORES	**Pore size (μm) ± Std**	156±56	159±30	161±38	158 ±42	158±62
	Porosity± Std	0.547 ±0.032	0.556 ± 0.010	0.542 ±0.069	0.497 ±0.058	0.436 ±0.031
	Strut width (μm)	54±15	63±24	55±20	54±19	65±19
	Pore Interconnectivity	0.96± 0.05	0.94± 0.08	0.99± 0.01	0.97± 0.01	0.97± 0.02
MICRO PORES	**Pore size (μm) ± Std**	2.5±0.5	3.0±0.7*	2.9 ±0.7*	4.9±1.9*	3.7 ±1.5*
	Porosity± Std	0.467 ±0.080	0.410* ±0.028	0.373* ±0.039	0.320* ± 0.034	0.276* ±0.080
	Strut width (μm)	1.4±0.3	1.7±0.5	1.5±0.3	1.5±0.4	1.4±0.4
	Pore Interconnectivity	0.98± 0.01	0.98± 0.02	0.98± 0.02	0.99± 0.01	0.98± 0.02

Table 2.2: Comparison of pore size estimation using MPM and SEM.

Each value in the table was analyzed in triplicate on image slices/stacks of three scaffold samples of the same chemistry. * A statistically significant difference, $P<0.05$, between the values for a given condition and respective control (analysis results on SEM images).

	Scaffold	**A**	**B**	**C**	**D**	**E**
	DTE(%)	**100**	**70**	**50**	**30**	**0**
	DTO(%)	**0**	**30**	**50**	**70**	**100**
MPM	**Macro Pore size(um)± Std**	156±56	159±30	161±38	158 ±42	158±62
	Micro Pore size(um)± Std	2.5±0.5	3.0±0.7	2.9 ±0.7	4.9±1.9	3.7 ±1.5*
SEM	**Macro Pore size(um)± Std**	172±16	161±60	187±42	182±45	173±29
	Micro Pore size(um)± Std	2.6±0.75	2.65±0.7	2.7±0.6	4.4±0.9	2.9±0.6

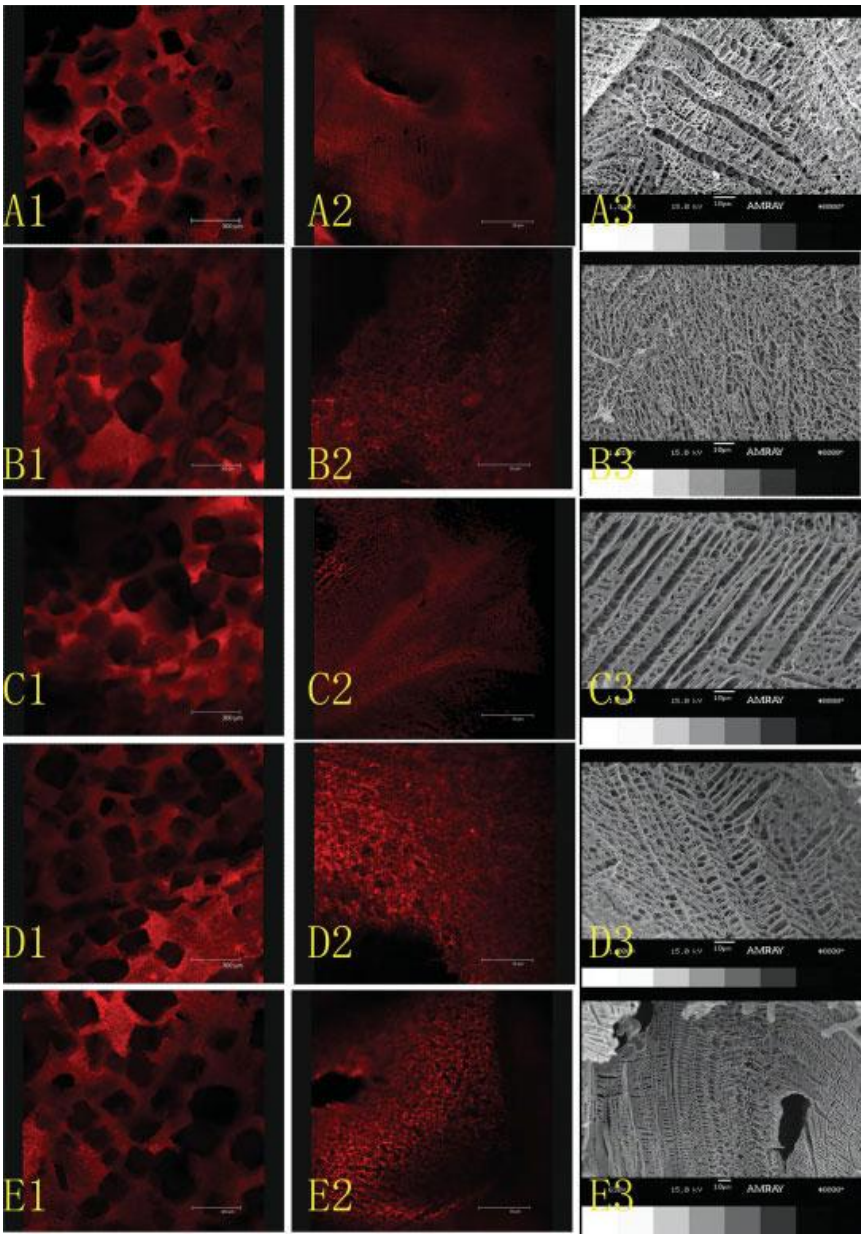

Figure 2.5: Microstructure of the porous scaffolds of varying compositions of poly (DTE carbonate)/poly (DTO carbonate) blends as imaged via MPM and Scanning Electron Microscopy (SEM).

Scaffold A-E refer to: poly(DTE carbonate), 70%poly(DTE carbonate)/30%poly(DTO carbonate), 50%poly(DTE carbonate)/50%poly(DTO carbonate), 30%poly(DTE carbonate)/70%poly(DTO carbonate), and poly(DTO

carbonate). Images marked “*1” represent MPM images of macro pores, images marked with “*2” represent MPM images of micro pores, images marked with “*3” are SEM images of micro pores.

The porosity, pore size, strut size and pore interconnectivity of porous scaffolds were quantified from the MPM image stacks shown in **Figure 2.5**. The macroscale pores exhibited a square/rectangular shape while the micro pores were irregular, lacking a defined morphology. Average macro pore size in the polymer scaffolds was around 158 um with minor variations as the poly(DTE carbonate)/poly(DTO carbonate) ratio was decreased (**Table 2.1**). We found that the average micro pore size increased from 2.5 um to 5um as the poly(DTE carbonate)/poly(DTO carbonate) ratio decreased from 100/0 to 30/70 (**Table 2.1**). Further analysis of the macro pore size distribution showed a normal distribution, with most pores at or near 160 μm size for all scaffolds regardless of their chemical composition (**Figure 2.6a**). Similarly, a normal distribution was obtained for the microscale pores (**Figure 2.6b**), although the average diameter of the micro pores varied at different poly (DTE carbonate)/poly (DTO carbonate) ratios.

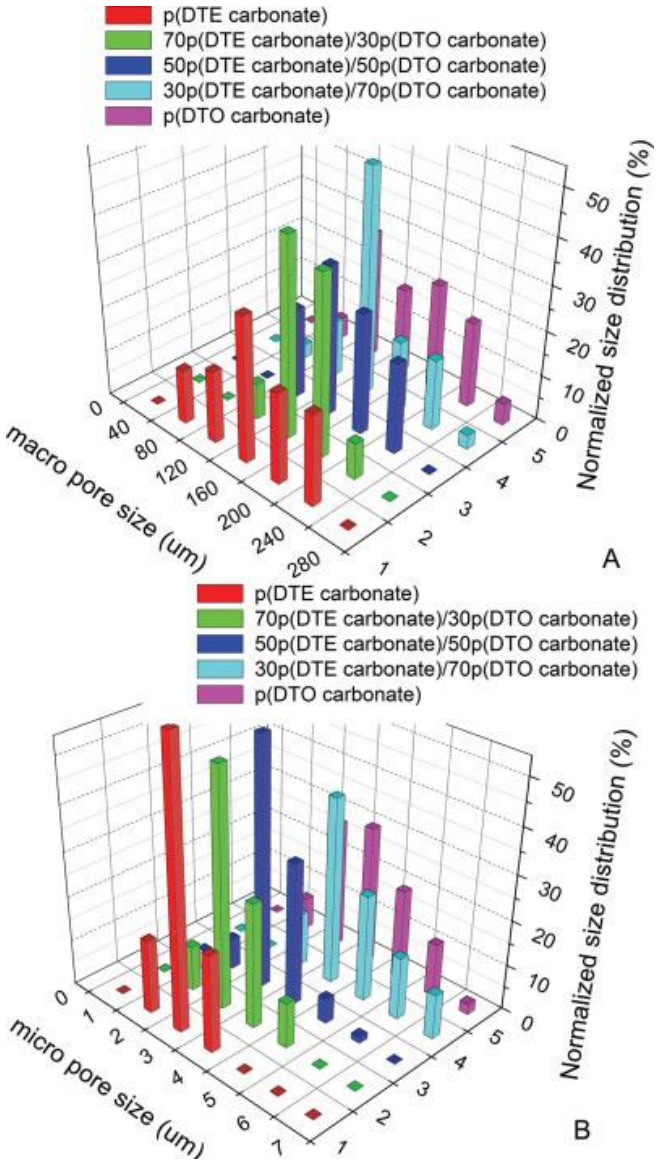

Figure 2.6: MPM enabled bi-modal size distribution of microscale and macroscale pores in scaffolds of poly (DTE carbonate)/poly (DTO carbonate) blends.

a: Size distribution of macroscale pores of poly(DTE carbonate),70%poly(DTE carbonate)/30%poly(DTO carbonate), 50%poly(DTE carbonate)/50%poly(DTO

carbonate), 30%poly(DTE carbonate)/70%poly(DTO carbonate), and poly(DTO carbonate). **b**: Size distribution of microscale pores of poly(DTE carbonate),70%poly(DTE carbonate)/30%poly(DTO carbonate), 50%poly(DTE carbonate)/50%poly(DTO carbonate), 30%poly(DTE carbonate)/70%poly(DTO carbonate), and poly(DTO carbonate).

Porosity analysis revealed that the porosity of macroscale pores was almost invariant with regard to variations of poly(DTE carbonate)/poly(DTO carbonate) ratio (**Table 2.1**), in contrast to the porosity of micro pores, which continuously declined as the poly(DTE carbonate)/poly(DTO carbonate) ratio decreased. Notably, the macroscale porosity for all blend compositions was somewhat higher than the micro porosity (**Table 2.1**). Seen also from **Table 2.1**, the strut size of both macro and micro pores of each test scaffold was relatively constant with regard to polymer chemistry and blend composition, averaging 58 um and 1.5 um for macro and micro pores respectively.

Spatially interconnected pores are highly desirable in tissue engineering. Analysis of interconnectivity demonstrated high levels of pore interconnectivity of both macroscale pores and microscale pores, ranging from 96.3 percent to nearly 100 percent, respectively (**Table 2.1**). Pore orientation was also studied on the MPM images and characterized as the normalized angle distribution. The angle subtended by the major axis of the pores with the horizontal (or vertical) axis was recorded for each pore and the average angle value for each scaffold was taken and shifted to zero degrees to make a more objective descriptor of

pore orientation since angle value could change depending on the orientation of the scaffold itself. Then the normalized and shifted angle distributions of macroscale and microscale pores were plotted, respectively. The distribution probability of macroscale pore angle ranges varied slightly around 17% for all studied scaffolds, indicating that the angles were evenly distributed and these macroscale pores are randomly oriented (**Figure 2.7a**). However, opposite trends were observed following the analysis of normalized microscale pore angle distributions (**Figure 2. 7b**). Among the normalized angle regions (from -90 to 90 degrees), there were peaks at zero degrees which denoted a preference of micro pore orientation for all scaffolds.

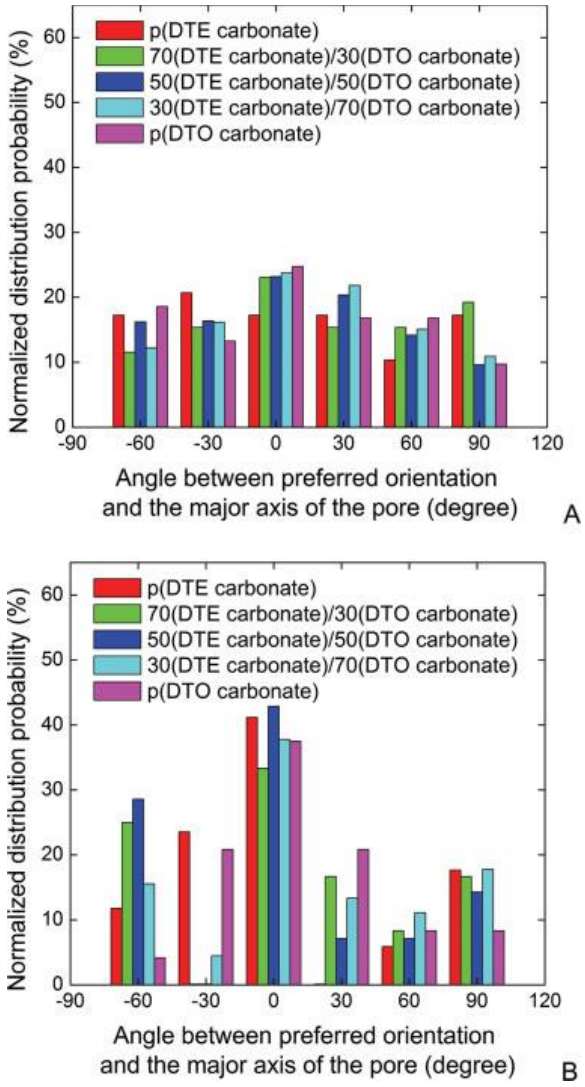

Figure 2.7: MPM enabled normalized orientation distributions of macroscale and microscale pores of scaffolds of poly (DTE carbonate)/poly (DTO carbonate) blends.

The normalized angle distribution probability was plotted as a function of the angle ranges (in bins of 30 degrees). **a**: normalized angle distribution of macroscale pores of poly(DTE carbonate), 70%poly(DTE carbonate)/30%poly(DTO carbonate), 50%poly(DTE carbonate)/50%poly(DTO carbonate), 30%poly(DTE carbonate)/70%poly(DTO carbonate), and poly(DTO

carbonate). **b**: normalized angle distribution of microscale pores of poly(DTE carbonate), 70%poly(DTE carbonate)/30%poly(DTO carbonate), 50%poly(DTE carbonate)/50%poly(DTO carbonate), 30%poly(DTE carbonate)/70%poly(DTO carbonate), and poly(DTO carbonate).

2.3.3 MPM Imaging of Cellular Morphology within Polymer Scaffolds

Utilizing conventional CLSM and MPM, GFP engineered rat fibroblasts were imaged after seeding within the poly (DTE carbonate)/poly (DTO carbonate) blend porous polymer scaffolds. Images demonstrated improved clarity of cell visualization with MPM versus CLSM (**Figure 2. 8**). Images produced with MPM had improved signal to noise ratios, a significant reduction in the photobleaching of the Texas Red dyed scaffolds, and a marked improvement in the ability to visualize cellular interactions on the scale of scaffold features.

Further, we quantified cellular morphogenesis in the scaffolds using MPM in terms of cellular area, perimeter, and morphologic shape factor. The MPM analysis confirmed the visual observations that cells cultured on 50% poly(DTE carbonate)/ 50% poly(DTO carbonate) blends scaffold exhibited greater spreading than either poly(DTE carbonate) homopolymer scaffold or poly(DTO carbonate) homopolymer scaffold (**Table 2.3; Figure 2. 9**). Notably, no significant differences were observed between overall projected areas of cells cultured in poly (DTE carbonate) scaffold and poly (DTO carbonate) scaffold.

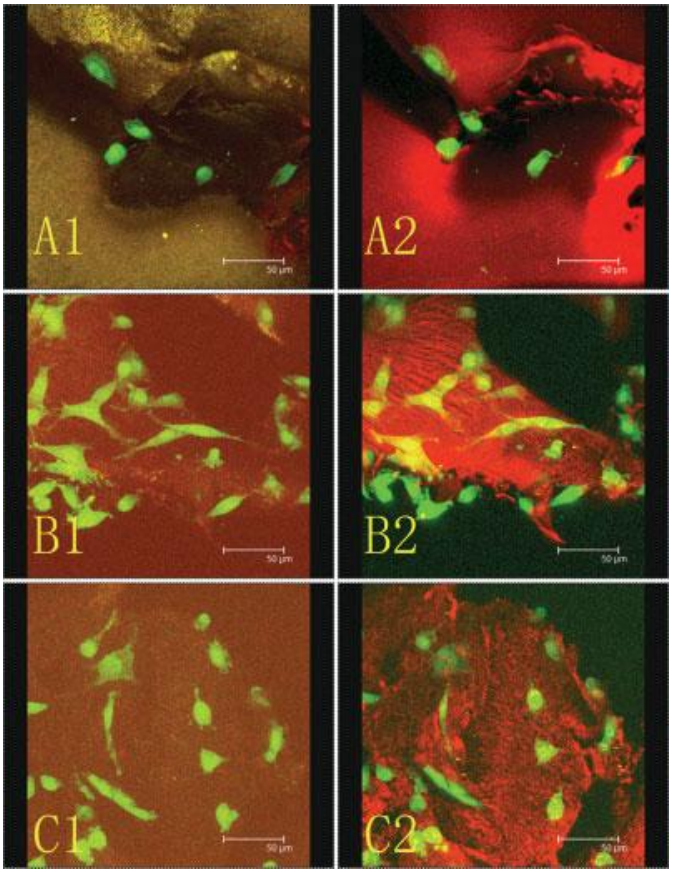

Figure 2.8: Comparison of MPM and CLSM images of GFP-fibroblast Cells in Texas Red dyed poly(DTE carbonate)/poly(DTO carbonate) blends scaffolds.

Cells were seeded on the scaffolds for 8 hours before imaging. All images were taken on Leica SP2 microscope, using 63x glycerol immersion objective (NA=1.2). **a1-a2**: CLSM and MPM images of GFP-fibroblast cells on poly(DTE carbonate) scaffold; **b1-b2**: CLSM and MPM images of GFP-fibroblast cells on 50%poly(DTE carbonate)/50%poly(DTO carbonate) blend scaffold; **c1-c2**: CLSM and MPM images of GFP-fibroblast cells on poly(DTO carbonate) scaffold. In CLSM mode, emission at 500-535nm and 605-700nm were used to collect

fluorescence signals from GFP-Fibroblast and Texas Red respectively. In MPM mode, two channels at 525±25nm and 610±37.5nm were used to collect fluorescence emissions from GFP-Fibroblast and Texas Red respectively. All image sizes were 512 by 512 pixels.

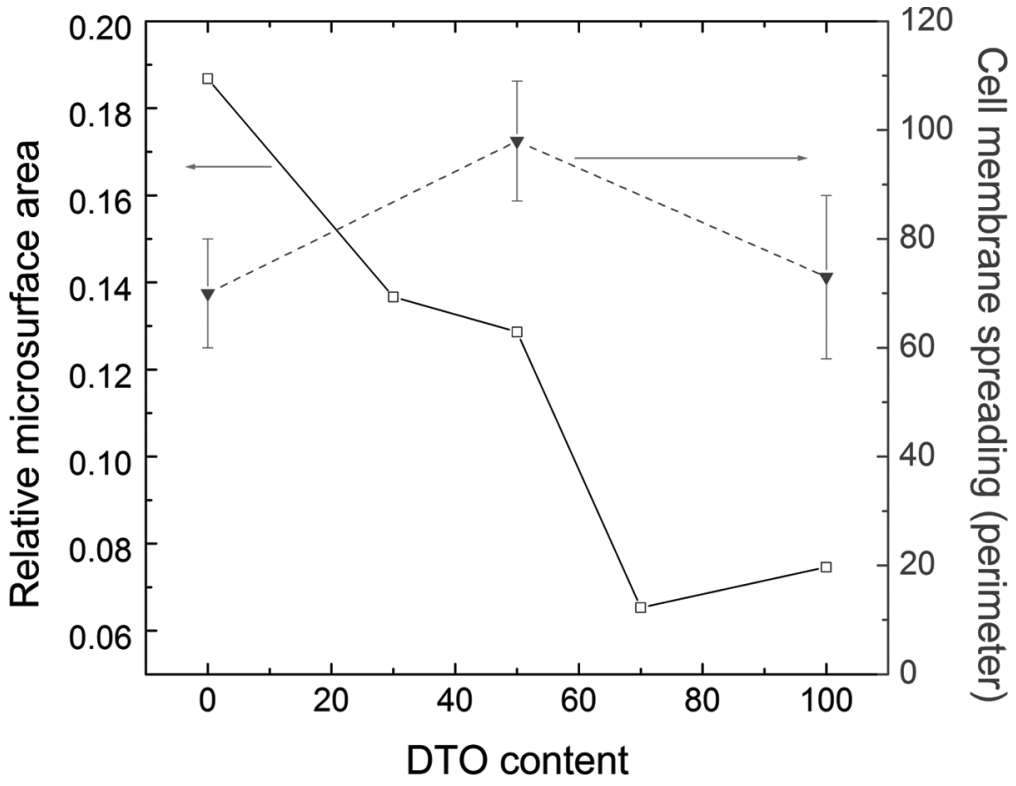

Figure 2.9: Composite biorelevant profiling of scaffolds using multiphoton microscopy: Correlation of cell morphogenesis and polymer scaffold microstructure for blends of variable DTO content.

The scaffold microstructure was quantified in terms of the relative substrate microsurface area (computed as number of micropores times average area of micropore), while the cell membrane spreading was quantified in terms of cell perimeter (**Table 2.3**).

The incorporation of the more hydrophobic DTO is reported to suppress cell spreading on two-dimensional films[72], but our MPM studies show an increase in cell spreading on 3-D scaffolds upon the incorporation of 50% DTO, which can be attributed to the variations in scaffold microstructure. Intermediate levels of scaffold microporous surface area enhanced cell spreading, indicating that the role of substrate microstructure, and not the surface chemical effects, was likely the predominant determinant of cell spreading in this regimen.

Table 2.3: Quantification of Cell Spreading in Polymer Scaffolds using Multiphoton Microscopy.

10 to 30 cells were analyzed per scaffold. * A statistically significant difference, $P<0.05$, between the values for a given condition and respective control (poly (DTE carbonate) scaffold).

Scaffold chemistry	**Cell Area, A (μm^2)**	**Cell Perimeter, P (μm)**	**Cell Shape factor, $\emptyset$**
P(DTE carbonate)	240±35	70±10	1.7±0.4
50%p(DTE carbonate) 50%p(DTO carbonate)	306±60*	98±11*	2.5±0.3*
P(DTO carbonate)	221±59	73±15	2.0±0.5

2.4 Discussion

Advances in scaffold fabrication technologies have brought a new dimension to the field of tissue engineering[171,227,228]. Assessment of the performance of material-based engineered tissues will require quantitative measures of scaffold properties, structures, composition and in vitro cellular responses. Previously reported methods for characterizing and quantifying scaffold microstructure and cell-scaffold interactions have been limited by harsh processing of specimens (SEM) and the inability to provide high quality images at a penetration depth of a few hundred microns. In this study, a novel approach based on multiphoton microscopy was employed to quantify the microstructure of porous biodegradable polymer scaffolds as well as cell-scaffold interactions in a non-invasive manner. Multiphoton microscopy, through a two-photon fluorescence excitation rather than single photon fluorescence excitation, restricts fluorophore excitation/emission to the focal plane of the microscope, which provides high quality thin optical section images from deep within thick specimens. 2-D multiphoton image slice series were subjected to digital image analysis and 3-D reconstruction processes to obtain the overall 3-D structural characteristics of the polymer scaffold at macro and micro scale as well as the cellular responses. The porosity, pore size and distribution, strut size, pore interconnectivity and orientation of both macro and micro pores of poly (DTE carbonate) / poly (DTO carbonate) blends were quantified. Statistical analysis demonstrated that the resulting metrics of the digitally analyzed MPM images were no different (analysis not shown) from the metrics calculated based on SEM

images that did not undergo digital image analysis processes (thresholding, filters, and morphological operators). This validated the use of digital image analysis on MPM acquired images for the determination of scaffold architecture. Compared with other scaffold characterizing techniques, MPM microscopy with subsequent digital image analysis provides non-invasive, high quality, improved signal to noise (SNR), 3-D image sections with a resolution of less than one micron.

Studies have shown that a major advantage of MPM over CLSM is a significant improvement in the imaging penetration depth by a factor of two or more without a loss of lateral resolution in typical biological specimens that are highly light scattering[222-224,229,230]. The effective resolution achieved from MPM and single-photon CLSM is a function of many complex factors, such as the absolute number of photons (signal intensity) collected per pixel and the fraction of true signal photons relative to scattered photons from outside the observation volume (contrast or SNR)[219,231]. Therefore, the SNR (contrast) of the images plays a key role in the evaluation of image quality. Our MPM scaffold images at low magnifications (10x objective NA=0.3) showed a 25% improvement in SNR over the corresponding single photon confocal images at a z-depth of 250 um. The MPM scaffold images obtained at higher magnifications (63x objective NA=1.3) showed a more pronounced improvement in SNR over one photon CLSM scaffold images (300%). Several factors possibly account for this SNR improvement[223,232-234]. The degradation of confocal images is especially evident at higher magnification where far fewer photons can be collected through the

lens in a much smaller region of sample. Additionally, the struts bounding the micro pores (size range 2~55um) scatter more light than struts among macro pores (size range >100um) due to Mie Scattering, which is more prevalent for 2~5 um micro pores rather than 150 um macro pores. Therefore, at higher magnifications, both Rayleigh (particles sized 1/10 of wavelength) and Mie scattering (particles sized at larger diameters) contribute to the background noise while at lower magnifications, Mie scattering is negligible. Therefore, with the decrease in collected fluorophore emission intensity and increased contribution of scattered photons to the background, the SNR of the high magnification single-photon CLSM images is expected to deteriorate. On the other hand, as the MPM does not generate a signal out of the plane of focus, there are no spurious scattered photons to contribute to the background and image contrast is maintained. Our higher magnification (63x) images of MPM and single photon CLSM illustrate this trend: both single-photon CLSM and MPM images encounter a decrease in the SNR value when switching from low magnification objective (10x) to high magnification objective (63x), however, the single-photon CLSM images attenuate much faster than MPM microscopy.

The use of MPM incorporated with the digital image analysis process afforded insights into the role of polymer chemistry and fabrication with regards to variations of local micro-architecture of the porous scaffolds fabricated from poly(DTE carbonate)/poly(DTE carbonate) blends. Clearly, the macroscale pore formation is largely dictated by the salt-leaching process, and therefore, strut size, pore size, and porosity of the macro pores are not likely to be sensitive to

alterations of DTO/DTE ratio. A statistical analysis of the macropore size distribution using the MATLAB code 'normplot' revealed that the pores have identical mean diameters and follow a Gaussian distribution regardless of the scaffold chemistry (data not shown). The microscale pores are generated by liquid-liquid phase separation enabling nucleation and growth of the pores via rapid cooling within the spinodal phase regime. It is reported that with increasing composition DTO, the average diameter of the micropores increased, while the total number of observed pores decreased. These observations are most likely due to the kinetics of nucleation associated with pore formation and the relative glass transition temperatures of the polymer blends. poly (DTE carbonate) has a glass transition temperature of 81^{o}C while poly (DTO carbonate) has a glass transition temperature of 58^{o}C. During the cooling process, those blends rich in DTE versus DTO become vitrified earlier decreasing time for Ostwald ripening, the process by which smaller droplets dissolve and larger droplets expand, and coalescence of the solvent rich phases[235-239]. This results in an increased number of total micropores with decreased individual sizes of the pores when compared to the DTO rich blends, which have increased opportunity to undergo the aforementioned phenomena prior to vitrification.

Pore interconnectivity was calculated from the 3-D reconstructed images of the scaffolds. It is important to note that for the image based interconnectivity calculations to be valid, the thickness of the reconstructed images in the vertical direction must be significantly larger than the individual pore sizes. The current study contained reconstructed 3-D image stacks of macro and micro pores that

were 250 um and 60-75 um thick respectively. Since the macro and micro pores were respectively on the order of a hundred microns and microns scale, the 60 um z stacks of micro pore images should be sufficient for interconnectivity analysis while the 250 um z stacks of macro pore images might not represent the true macro pore interconnectivity. The penetration depth improvement on the MPM imaging modalities may be helpful for better evaluation of macro pore interconnectivity.

Further analysis of the scaffold architecture reveals that the pore strut size is neither affected by the scaffold chemistry nor by the fabrication method. The pore strut size remains constant at 58 um for macropores and 1.5 um for micro pores. Similarly, both macro and micro pore interconnectivity values were high (>90%) and are unaffected by scaffold chemistry and fabrication methods. Previous studies reported that the porosities and interconnectivity of the scaffolds were determined by the interstitial space in the leachable templates and by the initial concentration of the polymer solution used in freeze drying[240]. The porogen/polymer weight ratio determines the pore microstructure of the scaffolds with highly interconnected pores observed when the porogen/polymer ratio range lies between 15-20[241], At sufficient porogen/polymer ratios such as the ones we employed, the salt particles are clustered and therefore the pores obtained after leaching are open and well interconnected[242].

Orientation analysis of the scaffold microstructure showed that scaffold fabrication process has some hierarchical relationship with pore orientations. There was no orientation preference for the macroscale pores while microscale

pores indicated an orientation bias. The possible explanation is that the salt leaching process occurs under normal conditions (room temperature, standard pressure) with the tension/compression around the porogen evenly distributed. In the case of microscale pore orientation, during the phase separation and freeze drying process that occur in liquid nitrogen, small amounts of existing water molecules cause nucleation and promote solvent crystallization, which result in the phase separation within the polymer blends and thus induce the orientation of micro pores.

This study validates the utilization of MPM for the real time in situ imaging of fluorescent cells seeded within 3-D porous polymer scaffolds. Cells were visualized with greater effectiveness using MPM over CLSM due to the greater SNR and reduced scatter with MPM as has been previously explained. Perhaps the greatest advantage of MPM was the ability to simultaneously image fluorescently engineered cells and scaffold microstructure. As was demonstrated (**Figure 2.8**), in comparison to CLSM, MPM allowed better combined resolution of cell morphology and scaffold microstructure (micropores). This is essential in facilitating the detailed examination of how scaffold structures may mediate cellular responses and behaviors[243]. Specifically, in our study, we found enhanced cell spreading on scaffolds of polymer blends rather than scaffolds of corresponding homopolymers. Our findings stand in contrast to those recent studies of similar substrates in 2-D film configurations[100], wherein cell spreading was inhibited on substrates with increased poly(DTO carbonate) content in the poly(DTE carbonate)/poly(DTO carbonate) blends, likely due to increased

hydrophobicity of the polymer. Our results suggest that the scaffold microstructure also plays a key role in modulating cell spreading aside from the effects of polymer chemistry[48,244-246]. Micropores can present microscale texture, which, depending on the cell adhesivity of the substrate, can affect the interdigitation of the cellular membrane with the scaffold and thus alter cell membrane spreading[247]. We estimate from the number of micropores and the size of micropores of the various scaffolds that the net microporous surface area is the highest for poly(DTE carbonate) scaffolds and decreases progressively upon the incorporation of DTO (**Figure 2.9**). Thus, the 50%poly(DTE carbonate)/50%poly(DTO carbonate) blend substrates, which exhibited larger micropores than poly(DTE carbonate), elicited the most enhancement in cell spreading. Since incorporation of 50% poly(DTO carbonate) should have reduced cell spreading, not increased it, we believe that the scaffold microstructure likely plays a major role in influencing cell spreading within this regimen. The 100% poly(DTO carbonate) scaffolds, which had the largest micropores but the least fraction of microporous surface area, did not elicit enhanced cell spreading, suggesting that a combination of scaffold microstructure and surface chemistry influence cell spreading.

2.5 Conclusion

In summary, while MPM has been previously validated to be an effective noninvasive method for imaging various cells and tissues, we present the first systematic report of the comparative use of MPM for the characterization of

biodegradable polymer scaffold microstructures. We have demonstrated that MPM imaging techniques are superior to confocal imaging and can achieve high signal to noise ratio for the dual characterization of non-invasive visualization and quantification of both biodegradable polymer scaffold microstructure as well as the local cell morphogenesis within scaffold. This MPM imaging/image analysis based platform enables quantitative characterization of 3-D biomaterial scaffold spatial features as well as pseudo-3D cell spreading features.

3 High Content / Rapid Screening of Cells on 2-D Substrate and Gradients

Note: This chapter is reproduced from the following publication:

Liu, E., M.D. Treiser, H. Patel, H.J. Sung, K.E. Roskov, J. Kohn, M.L. Becker, and P.V. Moghe. 2009. “High-content profiling of cell responsiveness to graded substrates based on combinatorially variant polymers”. Combinatorial Chemistry and High-throughput Screening - Special Issue on Combinatorial and High-Throughput Screening of Cell Response to Biomaterials 12(6).

3.1 Introduction

Polymer substrates differing in chemical properties, post-processing physical properties, and geometries have been shown to cause variable changes in cellular processes by way of alterations in protein adsorption, cell adhesion and spreading, and extracellular matrix production[87,88]. Parameters such as hydrophobicity, physicomechanics, architecture, and differential ligand conditioning represent strong determinants of both cell function and phenotypic expression[89-91,122]. Most of the studies to date depend on traditional characterization assays and a limited number of material conditions. This limitation on potential physical parameter space represents a significant shortcoming as interesting behaviors elicited in response to incremental but unselected experimental conditions may be overlooked.

Current trends in polymeric biomaterials discovery have expanded from the synthesis of a few potential materials to the design of relatively large libraries

of combinatorially derived materials[92,94,248]. These libraries permit the exploration of a large physico-chemical "property" space while simultaneously promoting the development of detailed relationships which relate cellular actions to material parameters[96-98]. Advances in instrumentation for the synthesis and assembly of large polymer libraries have expanded the size and complexity of available material arrays[99]. The advantage of such sizeable material test sets lies in the more thorough examination of cell-material behaviors that would have otherwise gone unnoticed when investigating smaller libraries. However, the full impact of combinatorial polymer libraries will be realized only with the development of methods that are able to evaluate material performance on the scale of the synthesis[248]. Unfortunately, traditional approaches to characterization and the biological screening of materials are not amenable to the rapid evaluation of large member material sets and therefore, necessitate the development of novel screening approaches.

One technique that has garnered significant interest involves the creation of single substrates with spatially resolved chemistries, roughness, and/or microstructures[100-103,249]. Single substrate approaches allow for the assay of cellular response to materials of differing properties with equivalent processing conditions and faster data acquisition, thereby providing lower experimental error[105,250]. Additionally, studies which vary both chemistry and temperature and utilize gradient-based technology permit the simultaneous study of continuous ranges of chemical and topographical properties[98,100,102,251]. These methods represent great potential as they map the near complete compositional and

processing experimental space of binary blends. This matrix of chemistries and surface physical properties further facilitates the identification of potentially new structure-function relationships that may help biomaterial scientists to rationally design materials to meet specific applications.

To establish cell-material relationships, it is necessary to isolate individual material parameters and their effects on specific responses. Zapata et al. employed continuous temperature gradients to assess osteoblast response to demixed polymer blends[102]. Previously, Bailey et al. utilized discrete binary blends of two tyrosine-derived polycarbonates, poly(DTE carbonate) and poly(DTO carbonate) (abbreviated as pDTEc and pDTOc, respectively, throughout this manuscript) and used phase separation-induced topography to determine how changes in material surface energetics and roughness affect cells grown on these surfaces[100]. These studies demonstrated that surface microstructure and topography strongly influenced cell attachment, spreading, and proliferation. One limitation highlighted by the authors in this study was that because the topographical features of the surface were dependent on both composition and temperature, universal structure-function correlations regarding roughness, surface chemistry, and cell responses could not be readily ascertained.

Recently, Treiser et al. published a technique whereby high-content imaging of cell morphology yielded a large number of quantifiable descriptors that can be used to potentially discern combinatorial variations in substrate composition[47]. Using a similar high content imaging approach, this study derives

morphometric descriptors from cells cultured on discrete binary blends of pDTEc and pDTOc that have been annealed on a gradient heat stage, which yields a temperature-induced roughness profile. Cell descriptors that are sensitive to roughness and/or surface chemistry are identified, and were utilized to decouple the effects of roughness and surface chemistry on cell attachment and adhesion strength. This study demonstrates a fast-screening, high-content imaging method to discern how surface topography and surface energy of structurally similar but compositionally varying, immiscible blends affect biological response on two dimensional gradient substrates.

3.2 Materials and Methods

3.2.1 Polymer Synthesis and Gradient Fabrication

Tyrosine-derived polycarbonates were synthesized as described previously.[252] Poly(desaminotyrosyl-tyrosine alkyl ester carbonate)s are referred to as poly(DTR carbonate)s, where R represents the alkyl ester pendent chain. In this study R is either ethyl (DTE) or octyl (DTO). The mass-average molecular mass and molecular mass distribution Mw/Mn (PDI) for each of the polymers are listed. poly(DTE carbonate) (abbreviated as pDTEc): Mw = 131,000, PDI = 3.0; poly(DTO carbonate) (abbreviated as pDTOc): Mw = 61,500, PDI = 2.7.

3.2.2 Annealing Gradient Preparation

Discrete composition thin film strips of pDTEc and pDTOc tyrosine-derived polycarbonate homopolymers and blends (70/30,50/50,30/70 pDTEc/pDTOc

ratio, by mass) were fabricated on a single 42 mm round glass coverslip (VWR, No 1½) by flow coating (F**igure 3.1**)[253]. Briefly, 3 % (mass fraction) solutions of each mixture were dissolved in methylene chloride and 25 uL drops were placed under the blade. The coating conditions were stage acceleration of 25 mm/s^2, stage velocity of 15 mm/s and a spread distance of 40 mm resulting in films approximately 0.2 mm thick. The substrates were then subjected to a variable temperature heating stage exhibiting a well-defined linear temperature range to induce phase-separation[100]. The range and slope of the temperature gradient are tailored through the respective block temperatures and their distance apart. All gradients and control films were annealed for 48 h in air. The final substrates consisted of five discrete polymer strips (two homopolymer and three blends) on a single coverslip which when subjected to a linear annealing temperature profile orthogonal to the respective compositions. This format yielded "two-dimensional gradients substrates" (referring to these substrates with a continuous temperature gradient in one dimension and a discrete compositional gradient in the other). The films were sterilized using ethylene oxide and degassed for 48 h prior to use.

3.2.3 Atomic Force Microscopy (AFM)

Tapping-mode atomic force microscopy measurements were conducted in air with a Nanoscope IV system (Digital Instruments) operated under ambient conditions with standard silicon tips (Nanodevices; L, 125 um; normal spring constant, 40 N/m; resonance frequency, (300 to 360) kHz). Images were collected using automated data acquisition every 2.5 mm. Root mean square

(RMS) roughness measurements were determined using standard Digital Instruments software; averages and standard deviations were determined from two measurements at each distance from each of two different polymer thin film coated coverslips (n=4). Normalized mean gradients of steepness were calculated for 5 positions at 5 mm intervals for each of the compositional strips. Normalized gradient steepness was calculated with the following formula:

$$\text{Normalized gradient steepness} = \frac{\Delta\ \text{RMS Roughness}}{(\text{Physical Distance})(\text{Mean RMS roughness})}$$

(Equation 3-1)

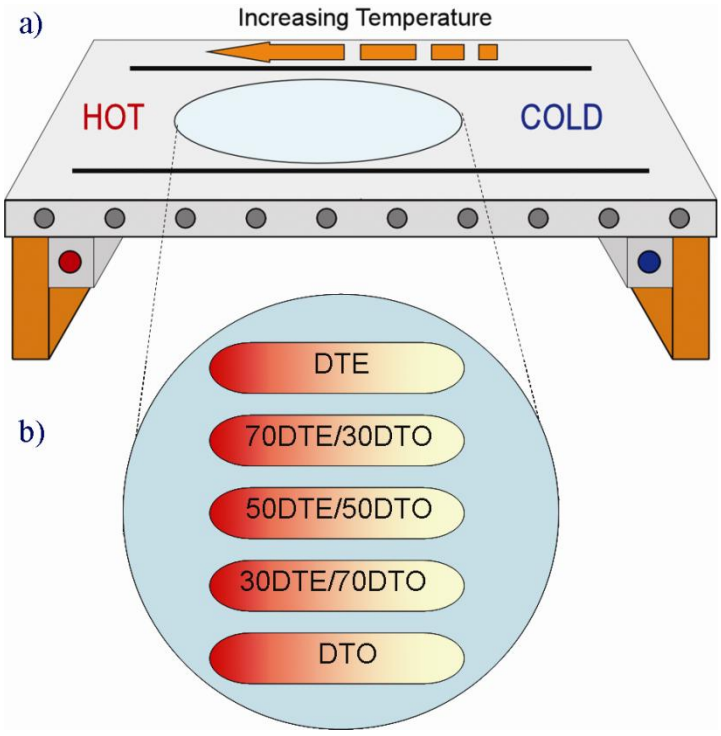

Figure 3.1: Fabrication of 2D orthogonal composition/roughness gradient platform.

a) Schematic of roughness gradient polymer substrate fabrication using the annealing temperature gradient platform. **b)** Overview of the design of the

roughness gradient substrates based on polymer blends. Along the horizontal axis is a continuous temperature annealing gradient; along the vertical axis is the compositional variation of pDTEc/pDTOc blends.

3.2.4 Cell Culture and Transfection

Human Saos-2 cells (a gift from Dr. David Denhardt; Rutgers University) transfected with Green Fluorescent Protein (GFP)-tagged farnesylation (GFP-f) gene were used as model cell lines to probe the morphology and organization of cells cultured on topological gradients of poly(DTE carbonate) and poly(DTO carbonate) blends. The gene that encodes the farnesylation protein is fused with the EGFP gene in the vector (Clontech, Mountain View, CA). SV40 viral promoter is used for the expression of GFP-farnesylation protein in mammalian cells. The farnesylation gene codes for a 20 amino acid sequence, which translates to the farnesylation protein that targets and binds to Ha-Ras, creating the farnesylated Ras protein complex. This binding process is mediated by a farnesyl transferase enzyme, which accompanies targeting of the protein complex to the inner face of the cellular plasma membrane. Because pEGFP is tagged to the farnesylation gene within the same vector, EGFP and farnesylation proteins are co-expressed, and EGFP can therefore be utilized as a visual indicator of activation of the Ras-farnesylation process, as well as an intracellular tracer to track the farnesylated Ras protein complex as it localizes to the plasma membrane. Therefore, using the pEGFP-farnesylation reporter gene provides two simultaneous advantages: 1) a membrane marker, which allows for fluorescent demarcation and resolution of the plasma membrane and is used for

morphometric cellular analysis, and 2) an indicator of cell signaling activation related to oncogenic Ras-mediated cell proliferation, which is presented as GFP-f intensity descriptors, such as standard deviation, mean, maximum, and minimum values of the density (GFP-f fluorescence intensity normalized to cell area). The transfection process was performed as previously described[47]. Briefly, Saos-2 cells were propagated in HAM's F12 (F12H) culture medium (Invitrogen, Carlsbad, CA, USA) supplemented with L-glutamine, penicillin-streptomycin, and 10% fetal bovine serum (FBS; Sigma-Aldrich, St. Louis, MO, USA). Cells were transfected with Lipofectamine™ supplemented with PLUS™ reagent (Invitrogen), and stable lines were selected using 0.5 mg/mL G418 (Sigma-Aldrich). Saos-2 GFP-f cells were cultured in flasks (75 cm^2 surface area) at 37 ^oC in a fully humidified atmosphere with 5 % CO2 in F12H (Invitrogen, Carlsbad, CA) supplemented with L-glutamine, penicillin-streptomycin, and 10 % fetal bovine serum (Sigma; St. Louis, MO). Medium was changed twice weekly and cultures were passaged with 0.25 % Trypsin EDTA (Lonza Inc., Walkersville).

3.2.5 Confocal Microscopy and Imaging

Saos-2 GFP-f cells were cultured on the roughness gradient substrates and incubated for 24 h at 37 °C. Live cell, real-time imaging was performed within a temperature controlled POC chamber retrofitted on the motorized stage of a Leica TCS SP2 confocal laser scanning microscope (CLSM) (Leica Microsystems Inc. Exton, PA). Green fluorescent images of cells were acquired using a 488 nm excitation with a 500 to 535 nm emission bandpass filter. All image frames underwent two line and frame averaging. For higher throughput

cell attachment and adhesion imaging, tile-scanned CLSM images were obtained at low (10X objective, numerical aperture (NA) =0.7) magnification over a 2.5 mm x 30 mm region (n = 6). For high-content imaging, single cells were viewed under high magnification (63x oil immersion objective NA=1.3) for the quantification of morphologically based cell descriptors (Image Pro Plus, Silver Spring, MD) and functional data (e.g. cell attachment and spreading). For the high-content imaging 15-30 cells per position (5 positions per composition) were examined for two independent substrates (n = 2).

3.2.6 Degree of Cell Attachment

Cells were seeded (6000 cells/ cm^2) on polymer gradient substrates and incubated for 24 h (n = 2). The culture medium was removed and the disks were washed carefully with PBS to remove any unattached cells. The roughness gradients underwent tile scanning as described previously. The total number of cells within a region was determined.

3.2.7 Degree of Cell Adhesion Strength

The cell adhesion strength was quantified by determining the centrifugal force required to detach a critical fraction of adherent cells from the respective position on the gradient substrates. Cells were seeded (6000 cells/ cm^2) on the gradient substrates and allowed to adhere for 1 h. Samples were then inverted and plates were filled with 1x DPBS solution (Lonza Inc.). The substrates were subjected to stepwise increases in centrifugal force ((200 to 800) rpm, corresponding to (9 to 146) x g) in a Beckman centrifuge for 5min at room

temperature. The number of adherent cells remaining on each surface was determined microscopically in six random positions on two independent samples (n = 2). The mean detachment force required to remove a critical fraction of adherent cells was calculated from the following relationship: $f = RCF \times V_c(\rho_c - \rho_m)$ (Equation 3-2), where RCF is the centrifugal force applied to the samples, V_c is the volume of a cell, and ρ_c and ρ_m are the densities of a cell and the medium respectively[244].

3.2.8 GFP-farnesylation Based Morphometric Descriptors of Single Cells

Individual cell images of GFP-fusion protein expressing cells acquired through confocal microscopy were exported to Image Pro Plus (Version 5.1 for windows, Media Cybernetics, Inc., MD, USA) for morphometric descriptor generation. Image processing algorithms included contrast enhancement, low pass/sobel/flatten filtering, intensity-based thresholding, morphological operations, and parameter measurements. 15-30 at cells examined from each position were used to calculate a population distribution for each descriptor.

The GFP-f descriptors were analyzed in two ways. The first utilized the ability of GFP-tagged farnesylation protein to fluorescently demarcate the plasma membrane. This analysis was not affected by variations in GFP-f fluorescence intensity, but was valid as long as the plasma membrane demarcation could be identified through image processing algorithms. It was possible to measure the cell boundary through membrane demarcation at even minimal fluorescence signaling around the plasma membrane. This analysis provided us with various

cellular morphologic parameters: area; perimeter; lengths of major and minor axes of the ellipse circumscribing the same geometric area of the cell; mean radius; mean diameter; roundness; protrusions; protrusion length; mean feret length; maximum feret length; and minimum feret length. The second mode of analysis scrutinized the variation in GFP-f fluorescence intensity within a single cell area. This analysis relates to the level of intracellular expression of the farnesylation protein and to Ras-mediated cell signaling activity, as described above. It provided us with another class of descriptor parameters: mean, sum, and standard deviation of density (GFP-f fluorescence intensity normalized to cell area); margination; heterogeneity; and clumpiness.

All descriptors listed were calculated utilizing standard object descriptors provided with Image Pro Plus software. SPSS statistical software (SPSS; Chicago, IL, USA) was then used to determine which high-content descriptors correlated best with surface roughness and cell attachment on the gradient surfaces. Bivariate correlation coefficients were computed relating each of the descriptors with surface roughness and cell attachment. Correlation coefficients that were found to be statistically significant ($p<0.05$ unless otherwise noted) were extracted for further analysis.

3.2.9 Statistical Analysis

Statistical analysis was performed on morphometric parameters using SPSS software and included analysis of variance (ANOVA) with Tukey's HSD post hoc method and other multivariate statistical tools. The differences were

considered significant for $p < 0.05$ unless otherwise noted. Error bars indicate the standard uncertainty around the mean.

3.3 Results and Discussion

3.3.1 Two-Dimensional Gradient Fabrication

Significant efforts have been expended to develop a versatile platform capable of varying one or more material properties with well-defined spatial constraints for biomaterials applications. However, unexpected physical and chemical variations which occur during the material processing remain a persistent challenge[249]. These variations impede a correlation-based interpretation of biological events. The combinatorial platform presented in this study was designed to vary two material properties, i.e., surface topography and chemical composition in a two-dimensional gradient platform (**Figure 3.1b**). This platform affords the simultaneous evaluation of the topography changes that present themselves during the phase separation process within a series of discrete blend compositions. Unlike current microarray-based methods for the concurrent assessment of hundreds of potential biomaterials[254], the orthogonal gradient approach in this study focuses on the detailed examination of the effects of two material properties; surface topography associated with phase separation and composition, on cellular responses within a single substrate.

The phase-separation technique has been utilized to produce a variety of surface features in polymer blends[98,100-102,249,255]. Unlike other technologies, including laser ablation[256,257], helium irradiation[258], and imprint lithography[89], which produce discrete topographical features on polymer surfaces, this

temperature gradient method produces a wider variation in surface properties. The demixing process was induced by annealing the blends of pDTEc/pDTOc on a hot stage possessing a linear temperature gradient. This resulted in a composition-dependent change in the surface roughness and surface-available phase fraction, which were determined by AFM measurements (**Figure 3.2**). The slope of the roughness variation was determined mainly from the pDTEc content in the blend. Phase separation is a kinetically controlled process and as the temperature of the thermal stage approached the glass transition temperature (Tg) of the pDTEc (99.2 $\pm$ 0.7 and 52.6 $\pm$ 1.6 ^{o}C for pDTEc and pDTOc respectively)[100] the demixing process slows appreciably. The phase-separated surface of 50/50 pDTEc/pDTOc blends exhibited RMS roughness values ranging from 68 nm to 5 nm. Similar pseudo-linear curves with varying slopes in the surface roughness were observed on 70/30 and 30/70 pDTEc/pDTOc blends with RMS roughness values ranging from 35 nm-5 nm and 50 nm-5 nm, respectively (**Figure 3.2**). The reproducibility and the pseudo-linear increase in the surface roughness that were demonstrated in this study indicate that the temperature gradient technologies can be utilized as a reliable property-controlled gradient platform. Complicating the trend elucidation is the fact that the respective components of the phase-separated surfaces exhibit markedly different behavior. The variable annealing temperature procedure yields a profile that possesses various amounts of each phase at the surface. As the individual components each have different protein adsorption behavior, the variable profile

has rich physico-chemical phase space[46]. Composition control in the form of discrete blends simplifies further the potential chemical variability.

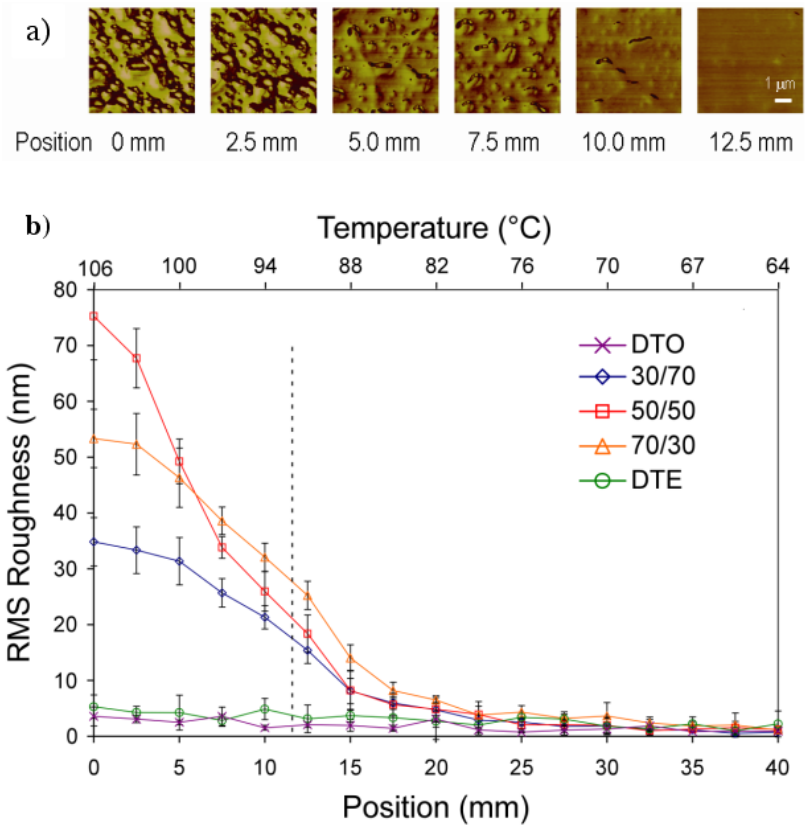

Figure 3.2: Surface roughness characterization of surface roughness using AFM tapping mode.

a) AFM phase images were taken along 30/70 pDTEc/pDTOc roughness gradients at an interval of 2.5 mm. The five positions selected are represented by p1 through p5. **b)** Comparison of different RMS roughness (computed from AFM height images; n=4) along annealing temperature gradients of the respective pDTEc/pDTOc blend compositions. The RMS roughness of the respective polymer blends decreases monotonically with composition as the temperature approaches the glass transition temperature of p(DTE)c. The RMS roughness of homopolymers (pDTEc or pDTOc) stays constant at 1~5 nm along

annealing temperature gradient. The dotted vertical line indicates the extremity of the range of roughness conditions shown in Panel 2(a).

3.3.2 Cellular Attachment and Adhesion Evaluation

Rapid screening of cell population-level adhesive responses was conducted through tile-scanning of images of Saos-2 GFP-f adherent cells to different regions of the polymer roughness gradients. Cells were found to attach in greater numbers to the pDTEc than to the pDTOc (**Figure 3.3 and 3.4**). As both homopolymer surfaces were relatively smooth, these variations in cell attachment are likely due to differences in polymer hydrophobicity and protein adsorption[16]. The homopolymer pDTOc has a longer hydrocarbon pendant chain and is more hydrophobic than pDTEc. This result is consistent with previously reported *in vitro* and *in vivo* studies demonstrating an inverse correlation between cell adhesion, spreading, and growth, and polymer hydrophobicity[100,252,259].

With regards to surface features, Washburn *et al*. reported that cells on the 12 nm rough surface exhibited increased spreading, more readily entered into the proliferative S-phase, and showed more profuse F-actin organization compared to those on the 1 nm rough surface[260]. This study suggests that cell proliferation and cytoskeletal organization are controlled by the nanometer scale topography. The present study showed that for a given blend composition, the cell attachment increased monotonically with the degree of surface roughness until the RMS value reached 30 to 40 nm in the 50/50 pDTEc/pDTOc blends (data not shown). However, cell attachment to the surfaces with RMS roughness values greater than 40 nm was diminished. While, a similar pattern was observed

for cell attachment on 70/30 and 30/70 pDTEc/pDTOc blends, the greatest overall cell attachment was observed on the 50/50 blends.

Further, we observed that the locations in the pDTEc/pDTOc blends with the most significant changes in topography slope, about (5 to 10) mm along the roughness, exhibited RMS roughness values of (30 to 40) nm and maximum cell attachment. Whether the roughness gradient steepness is a significant determinant of cell attachment and spreading remains to be confirmed. Our substrates presented both varying roughness and roughness gradient steepnesses on different blend compositions, so the roles of roughness and the gradients need to be decoupled. We examined whether cell adhesion profiles are governed by a specific gradient steepness of roughness, an index defined as steepness of roughness gradient divided by average degree of local roughness (**Figure 3.4**). This index allows comparison of roughness gradients over regions of varying average roughness. Three trends appear to emerge. In general, regions with greater specific gradient steepness of roughness correlated with increased cell adhesion, suggesting that (apart from degree of roughness), the degree of gradient of roughness is a likely determinant of cell response. Second, the slope of the linear best fits to **Figure 3.4** (see equations in caption for **Figure 3.4**) was greatest for the 30/70 pDTEc/pDTOc blend composition, suggesting that the gradient steepness has the most pronounced effect on cell adhesion on the pDTO-rich blends, consistent with the notion that the homopolymer pDTOc elicits lower levels of cell adhesion. Finally, the 50/50 pDTEc/pDTOc blends showed variable cell adhesion for similar values of specific gradient steepness,

suggesting that the roughness gradient steepness is a weaker determinant than the average degree of roughness and blend chemistry for this blend composition. The 50/50 blends had the greatest overall cell adhesion (**Figure 3.3&3.4**) at comparable roughness and lower roughness gradient steepness than the other blends and greater adhesion than either of the homopolymer substrates. This seems to support the dominance of blend chemistry in cell adhesion behavior in the 50/50 composition.

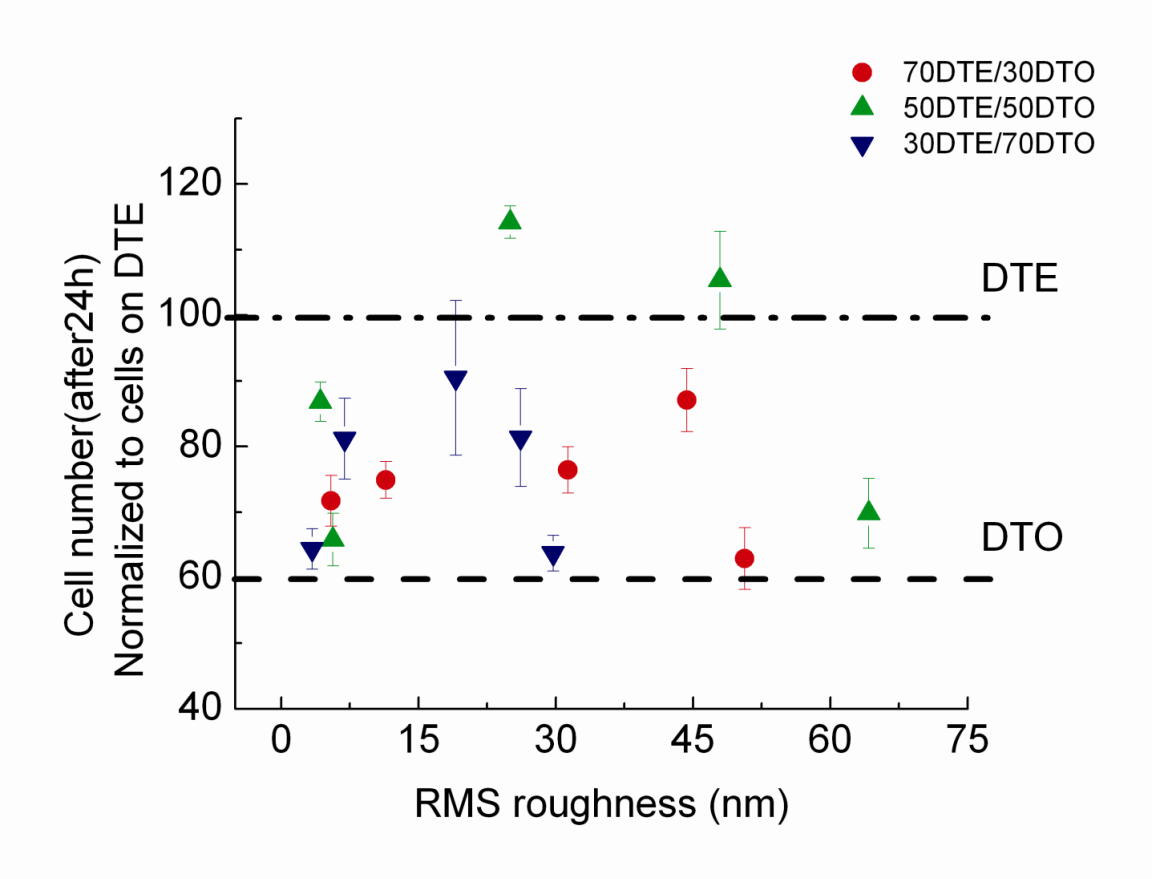

Figure 3.3: Degree of cell adhesion (24 h) was plotted versus RMS roughness on the substrates with roughness gradients.

Cell adhesion was analyzed at 5 different locations spaced 5 mm apart for each compositional strip. The number of cells attached to roughness gradient

displayed a biphasic correlation with the RMS roughness of the substrate surface.

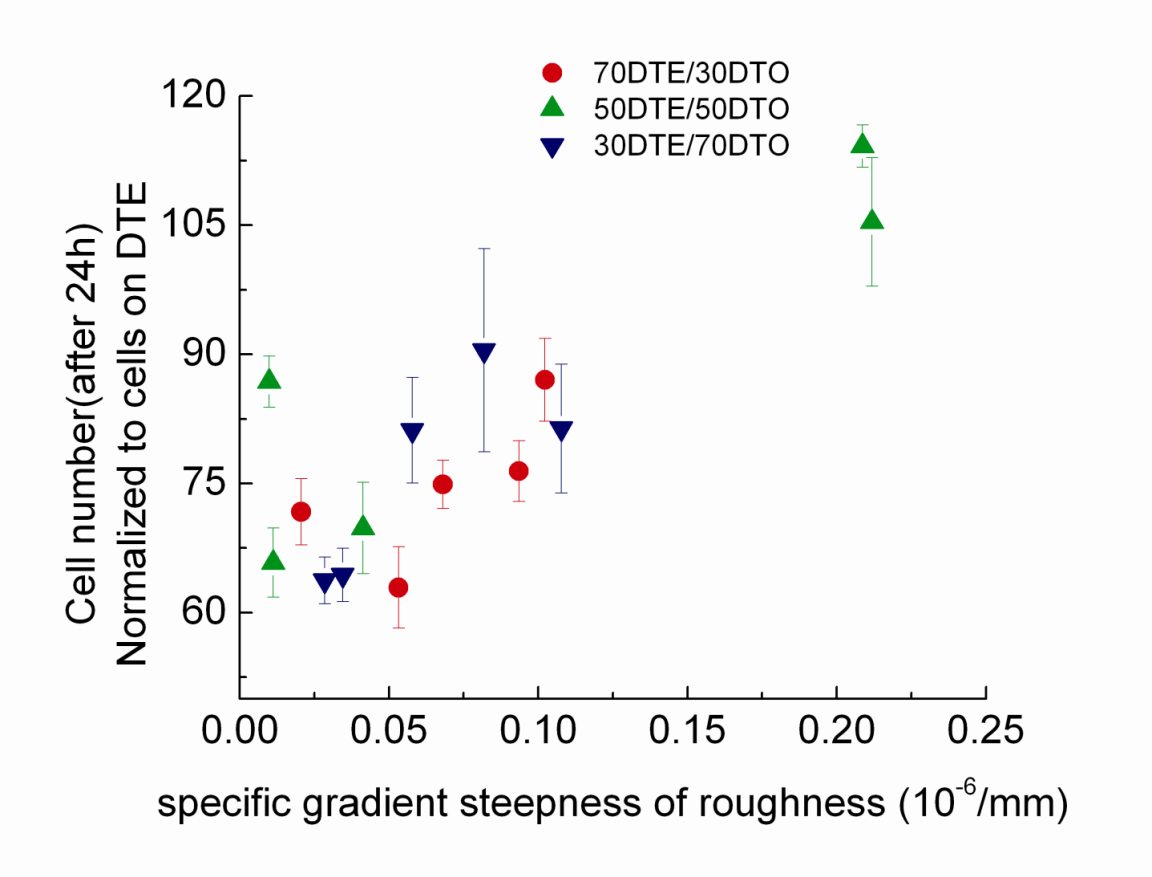

Figure 3.4: Cell adhesion (24 h) was plotted versus the specific gradient steepness of roughness, an index that corrects for varying degrees of roughness in different regions of the gradient steepness.

The number of cells attached to different positions on the substrates and different blend compositions are correlated with the "normalized" gradient steepness of the substrate surface. The best fit equations for the three compositions are: 70DTE/30DTO: y=62.3+182.45x, R=0.69; 50DTE/50DTO: y=70.87+181.54x, R=0.89; 30DTE/70DTO: y=58.65+283.25x R=0.80

The degree of cell adhesion strength was measured indirectly by counting the number of cells that still remained on the substrate after differential centrifugal fields (**Figure 3.5 a&b**). The detachment curves demonstrated that the cells adhered more strongly to the rough surfaces than the smooth surfaces for a given composition; this was indicated by the decreased absolute value of the slope of the detachment curve, as compared to the slope of graphs obtained from the smoother surfaces in **Figure 3.5**. Notably, cells adhered more strongly to the 50/50 pDTEc/pDTOc blends than to pDTEc, indicating that polymer composition and roughness can cooperatively sensitize cell adhesion and cytoskeletal organization. Our rapid screening studies also revealed that cell adhesion force increased monotonically with the surface roughness of the substrate on all the blends (**Figure 3.3**). In contrast, we found biphasic patterns in both cell attachment and spreading, as evidenced by the fact that both cell attachment and spreading increased significantly at the position with intermediate roughness (RMS value: ~ 40 nm) as compared to other positions with higher or lower levels of roughness.

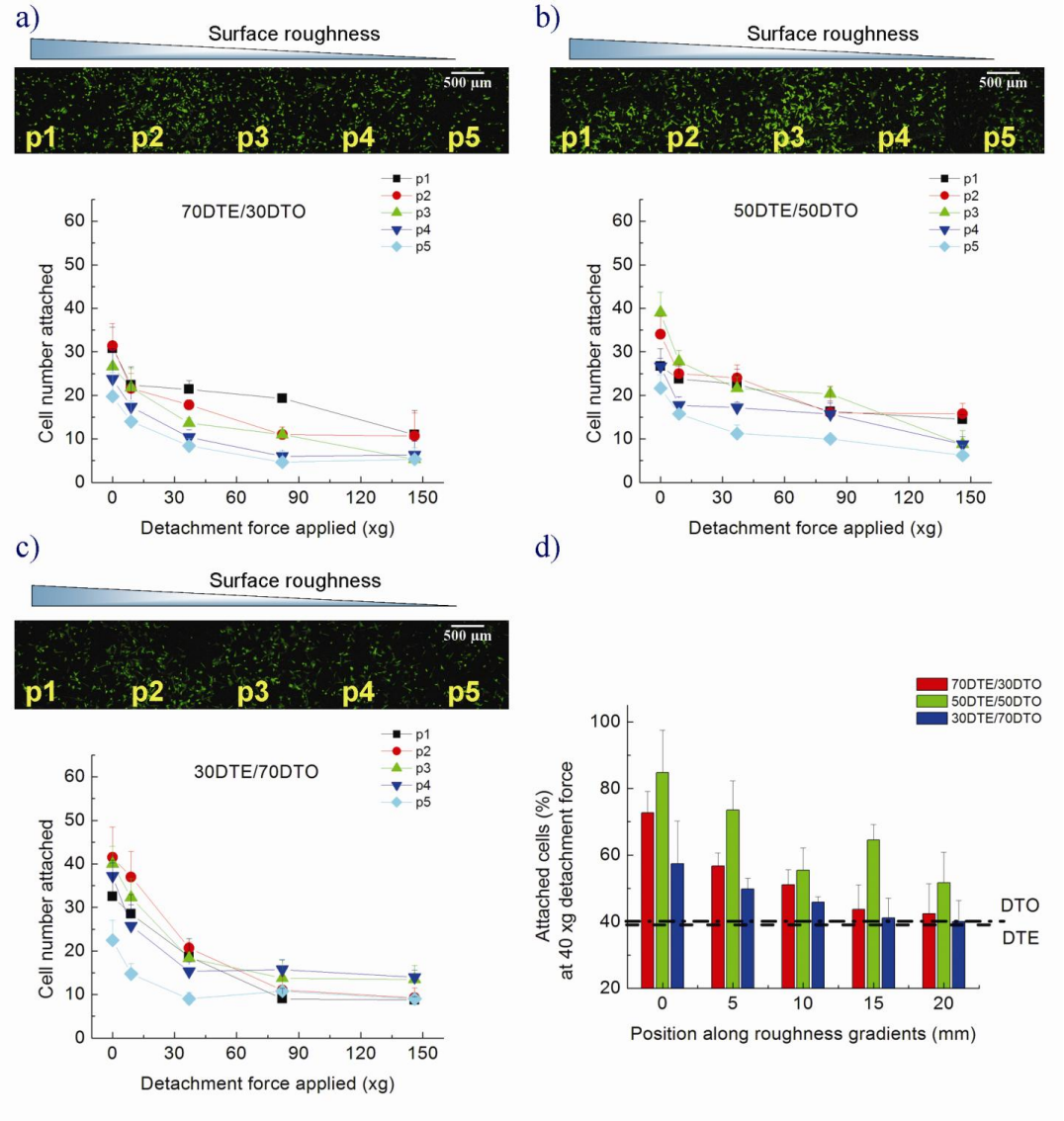

Figure 3.5: Saos-2 GFP-f cell adhesion force measurement using high throughput imaging.

(a-c) Saos-2 GFP-f cells were seeded on roughness gradients, incubated for 1h and centrifuged at 200~800rpm (9~137xg). Tile-scans were constructed for each of the substrate gradients with the 10x objective of a Leica TCS SP2 CLSM/MPM microscope. Cell number of GFP fluorescencent cells was determined by counting the number of fluorescent cells remaining. The 5 positions noted (p1-p5) refer to 5 positions (see **Figure 3. 2**) along each

composition spaced 5 mm apart. Position 1 corresponds to the roughest portion of the gradient, while position 5 corresponds to the smoothest. A montage of the gradients of each pDTEc/pDTOc composition after centrifugation was reconstructed based on the tile-scanned images (1.5 x1.5 mm) in ImageJ. A single example of one of these montages before centrifugation is shown for the 70/30, 50/50 and 30/70 pDTEc/pDTOc blends (a-c respectively). The tile scan images were then used to determine the number of cells remaining after centrifugation under differential forces for the respective blends. The cell adhesion force monotonically increased with RMS roughness of the surface within individual compositions. **(d)** The number of cells remaining after application of 40 xg detachment force was compared across polymers. The 50/50 blend demonstrated the greatest adhesion force at 40 xg.

The mechanistic factors underlying the role of roughness on cell adhesion and spreading are not entirely clear. However, one key link may be through the regulation of adsorbed extracellular matrix proteins from the culture environment, which in turn may be altered on microphase separated substrates with varying chemistry and hydrophobicity. A number of published reports as reviewed by Wilson et al. indicate that the nano-scale surface roughness regulates the cell attachment and adhesion force through protein adsorption onto the substrate surface: the geometry and chemistry that are changed by the roughness formation can influence the concentration, conformation, and activity of the adsorbed proteins[261].

3.3.3 High-content Single Cell Imaging on Substrates with Roughness Gradients

Cell population level differences on substrates with incremental variations in surface physiochemical proprties can be too subtle to be captured by high throughput or rapid screening. For such applications, information-rich high content imaging is called for. Recently, Treiser *et al*. published a technique whereby quantitative descriptors of cell morphology are used to parse cell response to combinatorial polymer materials with differing chemistry[47]. This study employed a similar technique to identify descriptors of cellular morphometry, which were responsive to changes in the substrate roughness.

The high-resolution imaging of the single cells and its quantitative image analysis were used to screen the multiple cellular responses to the roughness gradient surfaces. The cell morphology and spreading changed continuously along both the roughness gradient axes (**Figure 3.6**). At the smooth end of pDTEc-rich compositional regions, the cells spread more relative to the hydrophobic pDTOc-rich surfaces. This finding is consistent with reports from a previous study[252]. The fact that pDTEc increases cell-substrate adhesion more than cell-cell cohesion as proposed by Ryan *et al*. might account for the different cell behaviors elicited by the two polymers[262]. The maximum cell spreading was observed at the intermediate position at RMS roughness of (30 to 40) nm in the 50/50 pDTEc/pDTOc blends.

The Saos-2 cells were cultured on pDTEc/pDTOc blends with roughness gradients, and the cell areas were computed (**Figure 3.6**). The surface

roughness behaved in a threshold-like manner; regions containing RMS roughness values greater than 5 nm resulted in larger cell areas for the textured pDTEc/pDTOc blends as compared to the non-textured homopolymers. The RMS roughness exceeding 5 nm led to no significant difference in cell area. In fact, while the surface features ranged from 4.3 nm to 64.2 nm in RMS height (positions located (0 to 15) mm), the cell area remained relatively constant except in a few positions on the 50/50 roughness gradient. One of the key findings of our high-content imaging is that, whereas the cell area is responsive to the "presence" of surface topography[102], it lacks sensitivity to differences in nanometer scale surface features[255].

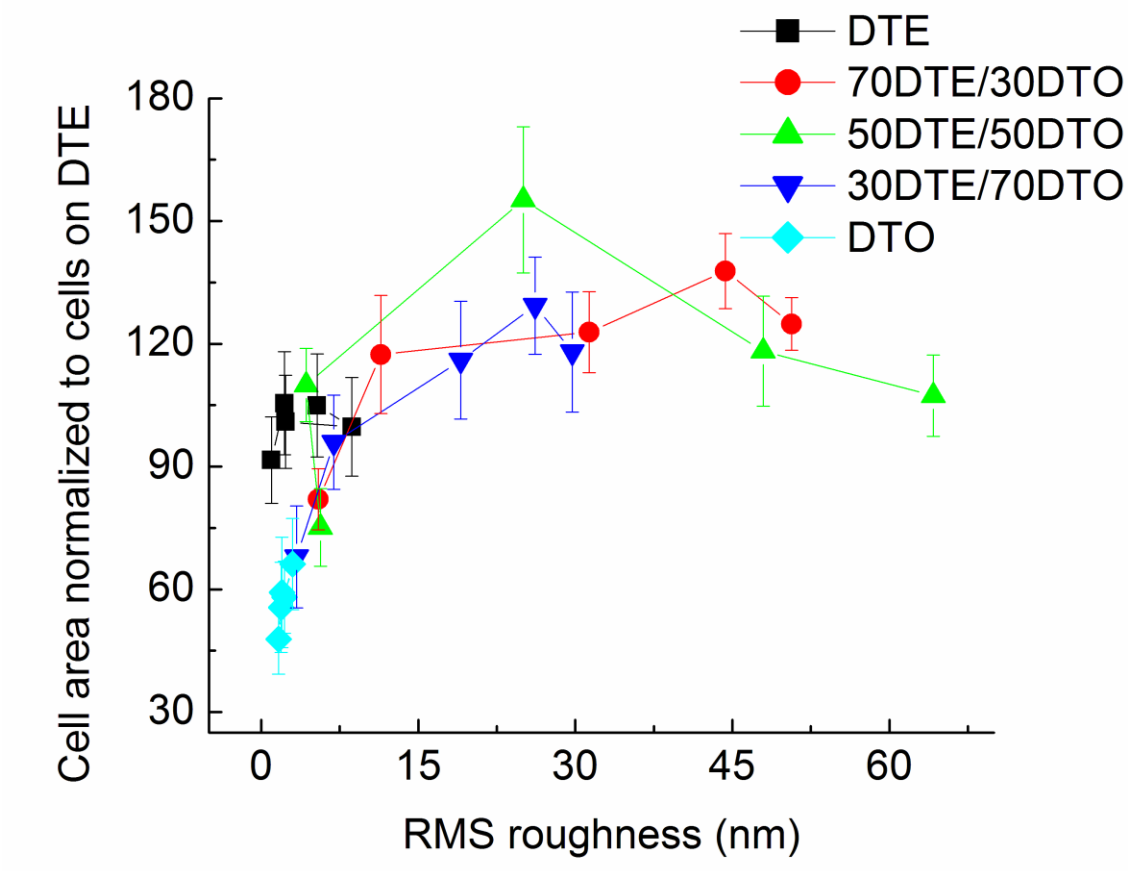

Figure 3.6: Normalized cell area versus roughness.

Cell area was utilized to characterize the spreading behavior of Saos-2 GFP-f cells cultured on the two dimensional gradients for 24 hours. Similar to 24 h cell attachment, Saos-2 GFP-f cell spreading displayed a biphasic correlation to surface roughness across compositions with intermediate roughness promoting the largest cell areas. (n =15 to 30 cells per condition).

Because the cell area correlated poorly with changes in the surface roughness, high-content image processing and statistical analyses were particularly valuable to potentially identify other cell morphometric parameters that were sensitive to the changes in roughness within individual chemistries. We found two such parameters: "perimeter length" of GFP-f on the 70/30 and 30/70 pDTEc/pDTOc blends, and the "standard deviation of the intracellular intensity" of GFP-f on 50/50 pDTEc/pDTOc blends, which correlated well with the changes in the surface roughness (**Figure 3.7**). While the perimeter is often used in combination with cell area to measure cell spreading, we report that only the cell perimeter length was responsive to the surface roughness. Since surface roughness can modulate cell response by affording increased anchor sites for cellular membrane processes[263,264], changes in the membrane function of the Saos-2 cells might be guided by the roughness gradient and then coordinate changes in global cell shape. The protein farnesylation has been implicated in alteration of both the cytoskeleton organization and cell functions via the activity changes of the Rho and Ras protein family[265,266]. An activation of this protein family and their downstream effectors is an important event in the

actin-myosin operation and focal adhesion assembly, both of which play a significant role in actin cytoskeleton organization and cell adhesion[151,267,268]. The standard deviation of farnesylation intensity, the second high-content parameter that our analysis yielded, may reflect some aspect of cellular farnesylation activity and thus implicate a direct or an indirect role for protein farnesylation in the signaling events downstream of cell adhesion to our gradient substrates. It should be noted that this parameter was correlated with the variations in the surface roughness of the 50/50 blends, but it was not as well correlated on the other compositional blends. Interestingly, the 50/50 blends were the substrates that elicited the greatest increase in cell response to the increase in surface roughness. Of note, while the statistically significant ($p<0.05$) correlation coefficients for surface roughness were found for all of the blends, the value of the coefficients was low (< 0.90) for the 70/30 and 50/50 pDTEc/pDTOc blends (**Figure 3.7**). The pDTEc represents a polymer surface composition that promotes favorable spreading and attachment of cells in comparison to pDTOc[252]. The low values of the correlation coefficients for the blends with $\geq$ 50 % pDTEc content may indicate that the increased presence of pDTEc lowers the ability to resolve cell morphologic changes that result from roughness alone. This would imply that the chemistry effect of the pDTEc dominates over the changes in the surface roughness. However, in polymer conditions composed of more pDTOc (e.g. 30/70 blends), the surface roughness effects on cell morphology may be resolved.

A major challenge in biomaterials characterization remains how to relate qualitative and quantitative changes in cell morphology to biological functions of interest. While the cell area provides a qualitative measure of cell behavior, quantitative correlations and the possibility that other cell morphometry-based descriptors will correlate with greater sensitivity and accuracy must be explored. By utilizing high-content imaging, descriptors that correlated best with 1 h cellular attachment were identified (**Figure 3.7**). Briefly, a bivariate correlation coefficient was calculated (Pearson correlation coefficient) utilizing SPSS software. Correlation coefficients that were found to be statistically significant ($p<0.05$) were flagged and identified. The heat map compares the descriptors on all of the surfaces against those on single smooth control surfaces, but it does not make comparisons among the different degrees of roughness. Therefore, while the descriptor can be statistically different on all values of roughness versus the smooth surface, they could all have the same value on the different values of roughness and therefore have a poor correlation coefficient. Since the heatmap does not represent the value of the descriptor, it alone is not able to identify which descriptors best correlate linearly with roughness, hence necessitating the use of statistical analysis. Overall, the cell area was found to be a reliable predictor of cell attachment on the 50/50 blends but was not well correlated with attachment on the 70/30 and 30/70 pDTEc/pDTOc blends. However, the cell roundness and the length of the major axis of cells correlated with the 1 h cell attachment on the 70/30 and 30/70 pDTEc/pDTOc blends, respectively. The identification of descriptors that describe cell behavioral polarity as those that

correlate best with early cell attachment implicates global cytoskeletal organization as a dominant mediator or effector of early cell attachment to textured substrates.

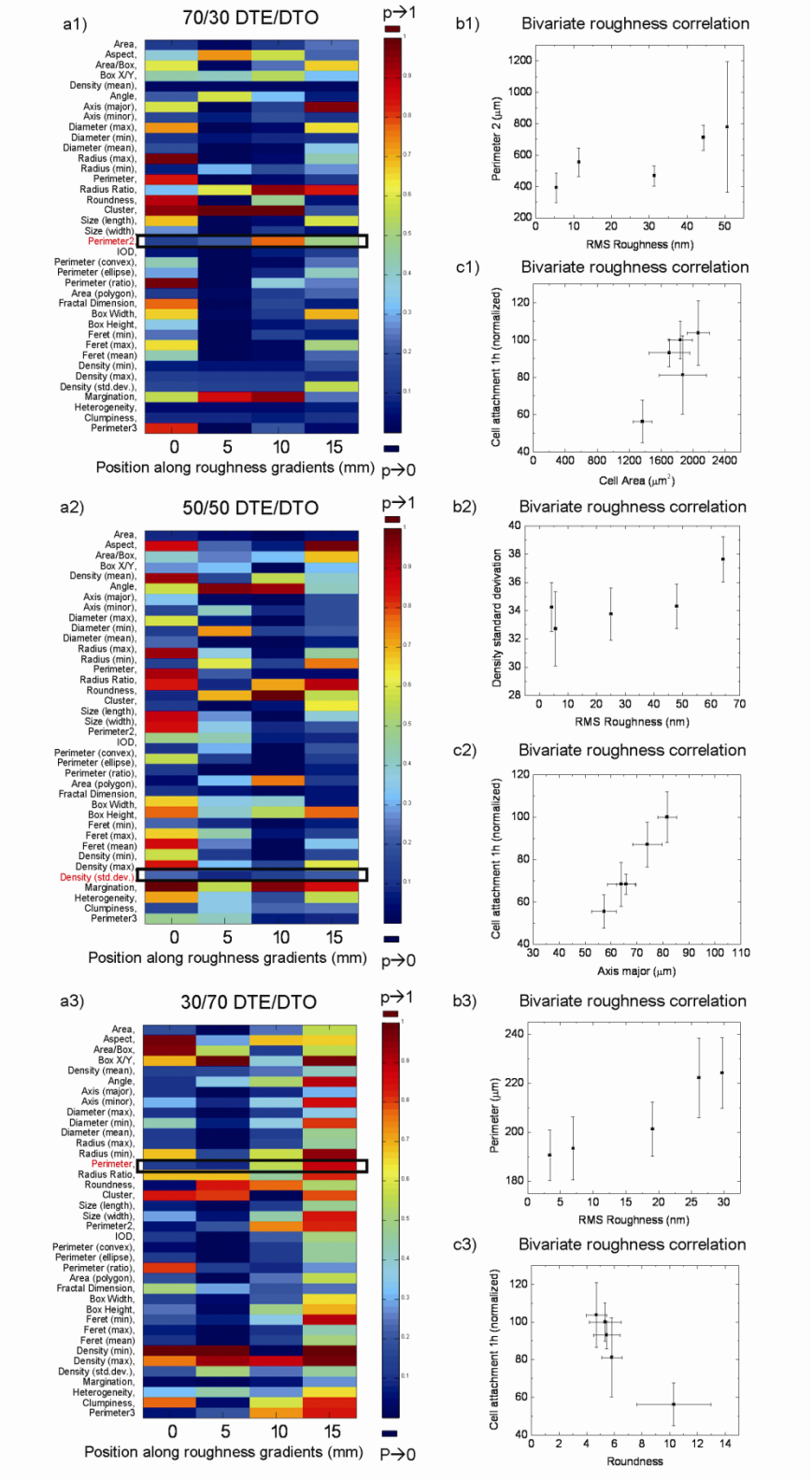
a1)
70/30 DTE/DTO
p→1
p→0
Position along roughness gradients (mm)
b1)
Bivariate roughness correlation
Perimeter 2 (μm)
RMS Roughness (nm)
c1)
Bivariate roughness correlation
Cell attachment 1h (normalized)
Cell Area (μm²)
a2)
50/50 DTE/DTO
b2)
Bivariate roughness correlation
Density standard deviation
RMS Roughness (nm)
c2)
Bivariate roughness correlation
Cell attachment 1h (normalized)
Axis major (μm)
a3)
30/70 DTE/DTO
b3)
Bivariate roughness correlation
Perimeter (μm)
RMS Roughness (nm)
c3)
Bivariate roughness correlation
Cell attachment 1h (normalized)
Roundness

Figure 3.7: Quantitative characterization of cell shape descriptors and morphologic expression of GFP-farnesylation using cell morphometric descriptors.

a*) A 'heatmap' demonstrates the difference along roughness gradients of different pDTEc/pDTOc compositions. Cell population descriptors were determined for cells (15-30 cells per position) cultured at different locations along individual roughness gradient positions (0, 5, 10 and 15 mm) within compositional blends. An ANOVA with post-hoc Tukey's HSD was utilized to determine differences in mean values of cell population descriptors as compared to the mean values of population descriptors on smooth surfaces of the same composition. The "heat map" representation identifies the statistical differences (P-value) between descriptor values comparing positions of increasing roughness and smooth positions utilizing a color-based keying system. A strong statistical difference in descriptor value (ANOVA p value approaching 0) is represented by blue, while no statistical difference (p value approaching 1) by red, an intermediate color between dark blue and red indicates moderate statistical difference (p value between 0 and 1) The heat map does not compare the mean values of descriptors between different levels of roughness within the same compositions, nor do the color bars correlate to the direction of the difference. b*) Identified descriptors that are sensitive to changes in surface roughness within polymer chemistries. Cell perimeter2 (another method of calculating perimeter of a cell), density (GFP-f fluorescent intensity normalized to cell area) standard deviation and perimeter were identified as descriptors that

were sensitive to surface roughness of 70/30, 50/50 and 30/70 pDTEc/pDTOc respectively. **c*)** Identified descriptors that are well correlated to short term cell attachment. The 1h cell attachment was intercorrelated to cell area, axis major and roundness of 70/30, 50/50 and 30/70 pDTEc/pDTOc respectively. ***1)** represents polymer blends with 70/30 pDTEc/pDTOc; ***2)** represents polymer blends with 50/50 pDTEc/pDTOc; ***3)** represents polymer blends with 30/70 pDTEc/pDTOc.

Perhaps most striking about the presented findings is the identification of individual measures of cell shape that are sensitive to and correlate with surface topography and cellular behaviors. Typical qualitative analysis may identify elongation as a hallmark of surface roughness, but this relationship lacks reproducibility and is insensitive to small changes in material properties. The high-content imaging of cells cultured on the dual-gradient substrates permitted the identification of cell shape descriptors that are sensitive to either roughness or surface wettability (**Figure 3.7**). The polygonal area of the cell was found to correlate with the surface energy of the material, while the perimeter length of the cell and the standard deviation of the intensity of GFP-f were all found to correlate statistically with the surface roughness. Current studies suggest that cell morphology and the generation of cytoskeletal tension are key regulators of cell function and signaling. Cell studies have highlighted the mechanisms by which the cell shape regulates cell cycle progression, apoptosis, and differentiation[138,150,269,270]. If cell shape is an essential regulator of cell response

to materials, then detailed quantitative analysis of cell morphology, as presented in this study, may provide new insights to determine how material chemistry and roughness interact to produce observable differences in the cell behaviors.

3.4 Conclusion

In this study, we employed both rapid screening and high-content imaging, two complementary approaches, to examine cellular adhesion and morphogenesis on compositionally differing substrate blends of two members of tyrosine-derived polycarbonates that possess a gradient in phase-separation which induce several surface variations including hydrophobicity, individual polymer component and surface roughness. The adhesion of Saos-2 cells was rapidly screened via tile-scanning and was found to be maximized at intermediate regions, characterized by intermediate levels of roughness and the steepest roughness gradient. Through high-content imaging, we identified different morphometric parameters of the organization and intensity of GFP-f that correlate best with the most adhesive substrate compositions (chemistry) or with the degree of surface roughness. We examined the correlations between the defined parameters and the cell functions (e.g. early cell adhesion) obtained by rapid screening. Thus, by using a combination of high-throughput and high-content analysis, we demonstrated that quantitative descriptors of cell fluororeporters can be effectively identified to parse the biologically responsive properties of a library of polymer substrates.

4 Cell Cytoskeleton and Nucleus Based High Content "Composite" Profiling on Stem Cell Differentiation and Self-Renewal

Note: Part of this chapter is reproduced from the following publication:

Er Liu, Simon Gordonov, Matthew Treiser, and Prabhas Moghe. Parsing the early cytoskeletal and nuclear organizational cues that demarcate stem cell lineages. Cell Cycle. 9: 2108 – 2117 (2010). Used by permission.

4.1 Introduction

Stem cells have garnered interest in the field of regenerative medicine due to their ability to differentiate into distinct functional tissue types. In particular, human mesenchymal stem cells (hMSC), isolated from bone marrow or adipose tissues have been extensively characterized with regards to their multi-lineage differentiation capabilities[53,271-273]. A variety of exogenous cues have been investigated to manipulate stem cell differentiation, including soluble growth factors[274], substrate composition[275], and underlying matrix compliance[276]. hMSC differentiation behaviors, particularly those toward osteogenic and adipogenic lineages, were reported to be influenced by overall cell shape and regulated by RhoA GTPase activity and cytoskeletal tension[138]. Therefore, our laboratory members utilized the high content imaging platform developed in Chapter 3 to screen the actin cytoskeletal organization of hMSC to discern heterogeneous subpopulations exposed to osteogenic versus adipogenic induction cues[277]. This profiling methodology utilizes quantifiable higher-order actin cytoskeleton organization features to parse individual stem cells at time points as early as 24

hours that commit to different long term fates (**Figure 4.1**). The early identification of stem cell lineage commitment based on quantification of cytoskeletal features demonstrates significant advantages over cell population pooled assays like PCR analysis, which cannot identify the heterogeneity of differentiation within a particular condition on an individual cell basis.

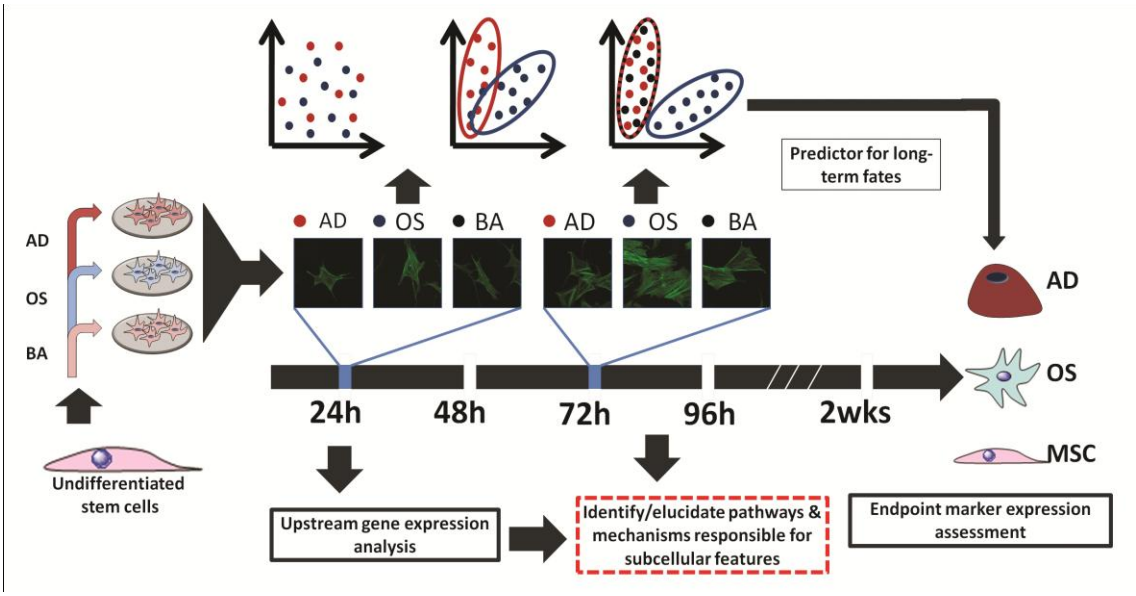

Figure 4.1: Deciphering early genes and cellular morphometrics governing long-term stem cell lineage fates.

A new approach based on high content imaging was recently proposed to resolve early cytoskeletal organization as a basis to discern differential lineage outcomes and track lineage specification in human mesenchymal stem cells. Early cytoskeletal organization parsed cells cultured within osteogenic (OS) versus non-osteogenic conditions but failed to discriminate, even at later times, between adipogenic (AD) and basal (BA) conditions.

Despite its ability to successfully parse out heterogeneities in cytoskeletal architecture of adipogenic (AD) and osteogenic (OS) treated hMSC, this methodology was unable to effectively distinguish adipogenic lineage committed hMSC from non-differentiated hMSC treated with basal growth media (BA) using cytoskeletal features alone. The cell cytoskeleton itself is not isolated, but is actively linked to the cell nucleus. The eukaryotic cell nucleus is a membrane-enclosed compartment containing the genome and associated molecules supported by a highly insoluble filamentous network known as the nucleoskeleton or nuclear matrix, which is believed to play a role in maintaining nuclear architecture and organizing nuclear metabolism. Previous studies have shown that within the cell nuclear matrix domains there are dynamic nuclear transactions between both soluble and insoluble components involving in the control of multiple nuclear transactions[17,278-281]. Similar to the cytoplasm and its skeleton, the nucleoplasm is highly structured and very crowded with an equally complex skeletal framework. Increasing evidence shows that the two skeletal systems are functionally contiguous, suggesting a dynamic cellular matrix connecting the cell surface with the genome[280]. With regards to stem cell differentiation, previous studies have demonstrated that although the genome is maintained within the nucleus when stem cells undergo differentiation processes, the shuttling of macromolecules between the nucleus and the cytoplasm permits a constant exchange of information and materials necessary for the control of gene expression[282]. Moreover, studies also report a link existing between

nuclear structure and cell adhesion complexes that are responsible for the cell's interaction with extracellular components through the cytoskeleton[283-286].

Collectively, the cell nucleus, in addition to the cell cytoskeleton, could potentially provide alternative clues in capturing stem cell differentiation versus self-renewal. To this end, we utilized DNA microarrays to probe whether nuclear and cell cycle related genes in hMSC were differentially up-regulated after exposure to differentiation/growth medium conditions. Clear variations were observed in cell proliferation rates and a number of key nuclear transport and cell cycle proteins, suggesting that nuclear events are sensitively influenced early on prior to lineage commitment. A major goal of this study was to extend the high content imaging-based profiling platform discussed in Chapter 3 beyond the cytoskeleton to include the nuclear organization as well. A good candidate nuclear protein for nuclear profiling was determined to be the nuclear mitotic apparatus (NuMA). NuMA is a nuclear matrix protein closely related to cell cycle progression through tethering spindle microtubules to their poles during mitosis. It has also been linked to nuclear transport components in interphase and mitosis and plays a role in spindle positioning and asymmetric cell division (stem cell differentiation versus self renewal) [17,131,164,165,287]. Based on these findings, NuMA organization and expression may mirror changes in differentiation and cancerous progression (will be addressed in the next chapter), and is acutely affected by the redistribution of histone acetylation and histone methylation patterns, prior to cellular phenotypic changes[131,165]. Thus, a composite, cytoskeletal-nuclear organization based high content imaging approach was

applied, demonstrating that early variations in hMSC within distinct lineage inductive environments could be more sensitively discerned.

4.2 Materials and Methods

4.2.1 Cell Culture

Human mesenchymal stem cells (hMSC) were obtained from commercial sources (Lonza; Walkersville, MD). Cells were cultured in a humidity-controlled environment under 5% CO_2 and 37°C and fed every 3-4 days with growth media (basal media) supplemented with commercial SingleQuot's© (Catalog # PT-3001, Lonza). Cells were received at passage 1 and used for up to 4 passages. Cells were subcultured upon reaching 90% confluence. Osteogenic induction (OS) and adipogenic induction/maintenance (AD) media were reconstituted as per manufacturer (Catalog #'s PT-3002 and PT-3004 respectively, Lonza). Adipogenic media was cycled with 3 days induction followed by 1 day maintenance.

4.2.2 hMSC Differentiation on Fibronectin-Coated Glass Substrates

Fibronectin- (BD Biosciences; Franklin Lakes, NJ) coated glass substrates were created via the application of 400 μL of 25 μg/mL phosphate buffered saline (PBS) solution to each well of a glass bottom 24-well plate for 1 hour at room temperature. Bone marrow derived hMSC (Source: Lonza Inc.) were applied at 10,000 cells per cm^2 and allowed to attach in basal medium for 4 hours. After the 4-hour attachment period, the basal medium was replaced with appropriate

induction media. For differentiation assays, cells were cultured for 2 weeks and then stained for alkaline phosphatase activity and lipid production as described in the cell labeling section.

4.2.3 Gene Microarray Analysis of hMSC under Induction Media

At 4 hour and 24 hour time points after hMSC were cultured on fibronectin-coated glass and treated with induction media as described previously in induction media, total mRNA was extracted (Catalog # 74106, Qiagen; Valenica CA) and reverse transcribed to produce a cDNA library (Catalog # 4374966, Applied Biosystems; Foster City, CA). Gene microarrays were analyzed using Affymetrix Microarray System. Additionally, microarray data normalization, gene selection, and hierarchical clustering from the values produced in the microarray chip readout was performed using dChip (www.dchip.org, freeware version 8/7/09). This processed data was used to identify genes of most variable expression between media condition treatments and time points. Briefly, normalization was performed to baseline intensity from one of the microarray chip files that displayed median intensity values on the chip image file. Replicate groups were designated per time point and media condition (10 total samples combined in duplicate into 5 conditions based on media and time point). Unsupervised sample and gene clustering was used to identify and visualize sample clusters and their signature genes from specific gene ontologies. Standardization across conditions was performed by subtracting the mean and dividing by the standard deviation. The distance metric between genes was defined as 1-r, where r is the Pearson correlation coefficient between

the standardized gene expression values across samples. Genes were ordered by cluster tightness and the centroid linkage method was used to produce the cluster plot. Dimensionality reduction (PCA) of the gene data sets for visualization in 3-D of cross-conditional variability in gene expression was performed using Matlab's (Mathworks) statistical toolbox. In particular, each principal axis in the graph represents a linear combination of all the genes shown in the clustering analysis. Different weights were placed for each variable to produce an increasing contribution of each consecutive principal axis (1, 2, and 3) to the variability in gene expression between media treatment conditions.

4.2.4 Cell Labeling

Functional marker staining: to stain alkaline phosphatase, cells were fixed with 4% paraformaldehyde in PBS, permeabilized with 0.1% Triton-X 100 in PBS, rinsed with PBS and stained with Fast Blue RR/napthol (Kit # 85, Sigma-Aldrich; St. Louis, MO). To stain intracellular lipids, cells were washed with 60% isopropanol and then stained with 30 mg/mL Oil Red O (Sigma).

Subcellular protein staining: prior to the addition of the primary antibody to NuMA, cells were permeabilized using a buffer of 0.1% Triton X-100 in PBS for 30 minutes. Mouse anti-human primary antibodies were used at a 1:50 dilution in 5% goat serum in PBS to mitigate non-specific binding. Each well received 75 µL for 1 hour at room temperature on rocker. Primary antibody was then removed and three 10 minute washes were performed with washing buffer (0.1 % Tween-20, 0.01% Triton X-100 in 1x DPBS). The secondary antibody used was

Alexa488 goat-anti-mouse at a dilution of 1:200 in washing buffer overnight at 4°C on rocker. The actin cytoskeleton was stained with Phalloidin TexasRed (Invitrogen). Cell nuclei were counterstained with 1 μg/mL Hoechst 33342 (Sigma). Samples were washed with PBS, mounted in fluoroguard anti-fade reagent, and stored in the fridge before imaging on a Leica Multiphoton/Confocal Microscope.

4.2.5 High Content Imaging-Based Profiling Platform Build-up

The overall high content imaging-based profiling platform is composed of three modules: high resolution cell imaging and microscopy module, subcellular feature extraction module and data mining module (**Figure 4.2a**), as described in the following paragraphs:

Confocal/Multiphoton Microscopy and Subcellular Feature Extraction of Cells

Fixed and stained cell samples were imaged using a 63X objective (NA = 1.3) with a Leica TCS SP2 system (Leica Microsystems Inc.; Exton, PA). Various fluorophores were excited either through visible laser (single photon excitation) or IR laser (two photon excitation). The excitation and emission setup parameters of the microscope are listed in **Table 4.1**. Optical sections were performed on cells with ~20um thickness using a step-size of 0.5um; average projection images were generated using a collection of these z-stacks for image analysis. Raw images of cells were exported to Image Pro Plus Version 5.1 (Media Cybernetics; MD) and went through a series of image processing steps

including: background subtraction, contrast enhancement, filtering, and segmentation to ensure that reporters of interest within the whole cell or cell nucleus were selected. These reporters were then used to yield three categories of subcellular features: decoding reporter protein expression (intensity-based), reporter morphology (morphometrics), and texture and spatial distribution (higher order elements) of the reporter. This cell/nucleus reporter data was then exported to an Excel spreadsheet for further analysis (**Figure 4.2b**).

Table 4.1: Excitation and emission setup of fluorophores used in the thesis

Fluorophore name	Excitation max [nm]	Emission max [nm]
Hoechst 33342	780 (two-photon excitation)	483
Alexa Fluor 488	494	519
Alexa Fluor 546	554	572
Alexa Fluor 633	632	648
Alexa Fluor 647	652	668
Alexa Fluor 594	591	618

Table 4.2: List of Cell Nuclear Descriptors

This table lists a pool of cell nuclear descriptors quantified for each cell. The definition of the feature and its possible biological relevance is listed. Nuclear morphology features are highlighted in red, intensity based features are highlighted in yellow, and textural/spatial organizational features are highlighted in blue.

Nuclear Features	*Description*
Angle	Reports the angle between the vertical axis and the major axis of the equivalent ellipse. Within the context of this study it would capture randomly oriented versus aligned cell nuclei, which might be indicative of cell orientation itself.
Area	Reports the total area of each cell nucleus.
Polygonal Area	Reports the area of the polygon that defines the object's outline. Anorhter metric measurement for area of cell nucleus.

Area/Box	Reports the ratio between the area of each object and the area of the imaginary bounding box.
Aspect	Reports the ratio between the major and minor axes of the ellipse with the same area, first and second order moments. The simplest way to define the cell nuclear shape factor.
Axis (major)	Reports the length of the main axis of the ellipse with the same area, first and second order moments.
Axis (minor)	Reports the length of the minor axis of the ellipse with the same area, first and second order moments.
Box Height	Reports the height of the smallest bounding box that completely encompasses the whole cell.
Box Width	Reports the width of the smallest bounding that completely encompasses the whole cell.
Box Ratio	Reports the ratio between the Box Width and Box Height
Dendrites	Reports the number of 1-pixel thick open branches. Within the context of the whole cell, it represents stretching process of the cells (migrations). In nuclear reporters, such as nucleus matrix protein NuMA, it could represent the number of traslocation of NuMA between cell nucleus and extra-nuclear environment.
Dendritic Length	Reports the total length of all dendrites.
Maximum Diameter	Reports the length of the longest line joining two outline points and passing through the centroid of the cell nucleus.
Mean Diameter	Reports the average length of the diameters.
Minimum Diameter	Reports the length of the shortest line joining two outline points and passing through the centroid of the cell nucleus.
End Points	Reports the number of 1-pixel thick processes stemming from the cell nucleus.
Maximum Feret Length	Reports the longest caliper length.
Mean Feret Length	Reports the average caliper length.
Minimum Feret Length	Reports the shortest caliper length.
Fractal Dimension	Reports the fractal dimension of the cell nucleus's outline.
Cell Area/Total Area	Reports the ratio between the areas of the cell nucleus to that of the entire field of view.
Center-X	Reports the geometric center of the cell nucleus, X-cordinate.
Center-y	Reports the geometric center of the cell nucleus, Y-cordinate.
Center-X(mass)	Reports the intensity weighted centroid of the cell nucleus, X-cordinate.
Center-Y(mass)	Reports the intensity weighted centroid of the cell nucleus, Y-cordinate.
Perimeter	Reports the length of the outline of each cell nucleus using a

	polygonal outline.
Perimeter2	Faster but less accurate measure of the perimeter.
Perimeter3	Reports a corrected chain code length of the cell perimeter.
Convex Perimeter	Reports the perimeter of the convex outline of each cell nucleus.
Elliptical Perimeter	Reports the perimeter of the ellipse surrounding the outline of each cell nucleus.
Perimeter Ratio	Reports the ratio of the convex perimeter to the perimeter outline of each cell nucleus.
Maximum Radius	Reports the maximum distance between each cell nucleus' centroid pixel position and its perimeter.
Minimum Radius	Reports the minimum distance between each cell nucleus' centroid pixel position and its perimeter.
Radius Ratio	Reports the ratio between Max Radius and Min Radius for each object, as determined by Max Radius / Min Radius. Another shape factor metric for cell nucleus.
Roundness	Reports the roundness of each object, as determined by the following formula: (perimeter2) / (4 * π * area). Circular cell nucleus will have a roundness = 1; other shapes will have a roundness > 1. Standard metric for nuclear shape measurement.
Size (Length)	Reports the feret diameter (caliper length) along the major axis of the cell nucleus.
Size (Width)	Reports the feret diameter (caliper length) along the minor axis of the cell nucleus.
Minimum Density	Reports minimum intensity inside the object (cell nucleus).
Maximum Density	Reports maximum intensity inside the object (cell nucleus).
Segmentation range	Reports the intensity range that each object (cell nucleus) was segmented into.
Mean Density	Reports the mean intensity of all pixels within a cell nucleus. Correlates to the average amount of fluorescently tagged NuMA protein present within a given cell nucleus.
Sum of the Density	Reports the sum of the total intensity values of all pixels within a cell nucleus. Corresponds to the total amount of positive NuMA-staining within the cell nucleus.
Integrated Optical Density	Reports the average intensity of each object normalized by the area of the cell nucleus.
Standard Deviation of Density	Reports the standard deviation of the intensity of pixels within a cell nucleus. This represents the degree to which the NuMA protein is localized into cell nucleus of equal staining intensity.
Holes	Reports the number of independent contiguous areas with no staining within a cell nucleus. Also can be regarded as NuMA absent areas

Hole Area	Reports the area of holes within an object. Also can be regarded as total NuMA absent areas.
Hole Ratio	Reports the ratio of the object area excluding holes, to the total area of the object, as determined by Area / (Area + Holes Area). One metric that provide the degree of NuMA localization within cell nucleus.
Margination	Reports the distribution of intensity between the center and the edge of the cell nucleus. Describes the relative spatial distribution of NuMA within the cell nucleus.
Heterogeneity	Reports the fraction of pixels that vary more than 10% from the average intensity of the cell nucleus. One texture feature that describes how well NuMA proteins are organized winthin cell nucleus.
Clumpiness	The fraction of heterogeneous pixels remaining in a cell nucleus after an erosion process. Another spatial distribution feature that reflects the degree of NuMA protein clustering within cell nucleus.

Data Mining and Computational Methods to Parse Nuclear-Encoded Stem Cell Phenotypes

As described in the previous section, there is a large pool of quantifiable features of the cell nucleus and nuclear protein NuMA. Features that were defined include: cell nuclear morphological features, intensity-based features that relate to the expression level of NuMA protein, textural and NuMA organizational features that describe the spatial distribution of NuMA protein and their location within the nucleus. A complete list of the nuclear features and their relevance to the cell nucleus and NuMA protein is shown in **Table 4.2**. Due to the large numbers of nuclear descriptors for each cell, it's barely possible to visualize such a high dimensional dataset. Therefore, for better visualization of the cell descriptor data set, dimension reduction was performed using a variety of techniques such as linear methods (principal component analysis (PCA)), non-linear methods (Probabilistic PCA, Factor Analysis (FA), Multidimensional

scaling (MDS)) or embedding methods (Isomap, Local Linear Embedding (LLE), Laplacian Eigenmaps, Hessian LLE), all implemented utilizing Matlab's toolbox (Mathworks Inc. MA http://www.mathworks.com/matlabcentral/linkexchange). Using Matlab, these datasets were graphically reduced to three-dimensional representations where each point represents an individual cell (**Figure 4.2c**). In particular, PCA involves a mathematical transformation that groups a number of possibly correlated descriptors into a smaller set of uncorrelated "integrated descriptors" called principal components given the fact that some of the extracted subcellular descriptor metrics could be redundant. Using this methodology, the higher dimensional descriptor data set was reduced to three new dimensions, each representing a linear combination of a group of raw descriptors. The low dimensional features underwent classification using linear discriminant analysis (LDA), or support vector machine (SVM), with a randomized two-fold cross validation on individual data sets utilizing a radial distribution function (**Figure 4.2d**). Two parameters, sensitivity and specificity, were used to evaluate the performance of the classification. Sensitivity measures the proportion of actual positives that are correctly identified as such, while specificity measures the proportion of negatives that are correctly identified. The optimal classification/prediction can only be achieved when the sensitivity and specificity are both high, while low values of sensitivity and specificity indicate poor classification/discrimination between two datasets.

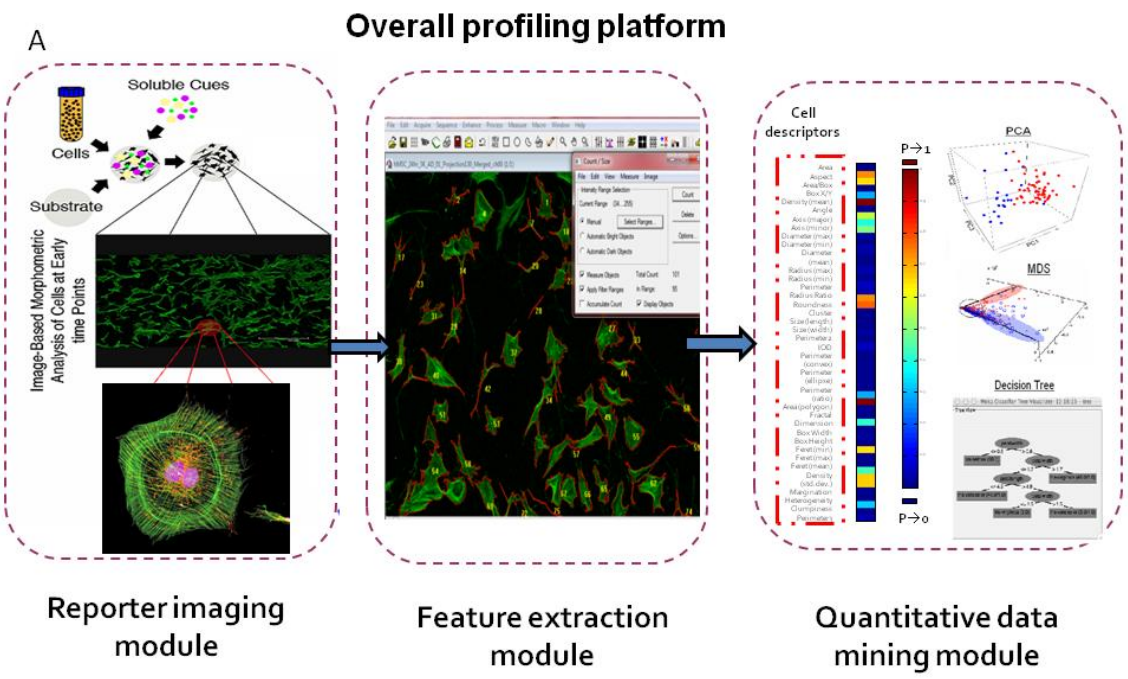
A
Overall profiling platform
Soluble Cues
Cells
Substrate
Image-Based Morphometric Analysis of Cells at Early time Points
Cell descriptors
P→1
P→0
PCA
MDS
Decision Tree
Reporter imaging module
Feature extraction module
Quantitative data mining module

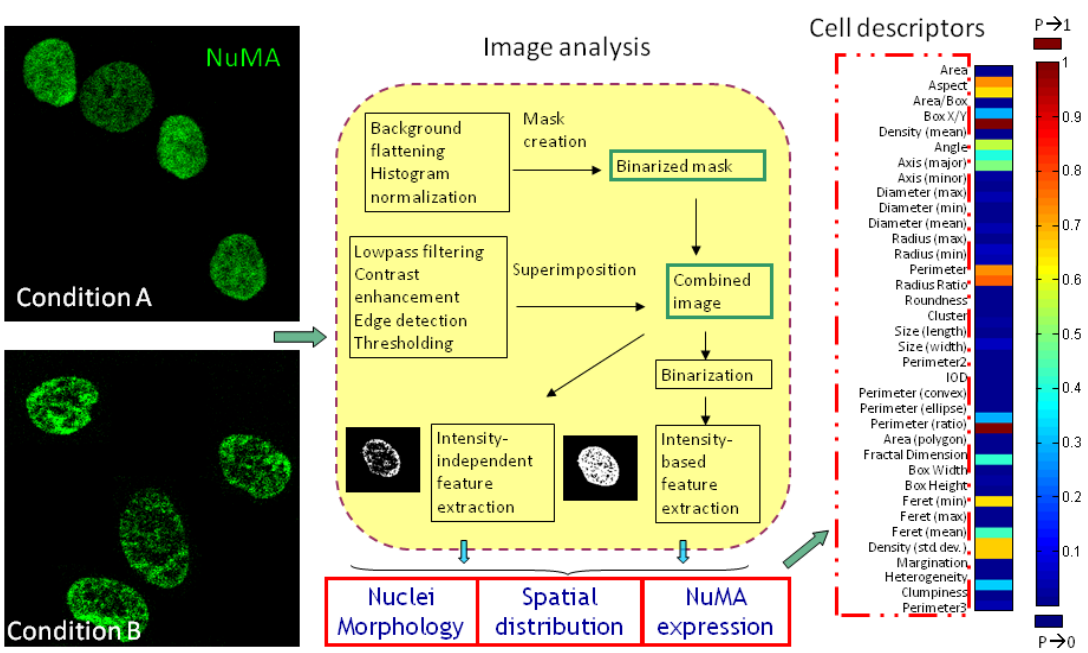
B
Image based subcellular feature extraction
NuMA
Condition A
Condition B
Image analysis
Background flattening Histogram normalization
Mask creation
Binarized mask
Lowpass filtering Contrast enhancement Edge detection Thresholding
Superimposition
Combined image
Binarization
Intensity-independent feature extraction
Intensity-based feature extraction
Nuclei Morphology
Spatial distribution
NuMA expression
Cell descriptors
P→1
P→0
Area
Aspect
Area/Box
Box X/Y
Density (mean)
Angle
Axis (major)
Axis (minor)
Diameter (max)
Diameter (min)
Diameter (mean)
Radius (max)
Radius (min)
Perimeter
Radius Ratio
Roundness
Cluster
Size (length)
Size (width)
Perimeter2
IOD
Perimeter (convex)
Perimeter (ellipse)
Perimeter (ratio)
Area (polygon)
Fractal Dimension
Box Width
Box Height
Feret (min)
Feret (max)
Feret (mean)
Density (std dev.)
Margination
Heterogeneity
Clumpiness
Perimeter3

C

Feature dimension reduction on cell descriptors

Cell descriptors

- Area
- Aspect
- Area/Box
- Box X/Y
- Density (mean)
- Angle
- Axis (major)
- Axis (minor)
- Diameter (max)
- Diameter (min)
- Diameter (mean)
- Radius (max)
- Radius (min)
- Perimeter
- Radius Ratio
- Roundness
- Cluster
- Size (length)
- Size (width)
- Perimeter2
- IOD
- Perimeter (convex)
- Perimeter (ellipse)
- Perimeter (ratio)
- Area (polygon)
- Fractal Dimension
- Box Width
- Box Height
- Feret (min)
- Feret (max)
- Feret (mean)
- Density (std.dev.)
- Margination
- Heterogeneity
- Clumpiness
- Perimeter3

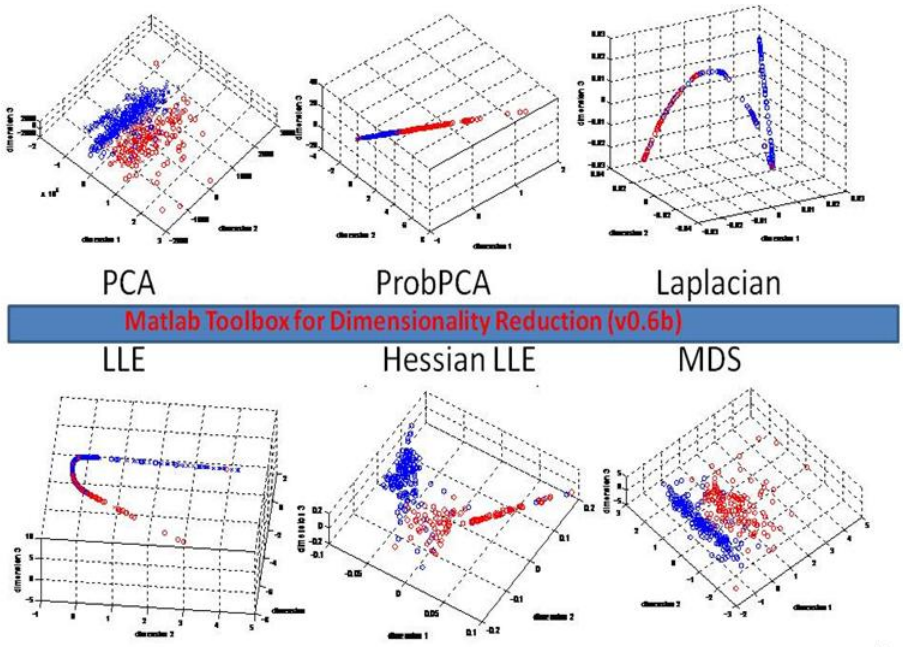

THREE NEW INTEGRATED DESCRIPTORS represent the raw dataset

D

Classification on subcellular features

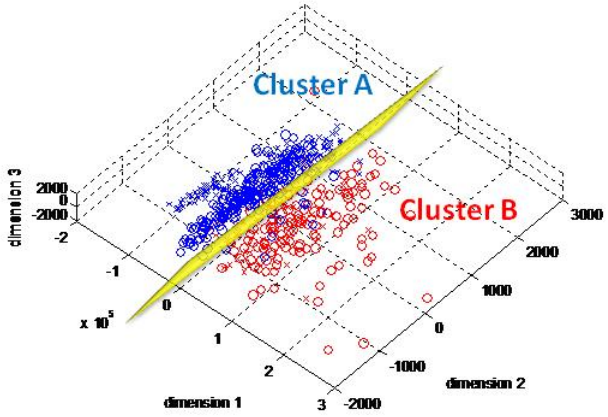

$$Sensitivity = 100\frac{True\ Positives}{True\ Positives + False\ Negatives} = 100\frac{True\ Positives}{Total\ Normal}$$

$$Specificity = 100\frac{True\ Negatives}{True\ Negatives + FalsePositives} = 100\frac{True\ Negatives}{Total\ Abnormal}$$

E

Cell descriptor data fusion

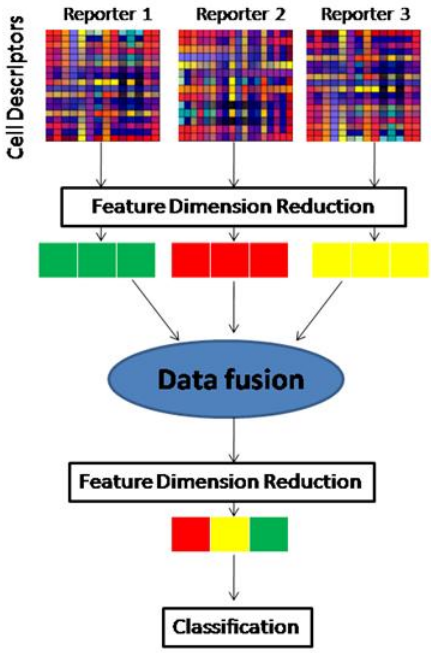

Figure 4.2: Schematic of High content Imaging Based Cell Profiling platform.

A) Overall profiling platform, including cell imaging module, subcellular feature extraction module, and data mining module. **B)** Subcellular feature extraction from high resolution images using image processing techniques; a pool of 50 cell descriptors was created and exported for further data mining. **C)** Subcellular feature dimension reduction using Matlab's toolbox. **D)** Further classification to identify the degree of separation of two clusters of cells based on dimensionally reduced subcellular features. Sensitivity and specificity were generated to report how different the two clusters of cells are from each other. For better visualization, a receiver operating characteristic curve was plotted based on sensitivity and specificity, where upper-left of the curve represented perfect separation of two clusters of cells and at the 45 degree slope line represented poor separation (random guess). **E)** A composite profiling approach using the concept of data fusion to combine cell descriptors from different reporters (e.g. cytoskeletal proteins, nuclear proteins). Raw cell descriptors from different reporters (actin and NuMA) first underwent feature dimension reduction to generate three representative super descriptors for each reporter (actin and NuMA) and were merged together to form six super descriptor pools and underwent further dimension reduction and final classification. All cell descriptors contributed to the final classification results but at different weights.

4.3 Results and Discussion

4.3.1 hMSC Differentiation versus Self-Renewal Cannot be Sensitively Captured Through Early Cytoskeletal Features or Lineage Specific Marker Expression

Human bone-marrow derived MSC demonstrate differentiation behaviors that are dependent upon both cell seeding density (optimally 3,000cells/cm^2 for OS and 20,000cells/cm^2 for AD) and growth factors. In this study, we cultured hMSC at an intermediate seeding density (10,000cells/cm^2) on fibronectin-treated glass and observed distinct differentiation fates after two weeks in AD, basal, and OS induction media. At 10,000 cells per cm^2 on fibronectin-coated glass in AD media, which is about half of the optimal seeding density for adipogenic differentiation, a small portion of hMSC also developed into osteogenic lineage(~15%) apart from adipocytic lineage (~40%) at 2 weeks as identified by fat marker Oil Red O and alkaline phosphatase marker Fast Blue Staining, respectively (**Figure. 4.3**). On the other hand, while cultured in OS media (**Figure. 4.3**), hMSC exhibited osteoblastic differentiation with greater than 80% of the cells displaying alkaline phosphatase activity and no detectable evidence of lipid accumulation. Finally, under basal control media (**Figure. 4.3**), the vast majority of cells were identifiable neither as osteoblastic nor adipocytic cells. Thus, under these conditions, hMSC demonstrated robust differentiation behaviors in response to altered soluble cues. However, screening for early lineage specific marker expression, or cytoskeleton features at 24 hours cannot distinguish lineage committed cells from naïve self-renewing cells, although it

somehow captures the difference between different lineages. (**Figure 4.1 and Figure 4.3**), as demonstrated by the classification results.

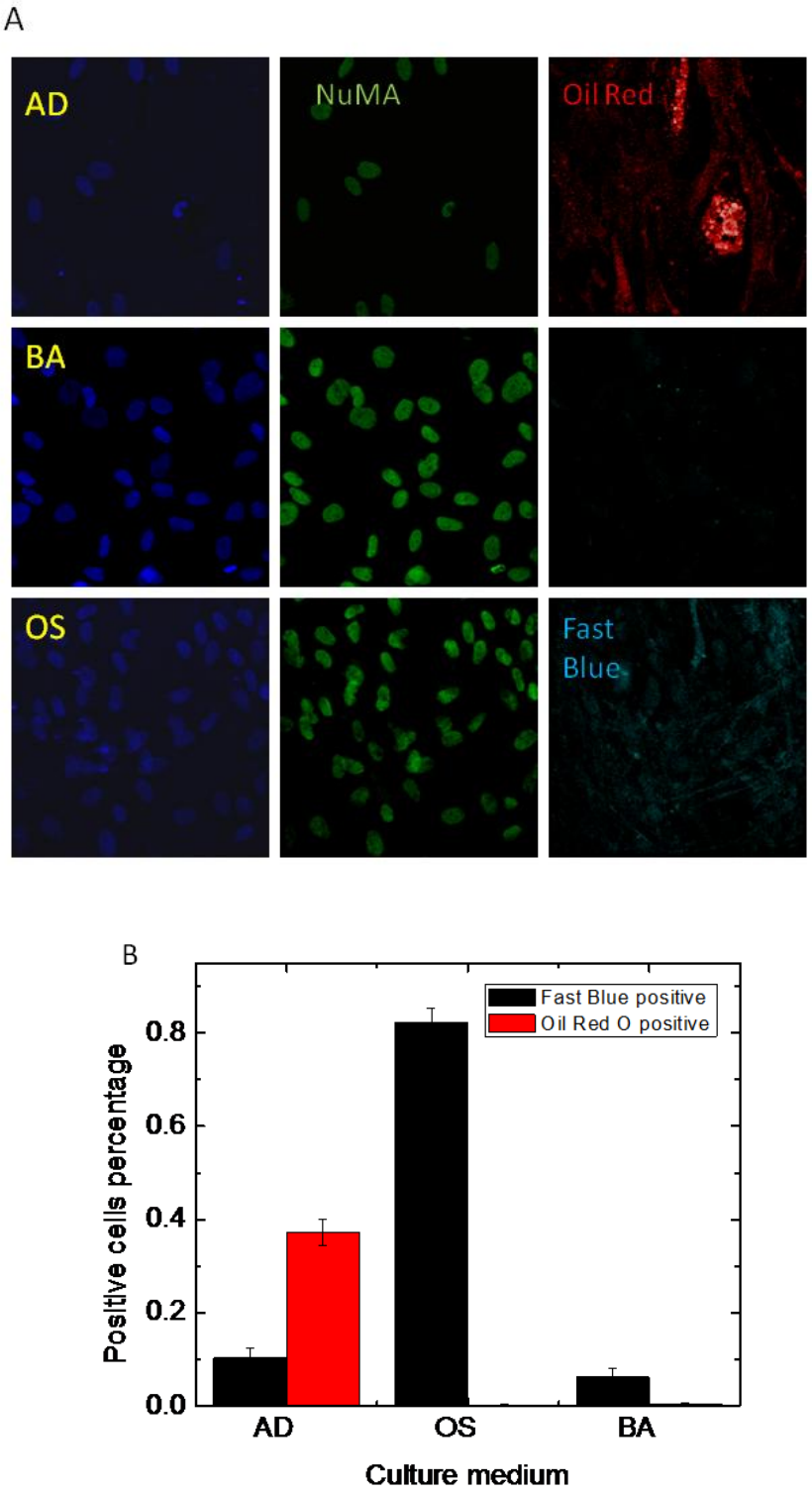

Figure 4.3: Evaluation of Mesenchymal Stem Cell Differentiation versus Self-renewal After 2-week Induction.

A) immunostaining of hMSC cultured under AD, OS induction medium and basal (BA) medium for 2 weeks. All cells were stained with Oil red O (adipogenic marker), Fast blue (osteogenic marker), NuMA proteins were labeled with antibodies and Alexa488 dye, and cell nuclei were counterstained with Hoechst. **B)** Quantification of Fast blue and Oil red O expression of cell populations in AD, OS, and BA culture conditions.

4.3.2 Human MSC Differentiation versus Self-Renewal Can be Captured Through Gene Expression Profiles and High Content Nuclear Features

Two key questions were addressed in this section: (1) which genes related to nuclear processes are differentially upregulated under distinct lineage inductive conditions (osteogenic versus adipogenic versus self-renewal)? To this end, we performed microarray analysis of human MSC seeded on glass substrates in osteogenic, adipogenic, and basal media at 24 hours. Using hierarchical clustering and Principal Component Analysis (PCA) we detected and visualized the variability in gene expression levels in MSC exposed to different soluble cues. (2) Do nuclear organization based high content imaging approach yield a more robust classification of stem cells, with the potential to forecast cells likely leading to distinct lineages?

4.3.2.1 Certain Genes Coding for Nuclear Proteins are turned on at 24-hours After Induction

Apart from the genes coding cytoskeletal proteins and downstream effectors, microarray analysis also showed different levels of gene expression that code for cell nuclear components, such as the family of nucleoporins, importin/transportin, lamin A/C, RAN and NuMA **(Figure 4.4a)**. Under osteogenic induction conditions, the family of nucleoporins (NUP37, NUP160, NUP98, NUP62CL, NUP43) were upregulated, together with a family of importins/transportins (KPNA3, KPNA1, KPNA4, KPNA5); compared to the corresponding downregulation under adipogenic induction and basal treatment. On the other hand, certain nucleoporin families (NUP205, NUP188, NUP93, NUP50, NUP153, NUP155, NUP88, NUP62, NUP214, NUP107, NUPL1, NUP35), importins/transportins (IPO8, KPNB1, IPO11) and RAN protein (RANBP5) were downregulated under adipogenic induction conditions compared with the osteogenic condition or non differentiation-inducing (basal) condition.

Large macromolecular structures, called nuclear pores, are transmembrane proteins that span the nuclear envelope that enable transport of molecules between the nucleus and cytoplasm[288,289]. Nucleoporins, a family of proteins that are part of the nuclear pore complexes, are the dominant constituents of the nuclear pore complex in eukaryotic cells. The nuclear pore complex can extend across the nuclear envelope to form a gateway regulating the exchange of macromolecules between the cell nucleus and the cytoplasm through the importin/exportin transport system. Macromolecules such as mRNA generated in

the nucleus are exported to the ribosome in the cytoplasm for protein synthesis, while proteins synthesized in the cytoplasm, such as histones, DNA and RNA polymerases, and transcription factors, are imported into the nucleus. The importin/exportin transport system provides the machinery involved in nucleocytoplasmic transport of cargo molecules larger than 40 kDa, while the RAN family of proteins actively plays a role in nuclear transport as well as nuclear assembly, cell-cycle regulation, and spindle assembly[290,291]. We found that under adipogenic induction, osteogenic induction, and basal conditions, different proteins from the nucleoporin and importin/exportin families were upregulated, which might indicate that pathways and regulation of molecular transport through the nuclear envelope vary with the onset of differential lineage commitment of MSC.

The lineage induction media may modify the chromatin structure that affects gene transcription in the cell nucleus. It has been proposed that the nuclear lamina contributes to heterochromatin formation that is associated with inhibition of transcription and gene silencing on the genomic level[136]. The nuclear lamina is composed of intermediate filaments and lamins A/C and B[292]. Nesprin, another nuclear protein that is located at the inner nuclear membrane can bind to lamin A/C and emerin, an inner nuclear envelope protein, via their spectrin-repeat rich KASH-domain[293,294]. However, gene expression levels of lamin A/C may not necessarily capture or reflect the spatial distribution that affects nuclear structure, which in turn affects regional control of gene expression associated with differentiation processes.

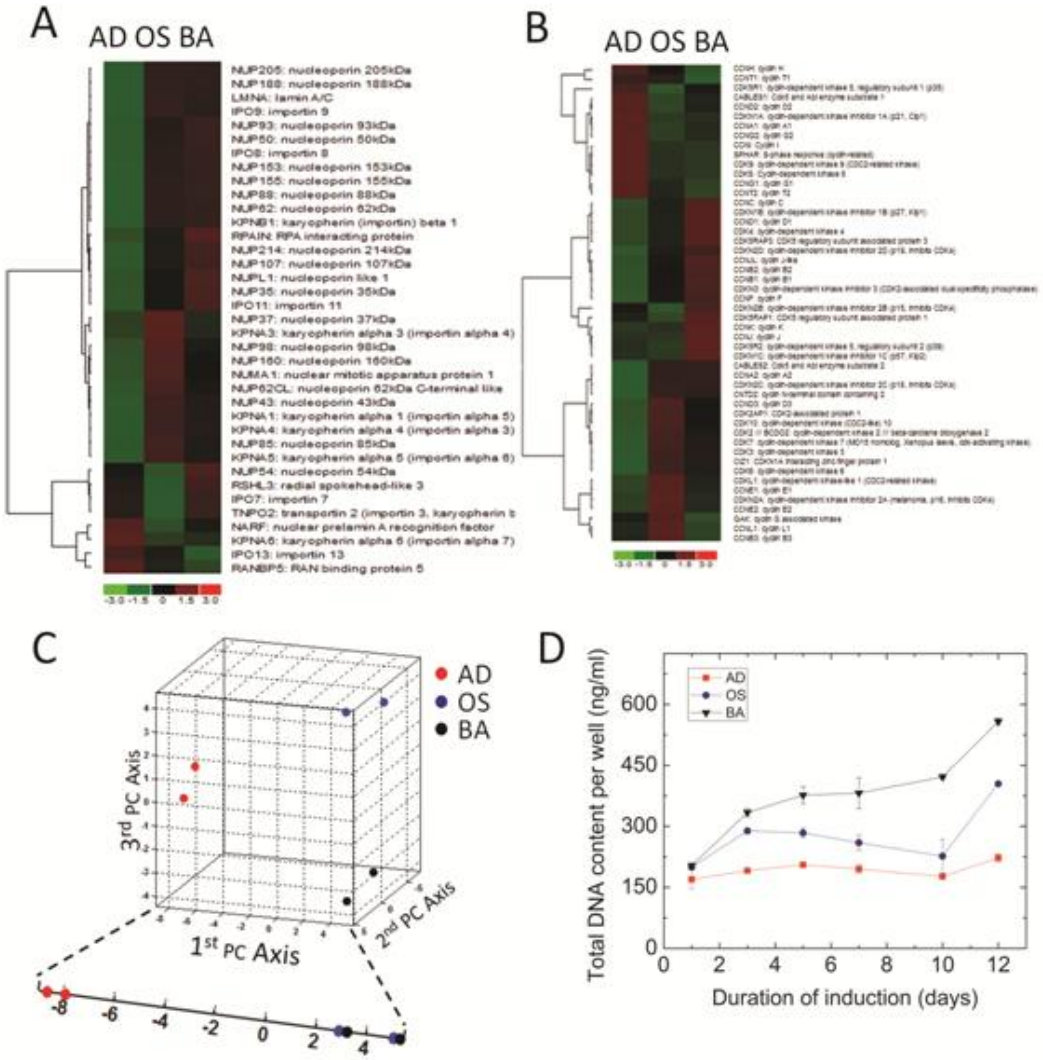

Figure 4.4: Structural and functional regulators of nuclear transport, organization and cell cycle show clear lineage-based variation in gene expression at 24 hours prior to the morphometric parsing in stem cells.

Hierarchical clustering analysis of genes involved in nuclear import and structural organization, reveals upregulation of nucleoporin messages under osteogenic (OS) and basal (BA) media treatment compared with adipogenic (AD) media treatment. Expression of lamin A/C and the nuclear mitotic apparatus, is upregulated (red) in OS and BA treated cells and downregulated (green) in cells

treated with AD media **(A**). Analysis of genes involved in cell cycle regulation, in particular the cyclins, cyclin-dependent kinases (Cdks), and cyclin-dependent kinase inhibitors, shows media-dependent levels of expression that indicates early differential regulation of cellular proliferation and cell cycle control in MSC under exposure to different extracellular soluble cues **(B)**. Dimensionality reduction of gene expression values shown in (**A**) and (**B**) using Principal Component Analysis (PCA) is shown in **(C).** Principal Component (PC) 1, 2, and 3, account for 42%, 17%, and 12% of the variability in the gene expression data, respectively. Notably, projection of the points in the 3-D PCA plot onto the first PC, shows largest variability in gene expression of nuclear transport/organization and cell cycle regulators between AD treated cells (red) and OS/BA treated cells (blue/black), while the intra-condition and OS/BA variability is relatively low. Gene expression of proteins involved in cell cycle control, nuclear import, and structural organization of the nucleus is thus less variable between OS and BA treatment than between AD and OS/BA treatment of MSC at 24 hours**.** **(D)** The growth curve of MSC under OS, AD induction and basal conditions. Cell growth was evaluated through the CyQUANT® Cell Proliferation Assay. The Y axis represents total DNA content per well (ng/ml), and the X axis represents the duration of induction. Cells are observed to grow fastest in BA media, while cells in OS media grow faster than AD media. The growth curve of cells in OS/AD/BA media aligns well with gene expression pattern of cell cycle-related cyclin family proteins.

Some organizational features of the cell nucleus are unique to undifferentiated cells, such as the concentration of heterochromatin at the nuclear periphery and the presence of transcription permissive areas around splicing factor speckles[165,295-297]. On the other hand, for differentiated cells, the most prominent organizational features are the concentrations of heterochromatin domains around a central nucleolus and at the nuclear periphery, as well as the formation of larger and fewer splicing factor speckles. Based on these observations, it has been proposed that the specific nuclear organization observed in differentiated cells might be important in stem cell determination, locking gene expression in place by maintaining genes in a silent state and enabling the expression of a small number of genes necessary for differentiation[136]. Therefore, the ability to quantitatively capture stem cell nuclear features during MSC differentiation could bridge the understanding of the contribution of nuclear organization to differentiation and help further delineate correlations between epigenetic control of gene expression and stem cell differentiation. Consequently, we sought to probe the nuclear structure and organization using an alternative approach—high content imaging of nuclear mitotic apparatus protein (NuMA) as a test case, since NuMA has been reported as a nuclear matrix protein, the expression and spatial organization of which changes as cells differentiate[131,165,295,298,299].

Moreover, we assessed the variability in expression of NuMA organization and cell cycle control genes between media conditions via principal component analysis **(Figure 4.4c)**. Points corresponding to media condition groups in the

3D principal component plot were projected onto the first principal component axis, which accounted for 42% of variability in the original gene data set. We found that the variability was greatest between AD and the two other treatments (OS and BA), represented by a larger separation of the points along the first PC axis. This finding is similar to the earlier observation with the expression of actin-associated proteins.

4.3.2.2 Lineage Induction Conditions Elicit Differential Proliferation Rates and Upregulation of Genes Related to Cell Cycle Control

It was observed that cyclin family proteins, which regulate cell cycle progress, were differentially upregulated/downregulated in MSC among the adipogenic, osteogenic, and basal conditions **(Figure 4.4b)**. There was a broad expression of most cyclin family proteins (major cyclins such as cyclin A-E and minor cyclins such as cyclin F-I) and cyclin dependent kinase (Cdk) enzymes to which they bind in MSC grown in non-inducing basal media. However, in adipogenically induced cells, the expression of a number of major cyclin proteins was downregulated, including that of cyclin B, cyclin C, cyclin D1&3, and cyclin E as well as Cdks. Similarly, it was observed that in osteogenically induced cells, only a few major cyclins were upregulated, namely cyclin A2, cyclin D3, cyclin E1&2, and cyclin B3.

To note, cyclin D/Cdk4, cyclin D/Cdk6, and cyclin E/Cdk2 complexes regulate the G1 to S phase transition, and cyclin B/Cdk1 regulates progression from the G2 to the M phase. Moreover, cell differentiation presumably happens after the checkpoint at G1 to S transition phase, where cells committed states of

continued growth, differentiation, or undergo apoptosis. Therefore, the formation of cyclin D/Cdk4, cyclin D/Cdk6, and cyclin E/Cdk2 complexes appear to be of significance during hMSC differentiation following induction with soluble cues. Interestingly, in adipogenic cells, most of the gene expression levels of proteins involved in cell cycle control was downregulated, which indicates the propensity of cells for inhibited cell growth and enhanced differentiation. Furthermore, for osteogenically treated cells, upregulation of cyclinA2, cyclin B3, cyclinD3, cyclinE1&2 was observed. However, upregulation of CDKN2B, which inhibits Cdk4 binding with cyclin D, was also noticed, which may suggest that one subpopulation of cells treated with OS media exhibited cell cycle progression while a second subpopulation committed to the differentiation pathway at 24 hours post-induction. For non-differentiating hMSC seeded in basal growth media, almost all members of the cyclin family and their associated Cdks were upregulated, indicating the expected proliferation of non-differentiating cells in normal growth media. In support of these findings, the growth curve of the hMSC seeded under adipogenic and osteogenic induction conditions showed growth trends reminiscent of the mRNA levels of cyclin/Cdk proteins determined from the microarrays, as demonstrated in **Figure 4.4d**, where hMSC grew faster in osteogenic induction media than in adipogenic induction media, but slower than in basal media.

4.3.3 Improved Classification of MSC Lineages at Early Time Points Using Nuclear Descriptors

Previously it was demonstrated by Treiser et al. that fibronectin pre-treatment could potentially speed up the lineage commitment forecasting as early as 24 hours[277]. Therefore, we sought to explore the potential of utilizing nuclear features to improve the lineage segregation. As described previously, a large pool of cell actin cytoskeletal descriptors and nuclear descriptors were extracted using image-based feature extraction algorithms[47,300]. For better visualization of the cell descriptor data sets, dimension reduction was performed on both the actin cytoskeletal descriptor pool and the nuclear descriptor pools using Principal Component Analysis (PCA). Interestingly, the 24 hour actin descriptors after PCA-LDA based data mining successfully segregated adipogenic lineage and osteogenic lineage committed cells, with a sensitivity of 93.30% and specificity of 91.51% (**Figure 4.5**). However, the cytoskeletal descriptor-based classification of adipogenic-lineage committed cells relative to undifferentiated cells was poor, with sensitivities of 45.83% (AD vs. BA) and 51.39% (OS vs. BA) (**Figure 4.5).**

Interestingly, when data dimension reduction and classification were applied to nuclear descriptors alone, lineage committed cells (either AD or OS) could be parsed out completely (100% sensitivity and 100% specificity) from undifferentiated cells (BA), while adipogenic and osteogenic lineages could also be parsed out from each other with sensitivity and specificity of 85.54% and 95.18%, respectively (**Figure 4.5**). By examining the principal components from the dimensionality reduction, we found that all three categories of descriptors

(morphology descriptors, NuMA expression descriptors, and spatial distribution descriptors), contributed to the final data interpretation. This sheds light on the limitation of gene microarray data to parse out MSC exposed to adipogenic, osteogenic, and basal conditions.

Another interesting observation was that differences between MSC cultured in adipogenic, osteogenic, and basal media correlated with variations in cell growth (**Figure 4.4d**), which is also demonstrated through the gene expression of cyclin family proteins and NuMA descriptor- based profiling. NuMA is an abundant 240 kDa protein that is present in the nucleus of interphase cells and concentrates in the polar regions of the spindle apparatus during mitosis[17,298,299]. As a mitotic-associated protein, NuMA is more closely related to cell cycle progression and thus NuMA organization could be conceivably linked to differential growth kinetics. However, NuMA also functions as a structural protein interface between the nucleoskeleton and RNA splicing. The structure and organization of NuMA have been reported to be distinctly modulated between non-differentiating cells and differentiated cells[131,165]. Therefore, whether NuMA based segmentation is solely a consequence of varying cell growth, differentiation, or a combination of both, remains to be further investigated.

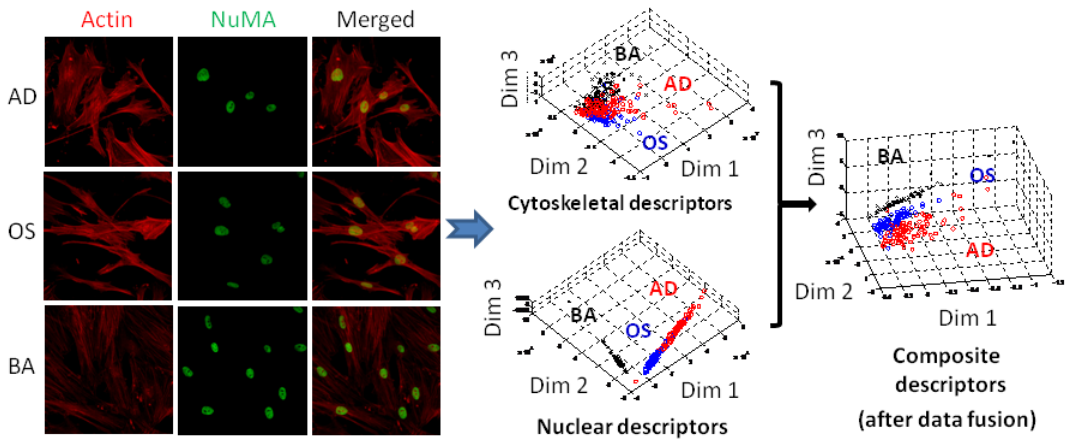

	Actin Descriptors			Nuclear Descriptors			Composite Nuclear and Actin Descriptors		
Lineage Comparisons →	AD vs OS	AD vs BA	OS vs BA	AD vs OS	AD vs BA	OS vs BA	AD vs OS	AD vs BA	OS vs BA
Sensitivity (%)	93	46	53	86	100	100	97	96	99
Specificity (%)	92	89	90	95	100	100	98	99	93
MSE	0.1	0.2	0.2	0.10	0.01	0.01	0.03	0.06	0.02

Figure 4.5: A composite profiling approach using both cytoskeleton and nuclear features enhanced the classification of adipogenic, osteogenic and non-differentiated cells.

Left panel: Visualization of subcellular component. Actin cytoskeleton was stained with phalloidin Texas Red (Red in the image), cell nuclear mitotic protein (NuMA) was stained with Alexa 488 through immunocytochemistry (Green in the image). All subcellular components were visualized through Leica SP2 confocal/multiphoton imaging system under a 63x immersion objective (NA=1.3). **Middle panel**: Visualization and classification of actin cytoskeletal descriptors and nuclear descriptors, respectively. Human MSC from bone marrow were cultured on fibronectin-coated coverglass for 24 hours in OS/AD/BA media, respectively. Actin cytoskeleton features and nuclear features were extracted separately according to the image analysis procedures described in our

previous publications. Principal component analysis was performed on each descriptor dataset to reduce the dimensionality to three new dimensions that are combinations of descriptors from the original descriptor pool. Following that was the classification steps. **Right panel:** Composite descriptors after data fusion. A smaller composite descriptor pool was formed by combining the dimensionally reduced cytoskeletal descriptors and nuclear descriptors; new dimension reduction was performed on the composite descriptor pool and visualized in another three new dimensions and was subject to LDA classification.

Overall, the combination of the composite descriptor data sets showed that the cell cytoskeletal descriptors and nuclear descriptors collectively improve lineage commitment classification, with cytoskeletal descriptors parsing adipogenic over osteogenic lineage while nuclear descriptors parsed out lineage committed cells over non-differentiating cells. These insights suggest that the combination of both cytoskeletal and nuclear descriptors can more robustly distinguish amongst adipogenic, osteogenic, and non-differentiating cells. To this end, we proposed a data fusion approach that combines data from multiple sources to improve efficiency, robustness, and accuracy for subsequent classification (**Figure 4.2e**). This technique was originally utilized in geospatial applications with the expectation that fused data is more informative than the original separate inputs. With the use of data fusion, high dimensional cytoskeletal and nuclear descriptor data sets were first reduced to three new dimensions, combined together to produce a new data set of six dimensions, further reduced to three new dimensions of descriptors comprising of linear

combinations of both cytoskeletal and nuclear descriptors, and finally subjected to classification algorithms. Classification results after fusion of cytoskeletal and nuclear descriptors showed improvement in the parsing of adipogenic and osteogenic lineages (with sensitivity and specificity of 97.22% and 98.18% respectively), as well as separation of lineage committed cells (either adipogenic or osteogenic) over basal-treated cells (**Figure 4.5**). Thus, we demonstrated that the data fusion technique can improve the classification of cells in the adipogenic, osteogenic, and uncommitted states.

4.4 Conclusion

Previous high content imaging of single cell cytoskeletal features identified osteogenic versus adipogenic lineage signatures of human mesenchymal stem cells much earlier than traditional endpoint assays of differentiation. However, it failed to identify self-renewal versus lineage-committed phenotypes. In this study, we used gene expression profiling via microarray analysis to search for nuclear clues of lineage-specific cell phenotypes. Our studies on 24-hour gene expression after induction demonstrate that among differentiation-specific genes are certain genes coding for nuclear proteins and cell cycle related proteins. The role of nuclear structure was further explored in terms of high content imaging of nuclear structural proteins. We propose a novel high content imaging based composite profiling approach, as a continuation of the high content profiling work published previously, to capture the early stem cell differentiation on a single cell basis. This methodology extracts morphological features, spatial distribution,

and expression of key cytoskeletal proteins (e.g. actin) and nuclear proteins (e.g., NuMA) to parse out osteogenic, adipogenic, and undifferentiated states of MSC within the first 24 hours. By virtue of discerning different lineage pathways, this “integrative” approach is more comprehensively linked to both cell cycle/nuclear and cytoskeletal substrate signaling and provides more robust forecasting than exclusive cytoskeleton-based profiling.

5 Mapping Cell Phenotypes Using High Content Nuclear Imaging based Profiling Approach

5.1 Introduction

Stem cells have the potential to serve as a source of cells for therapeutics to treat several degenerative diseases, but their ability of self-renewal, in other words plasticity, also makes them susceptible to cancerous transformation. This brings along with stem cell-based therapy a possible risk of tumor formation. The risk for malignant transformation exists for each stage of the clinical lifecycle of stem cells, including malignant transformation in vitro during production phases, during insertion of potentially therapeutic transgenes, and finally *in vivo* via interactions with tumor stroma and oncogenic microenvironments. Current methods employed in clinical trials have limitations such as the absence of long term follow-up and lack of adequate screening methods to detect transformation early on. Therefore, to better harness the potential of stem cells for regenerative medicine, one needs not only in-depth stem cell biology but also screening tools to probe and monitor stem cell behaviors: self-renewal, differentiation, and transformation.

Different states of stem cells, e.g. self-renewal, cancerous transformation, and lineage commitment can usually be visualized using conventional microscopy. Differences in expression readouts or sub-cellular localization of biomolecular markers often reveal phenotypic differences amongst a population of cells. However, these differences may not be observable until later stages of

the developmental process (ranging from weeks to months). Thus, there is a need for an early identity or “signature” that reflects the “preprogrammed” stem cell state. Conventional efforts to tackle this problem have been focused on early gene expression profiles. Previous studies have demonstrated that upon stem cell state changes, phenotypic genes do not turn on at early stages of lineage commitment or upon the onset of transformation; on the contrary, a number of other genes, including cell and tissue structure dynamics, cell cycle and apoptosis, intracellular communication, metabolism and regulation of gene expression, are transcriptionally altered[143,144,301].

Taken together, these previous studies suggest that seemingly indistinguishable cells at an early stage may undergo further state changes, as indicated by non-lineage specific phenotypic gene expression profiles. Since the cell nucleus is the location where gene expression control takes place, the study of the inner organization of cell nucleus could be an avenue to expand the understanding of changes of a cell’s state. The nuclear matrix, a major component of cell nucleus, provides a three dimensional framework for the tissue specific regulation of genes by directed interaction with transcriptional activators. It binds diverse nuclear matrix proteins and supports their assembly into functional macromolecular complexes involved in important nuclear processes, such as DNA replication, transcription, and RNA processing. The nuclear matrix is the first link from the DNA to the entire tissue matrix system and provides a direct structural linkage to the cytomatrix and extracellular matrix[302]. In summary, the tissue matrix serves as a dynamic structural framework for the cell, which in

turn interacts to organize and process spatial and temporal information to coordinate cellular functions and gene expression. Apart from nuclear matrix, certain compartments of the cell nucleus, including nucleoli, the higher organization of chromatin into heterochromatin and euchromatin regions, as well as non-chromatin domains have been identified to be important in changes of stem cell state[156,158-164]. Therefore, we hypothesize that distinct early gene expression profiles in cells might translate into characteristic nuclear structural and organizational changes that might be too minute to be discerned using conventional microscopy and intensity-based low content analysis, but may be detected by high resolution microscopy and *in silico* data processing and modeling techniques to extract high content information.

Here we propose a high content imaging-based profiling platform for the early identification of nuclear signature profiles indicative of long-term stem cell state changes based on confocal microscopy. We started by hypothesizing that state changes of cells can be readily identified through the use of an initial biomolecular marker set. To capture the early changes of cell state, our strategy was to (1) use one of the most abundant nuclear matrix proteins, nuclear mitotic apparatus (NuMA) as a biologically-relevant reporter; (2) perform confocal/multiphoton microscopy to acquire high resolution images; (3) perform image-based high content nuclear feature extraction to harvest an array of nuclear descriptors that can be divided into three categories: nuclear matrix protein expression (intensity based features), nuclear shape (morphological features) and nuclear organizational/spatial distribution features (texture

features); (4) utilize dimension reduction and classification techniques to identify differential states of stem cells. This platform enables identification of early subcellular “signatures” of cells that precedes state change. It also provides an alternative strategy for obtaining phenotypic and functional characterization of identifying cell state without using additional biomolecular markers at later time points. The utility of this platform was demonstrated in capturing mesenchymal stem cell transformation on various extracellular substrates.

5.2 Materials and Methods:

5.2.1 Cell Culture

Human mesenchymal stem cells (hMSC) were obtained from commercial sources (Lonza; Walkersville, MD). Cells were cultured in a humidity-controlled environment under 5% CO_2 and 37°C and fed every 3-4 days with growth media (basal media) supplemented with commercial SingleQuot’s© (Catalog # PT-3001, Lonza). Cells were received at passage 1 and used from passage 13-19. Cells were sub-cultured upon reaching 90% confluence. The in vitro oncogenic transformation process was performed through periodic treatment of a known metal carcinogen, nickel sulfate (Sigma) according to the following protocol: Cells seeded in 24-well plates were allowed to attach for 24 hours in basal conditions. After 24 hours, wells were washed with DPBS and treated with nickel (II) sulfate (36-72 μM in basal media) for 48 hours. The samples were then washed and supplemented with basal media for 48 hours, followed by nickel (II) sulfate treatment for 72 hours, and ended with 72 hours in basal medium. This

brings the total to an 11-day transformation. In addition to nickel sulfate-treated hMSC, we also studied genetically-transformed hMSC, which were acquired from Dr. Richard Gorlick's lab (The Children's Hospital at Montefiore, Bronx, NY). These hMSC were sequentially transformed with a retrovirus containing human telomerase reverse transcriptase (hTERT), simian vcuolating virus 40 large T antigen (SV40 TAg), and lentivirus containing oncogenic H-Ras[303].

5.2.2 Cellular Assays

5.2.2.1 Characterization of hMSC Oncogenic Transformation

Fluorescent in-situ hybridization (FISH)

Fluorescent in-situ hybridization was used to detect and localize for the presence of telomerase within the MSC population of transformed cells. A cadmium selenium (CdSe), a gift from of Dr. Matthew Becker (University of Akron, OH), conjugated probe (5'-$NH_2(CH_2)_{12}$ -T*C*T*C*AGTTAGGG*T*T*A*G) was designed to be complimentary to a human telomerase unit (hTR), an mRNA transcript, and a portion of the holo-enzyme. This quantum dot conjugated probe has an emission peak at 594nm, which can be easily detected using confocal microscopy. After washing with PBS, cells were fixed using 4% paraformaldehyde at room temperature for 15 minutes. Cells underwent a dehydration process by washing with 70%, 90%, and 100% ethanol successively for 4 minutes. They were then washed with 100% xylene for 5 minutes before rehydration with 100%, 90%, and 70% ethanol successively for 4 minutes. Cell samples were washed with PBS and then treated with Pepsin (100 µg/mL

PEPSIN in 10 mM HCl) for 10 minutes at 37°C. After another 5-minute PBS wash and a 10-minute post fixation with 1% paraformaldehyde, cell samples were treated with 50 µL of hybridization solution and 10 µL of the CdSe quantum dot solution for 16 hours at 37°C. Cells were then washed with solution (60% formamide, 300 mM NaCl and 30 nM sodium citrate) three times for 10 minutes. More washes with the same solution were applied in 37°C for 10 minutes followed by a last wash with PBS.

Telomerase expression was acquired as mean fluorescence intensity per cell through image analysis. Telomerase fold-change was further quantified as the ratio of telomerase expression on carcinogen-treated hMSC over normal hMSC on the same substrate condition. Oncogenic transformation was quantified using a scalar, “transformation index”, which normalized the fold change of telomerase expression of hMSC under carcinogen treatment to that of genetically transformed hMSC (0—no transformation, 1—fully transformed).

Immunocytochemistry (ICC)

Staining for a proliferation marker (Topoisomerase α-II) and nuclear mitotic apparatus (NuMA) were completed on MSC fixed on well plates with 4% paraformaldehyde. Prior to the addition of the primary antibodies, cells were permeabilized using a buffer of 0.1% Triton X-100 in PBS for 30 minutes. Mouse anti-human primary antibodies were used at a 1:50 dilution in 5% goat serum in PBS for non-specific binding. An amount of 75-100 µL of antibody solutions were added to each well for 16 hours in 4°C on rocker. After primary antibody removal cell samples were washed with washing buffer (0.1 % Tween-20, 0.01% Triton X-

100 in 1x DPBS) three times for 5 minutes. AlexaFluor488 goat anti-mouse secondary antibody was applied to samples at a dilution of 1:200 for 1 hour at room temperature on rocker. Cell samples were then washed three times for 5 minutes. Cell nuclei were counterstained with Hoechst 33342 dye (1:1000 dilution) in PBS for 10 minutes at room temperature on rocker. Samples were washed with PBS, immersed in fluoroguard anti-fade reagent and stored at 4°C before being imaged on a Leica Multiphoton/Confocal Microscopy.

Flow Cytometry

Non-confluent cultures were trypsinized into single cell suspensions, counted, washed with phosphate-buffered saline (PBS), and stained with antibodies specific for human cell surface markers: CD44-FITC, Stro-1-PE, and CD133-APC (eBioscience Inc. San Diego, CA). A total of 100,000 cells were incubated with antibodies for 15 minutes at room temperature. Unbound antibodies were washed off and cells were analyzed no longer than 1 hour post-staining on a BD Facscalibur^{TM} flow cytometer system (Billerica, MA).

5.2.3 Microscopy, High Content Profiling and Computational Modeling

High resolution confocal/multiphoton microscopy, image based nuclear feature extraction, and dimensionality reduction (**Figure 5.1a**) were employed as described in the methods section of Chapter 4. Dimensionally-reduced nuclear features were classified using SVM, as described previously. For validation purposes, two datasets with known divergent outcomes (negative and positive controls identified through conventional assays) were compared, and SVM

classifier performed on the two sets of dimension reduced cell nuclear descriptors were expected to have no overlap in the two distributions (100% for both sensitivity and specificity). The sensitivity and specificity can further be incorporated into a receiver operating characteristic (ROC) curve for better visualization of the classification results, where sensitivity was plotted against 1-specificity. In the curve, the upper left corner represents a perfect separation between two data sets, and the middle 45 degree region passing the origin represents a random guess region, indicating inseparable datasets. The area under the ROC curve (Az), defined as a measurement of area within the upper left quadrant (above the random guess line), is a parameter that measures discrimination (the ability of the test to correctly classify those with and without the disease in clinical diagnostics, specifically in this study, hMSC transformation). The closer the ROC curve is to the upper left corner, the higher the Az value, thus the higher the overall accuracy of the test. The popular criteria for determining the accuracy of a diagnostic test is similar to traditional academic point systems: an Az value of 0.9 to 1 is indicative of excellent discrimination, 0.8 to 0.9 is good discrimination, 0.7 to 0.8 is fair discrimination, 0.6 to 0.7 is poor discrimination and an Az value of 0.6 and below is indicative of no discrimination (failure).

In order to determine the degree of transformation of a given condition, e.g. hMSC exposed to short term (72h) carcinogen induction, nuclear descriptors were generated and compared with genetically transformed hMSC (positive control) and normal hMSC (negative control) respectively in the SVM classifier

(shown in **Figure 5.1b**). Therefore, two Az values were acquired from the classifier, with Az1 representing the comparison between the test set and negative controls (normal hMSC), and Az2 representing the comparison between the test set and positive controls (oncogenetically-transformed hMSC). Equation 5-1, which combines the two Az values: $iAz = \frac{(Az_1 + 1 - Az_2)}{2}$ (Equation 5-1), can then be used to calculate an integrated Az (iAz) value. This value determines the location of the test set, which is between 0 (the negative controls) and 1 (positive control). For our application of stem cell transformation, iAz could be used to mirror the degree of transformation (transformation index).

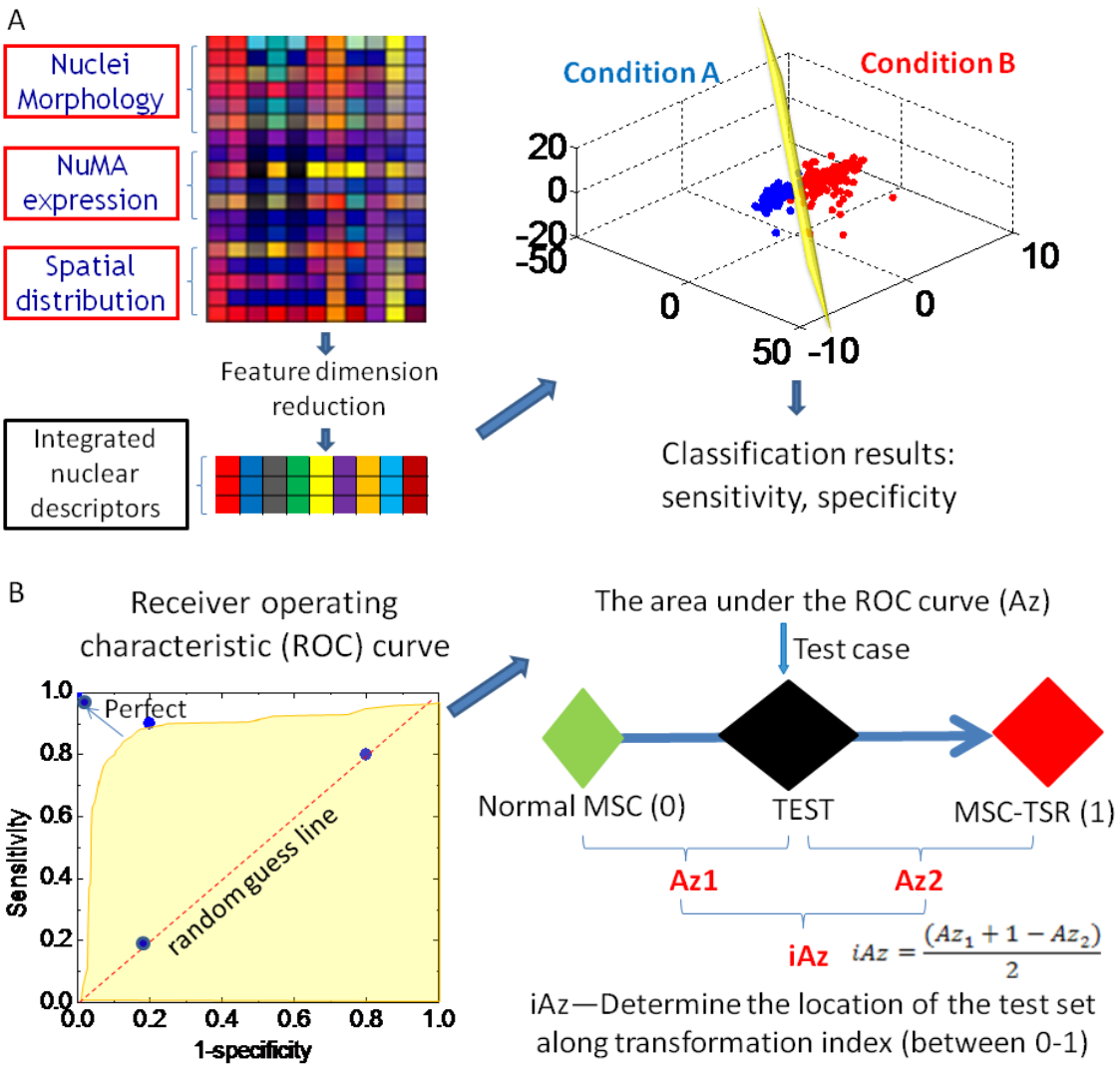

Figure 5.1: Schematic of data mining on high content nuclear descriptors.

A) Schematic of cell nuclear descriptors dimension reduction and classification. **Left panel**: a pool of nuclear descriptors was extracted from image analysis. PCA analysis was used to reduce the dimensionality of the nuclear feature space into three 'integrated' nuclear descriptors (visualized in the **Right panel)**, each axis representing a combination of nuclear descriptors. A SVM-based

classification technique was used to discriminate the dimensionally reduced nuclear descriptor datasets from two different conditions. SVM classification was verified by assessing sensitivity and specificity. **B)** Utilization of the classification results used to determine the location of the test set in-between the negative and positive controls. **Left panel**: Visualization of classification results using a receiver operating characteristic (ROC) curve. In the ROC plot, sensitivity is plotted against 1-specificity. The upper left corner in the ROC curve represents a perfect separation between two data sets, and the middle 45 degree region passing the origin represents random guess region, indicating inseparable datasets. Measuring the area within the upper left quadrant (above the random guess line), named the area under the ROC curve (Az), can be used to evaluate the discrimination between the two datasets. **Right panel**: An example showing the utility of Az to estimate the location of a test set in the negative (normal MSC) and positive controls (genetically transformed MSC). Comparison was first made between the test set and negative controls, followed by a comparison between the test set and positive controls. An integrated Az (iAz) was further calculated via combining the two Az values from the previous two comparisons. The iAz value, ranging from 0-1, is indicative of the location of the test set in the unit index defined by negative (0) and positive (1) controls.

5.2.4 hMSC Transformation Study on Polymeric Substrates

Tyrosine-derived polycarbonates[225] (**Figure 5.5a**), polymethacrylates (Courtesey of Dr. Abraham Joy from NJCBM), and poly(L-lactic acid) (Resomer

L-206) (Boehringer Ingelheim; Ridgefield, CT) were dissolved in 1.5% (v/v) methanol in methylene chloride solutions yielding a 1% (w/v) polymer solution. Polymer solutions were then spin-coated onto 15 mm glass coverslips. Spin-coating was conducted at 4,000 RPM for 30 seconds.

Polymer-coated glass coverslips were placed in the bottom of a 24 well glass-bottom tissue culture plate and secured with a silicon O-ring (Catolog # - 111, Molding Solution; Lexington, KY). The plate was sterilized with a UV light applied at 5,500 to 6,500 μW per cm^2 for 900 seconds. Human MSC were seeded at 20,000 cells per cm^2 and underwent an 11 day carcinogen induced transformation process (described in the methods section). At 72 hours, cells were fixed and stained with NuMA for imaging. After the 11 day transformation treatment, cells were fixed and subjected to functional assay screening as described earlier in this section.

5.2.5 Statistical Analysis

Statistical analysis was performed on morphometric parameters using SPSS software and included analysis of variance (ANOVA) with Tukey's HSD post hoc method and other multivariate statistical tools. The differences were considered significant for $p < 0.05$ unless otherwise noted. Error bars indicate the standard uncertainty around the mean.

5.3 Results

5.3.1 Overview of the high content nuclear profiling platform

Our methodology is composed of three steps. In the first step, we identified a collection of cell populations from high-resolution confocal images of cells stained with a set of initial functional markers or via functional assays. Semi-automated analysis is then used to characterize the cells stained with initial marker and returns readouts that can be used to distinguish multiple cell phenotypes within a single cell population, through the choice of initial markers varies for different studies. In the second step, we sought to determine whether the distinctions identified in the first step can also be captured utilizing the high content nuclear features at end time points. Therefore, a SVM-based classifier was used to distinguish the known distinct cell populations using the high content nuclear features, thus “training” the classifier. In the third step, we performed new experiments on different cell types/sources or culture conditions at time points earlier than the first step. We then used the high content nuclear features obtained from these experiments as a test set for the trained classifier, and used the classifier to try to distinguish cell fates under these unknown experimental conditions. Thereby, this approach provides a way of early identifying cells with different behaviors and mapping potential cellular responses to variant stimuli without using complex molecular/functional marker sets.

5.3.2 Predicting Oncogenic Transformation of Stem Cells

5.3.2.1 Oncogenically Transformed hMSC have Distinct Molecular and Nuclear Signatures from Normal hMSC

We first applied our approach to identify normal hMSC and genetically transformed hMSC as training sets. Since the genetically transformed hMSC were well characterized by Liu et al. and his colleagues[303], we selected telomerase as the initial molecular marker for the transformed phenotypes in this study. Shown in **Figure 5.2a**, the telomerase mRNA expression in genetically transformed hMSC was three times higher than normal hMSC. In parallel, high resolution images from the nuclear protein, NuMA, labeled with Alexa488 (green) and nuclei, labeled with Hoechst 33342 (blue) were acquired for genetically transformed hMSC and normal hMSC (**Figure 5.2b left panel**). These images demonstrated that there were indeed minute visual differences in the cell nuclear morphology and NuMA organization within 72 hours, however, they were difficult to quantify without the use of computer based image analysis, where individual cell nuclear morphology, NuMA protein expression, texture and spatial distribution descriptors were obtained via a series of image processing techniques that captured quantitative differences in cell nuclear organization (**Figure 5.2b middle panel**). Further feature dimension reduction and classification analysis results confirmed the distinction between these two cell types (**Figure 5.2b right panel**), with 100% sensitivity and specificity, respectively.

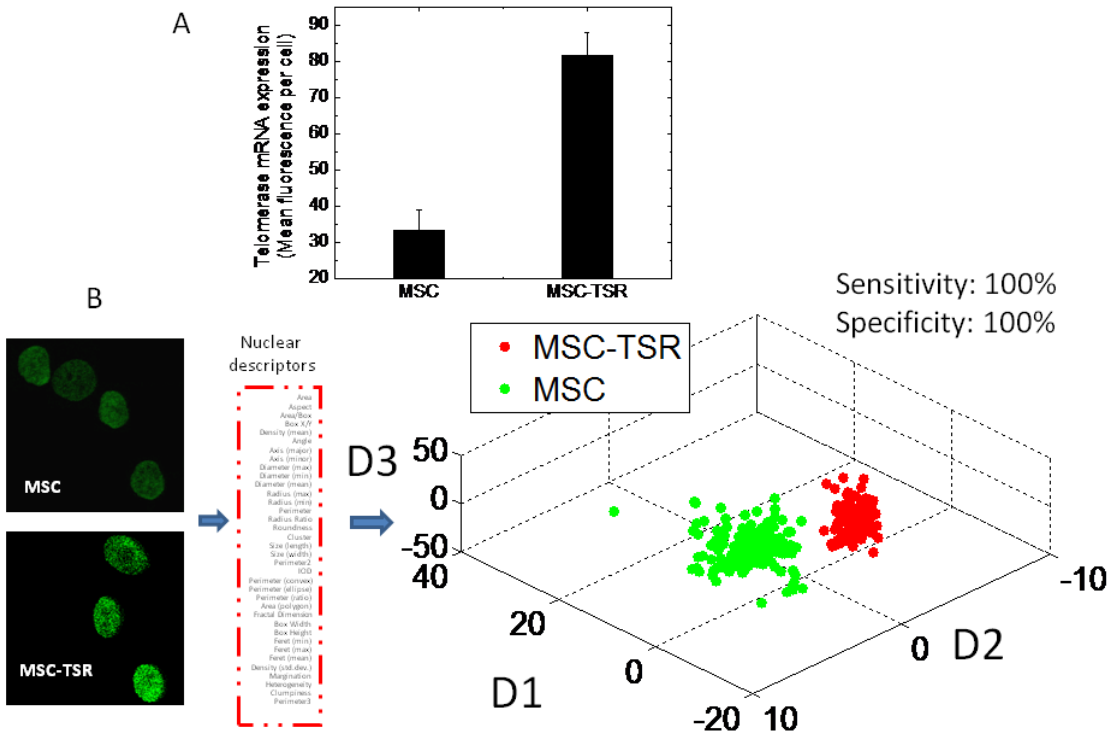

Figure 5.2: Characterization of genetically transformed hMSC using high content nuclear descriptors.

A) Telomerase (a cancer marker) expression screening was performed on genetically transformed hMSC (MSC-TSR) and normal hMSC. Quantitative telomerase mRNA expression was acquired from image analysis performed on genetically transformed hMSC (MSC-TSR) cells and normal hMSC labeled with a quantum dot-conjugated Telomerase mRNA probe via Fluorescent In-Situ Hybrydization (FISH). **B)** High content nuclear descriptor based profiling on genetically transformed hMSC and normal hMSC. **Left panel**: High resolution (63x, confocal average projection) images of NuMA proteins from genetically transformed hMSC (MSC-TSR); **Middle panel**: A pool of nuclear descriptors were extracted from NuMA images; **Right panel** and table: Three dimension plot of 'integrated' super nuclear descriptors, where each axis represents a

combination of nuclear descriptors. A SVM-based classifier was applied to the dimension reduced nuclear descriptors and returned 100% sensitivity and specificity, demonstrating the distinctive nuclear features of transformed hMSC and normal hMSC.

5.3.2.2 hMSC Transformation Can Also be Observed after Periodical Carcinogen Treatment

In this section, we performed an alternative experiment on hMSC transformation, but utilizing carcinogen induced transformation as an alternative approach. hMSC were exposed to periodical carcinogen, nickel sulfate, containing basal medium for 11 days. The effect of nickel sulfate induced cell carcinogeneisis was reported and well characterized by Shobha et.al[304]. In this study, abnormal transformation was confirmed using assays for cell proliferation, cell growth, topoisomerase-II α protein expression, and telomerase mRNA expression. **Figure 5.3a** left panel showed raw images of cells that were used to quantify cell growth by staining nuclei with Hoechst and performing automated counting using ImagePro Plus at 72 hours post-attachment. Expression of the proliferation marker topoisomerase-II α, represented by mean fluorescence intensity per cell, was enhanced by two-fold on carcinogen-treated hMSC when compared to the basal control (**Figure 5.3a middle panel**). Both cell number and proliferation marker expression confirmed that carcinogen treated cells underwent replication at a much higher rate than those in basal conditions. To further establish the transformation process at molecular level, we quantified the expression of telomerase, which is over-expressed in more than 95% of all

cancer types in literature[305-308]. The telomerase mRNA expression in carcinogen treated hMSC was two-fold higher than that of basal cells (**Figure 5.3a right panel**). This further confirmed the transformation process of hMSC under periodical nickel sulfate treatment. Certain cancer stem cell markers were also investigated, including CD44, CD133 and Stro-1, all of which showed increased expression on carcinogen treated hMSC (**Figure 5.3b**).

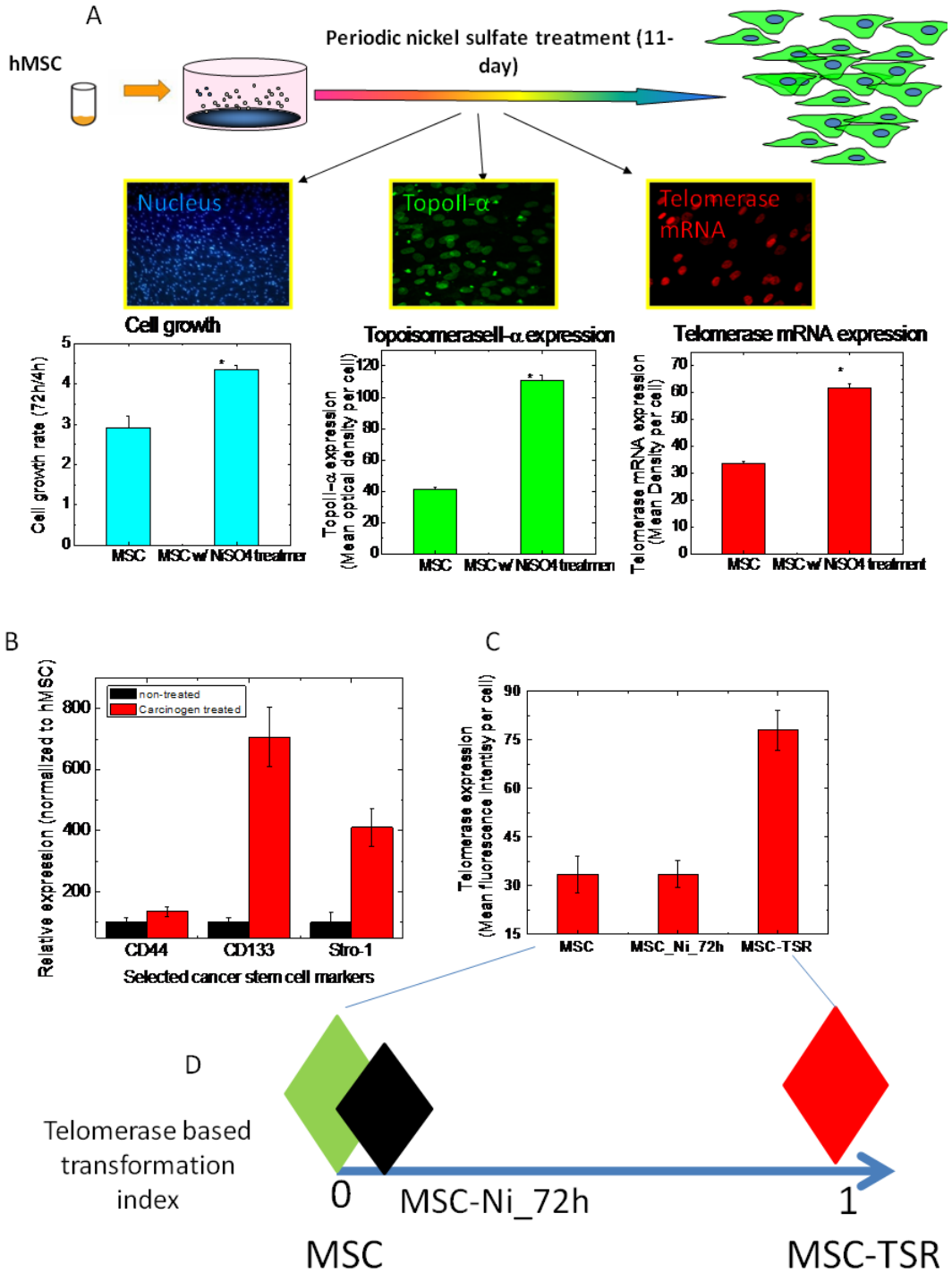

Figure 5.3: Characterization of carcinogen-induced hMSC transformation using traditional approach.

A) Schematic of transforming hMSC using a carcinogen (nickel sulfate) induction model. Transformation was assessed after 11day periodical carcinogen (nickel sulfate) treatment vs cell growth (72h), proliferation marker expression, and telomerase mRNA expression. All cells were labeled with quantum dot conjugated Telomerase mRNA probe via Fluorescent In-Situ Hybrydization (FISH); Topoisomerase II-α were labeled with antibodies and Alexa488 dye; Cell nuclei were counterstained with Hoeschst 33342 dye. Cell growth evaluation was performed by image-based automatic counting cells at 72h and normalized to the 4h control. Quantitative for Topoisomerase II-α and Telomerase mRNA expression were performed based on fluorescent intensity normalize to each single cells. **B)** Expression of certain known cancer stem cell markers (CD44, CD133 and Stro-1) were evaluated via flow cytometry. All data points were normalized to normal hMSC. **C)** Telomerase expression level of hMSC at early (72h) time point of transformation compared with normal hMSC and transformed hMSC (MSC-TSR). No telomerase expression difference was observed at 72h post nickel sulfate treatment. **D)** Further visualization of the telomerase based transformation index. Telomerase based transformation index was calculated through the following equation:

$$Transformation\ Index = \frac{Telomerase\ \ expression\ \ of\ MSC_{72h\ Ni\ treatment}\ -Telomerase\ \ expression\ \ of\ MSC_{normal}}{Telomerase\ \ expression\ \ of\ MSC_{TSR}\ -Telomerase\ \ expression\ \ of\ MSC_{normal}},$$

(Equation 5-2), where transformation index was normalized to a value that lies in the range of 0 (normal MSC)-1(fully transformed MSC). Telomerase based

transformation index at early carcinogen treatment (72h) was close to normal MSC side.

5.3.2.3 Early High Content Nuclear Features Capture Long Term hMSC Oncogenic Transformation

Under periodical carcinogen treatment, differences in transformation behavior were observed in hMSC. Therefore, an interesting question was raised: can the onset of transformation be detected for these cells at early timepoints? Notably, typical cancer detection markers such as telomerase expression failed to sensitize onset transformation at the first 72h after nickel sulfate treatment (**Figure 5.3c**). The telomerase based transformation index plot (**Figure 5.3d**) showed that 72h carcinogen induced hMSC were much closer to normal hMSC compared with genetically transformed hMSC. On the other hand, early cell nuclear morphology and nuclear protein organization of single cells may hold some clues to the long-term abnormal transformation since changes in the nuclear protein organizational may occur earlier than changes in cancer related gene expression profiles. The reduced-feature dimension plot depicted the localization of nickel sulfate treated hMSC population in-between the reference cell populations (hMSC in green and genetically transformed hMSC in red) (**Figure 5.4a**), with 72h nickel sulfate treated hMSC population in the middle region (in black) Further visualization of nuclear descriptor based prediction on the degree of transformation of hMSC was demonstrated in **Figure 5.4b**. In this figure, iAz was generated from classifications of nuclear descriptors of 72h

carcinogen induced hMSC compared with both negative controls (normal hMSC) and positive controls (MSC-TSR) using the technique described in the methods section. iAz was plotted on a one dimensional 'ladder' line, with left end being normal hMSC labeled with '0' and right end being genetically transformed hMSC labeled with '1'. The 72h carcinogen treated hMSC has a iAz value of 0.48, locating in the middle region of the transformation ladder. Taken together, this indicated that early nuclear protein NuMA features could mirror the onset and progression of the carcinogen induced transformation process.

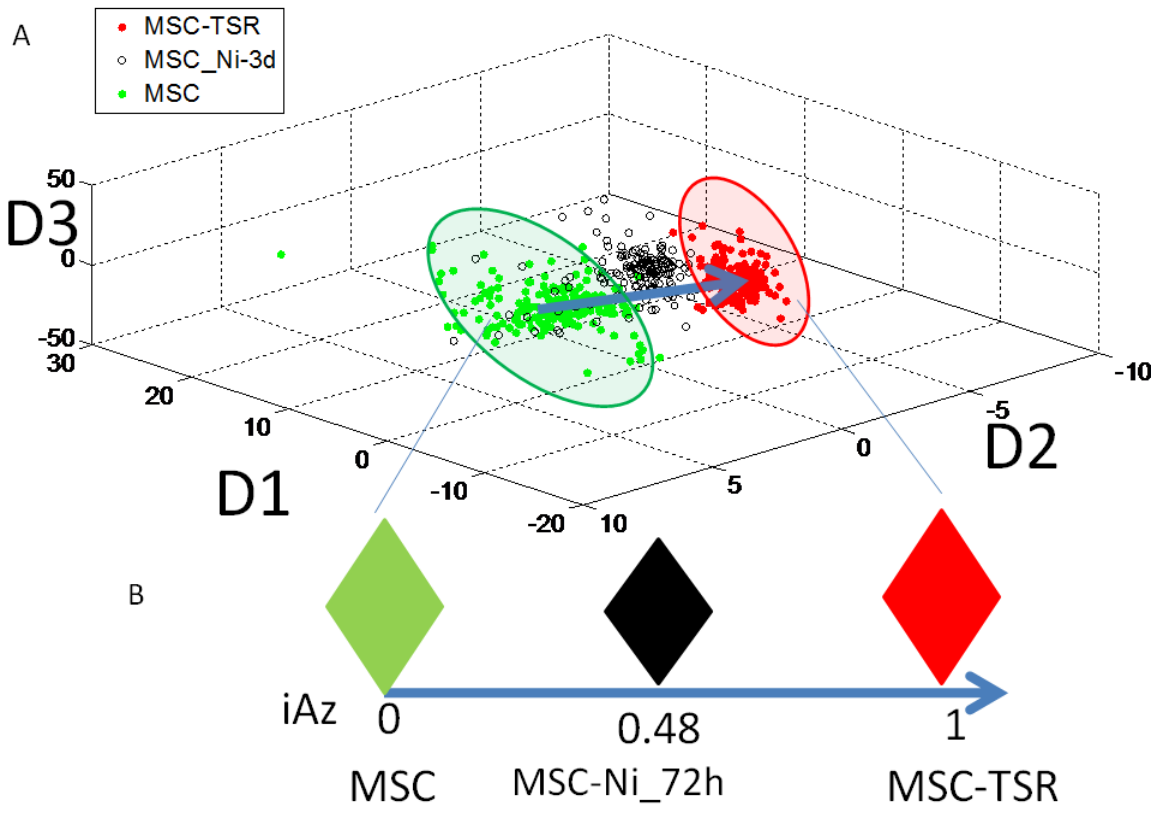

Figure 5.4: Characterization of carcinogen-induced hMSC transformation using high content nuclear descriptor based profiling.

A) Visualization of high content nuclear descriptors after feature dimension reduction. Three-dimensional plots of dimension-reduced nuclear descriptors represented mathematical grouping of original nuclear descriptor pool. **Green**: descriptors from normal hMSC, **Black**: hMSC with 72h nickel sulfate treatment, **Red**: genetically transformed hMSC (MSC-TSR). Three clusters were shown in the plot, the evaluation of how close carcinogen treated hMSC to either normal hMSC or transformed hMSC were sketched and further implemented through the use of SVM based classifier. **B)** Visualization of the location of 72h carcinogen induced hMSC in between normal hMSC (0) and genetically transformed hMSC (1). iAz values was calculated from classifications on nuclear descriptors, as described in the methods section. Results were demonstrated in a one-dimensional arrow plot, with left end being normal hMSC and right end being genetically transformed hMSC. Early carcinogen induced hMSC lied in the middle of the transformation arrow, with an iAz value of 0.48.

5.3.2.4 Forecasting hMSC Transformation on Synthetic Polymer Substrates Based on 72h High Content Nuclear Descriptors

We next examined whether the high content nuclear descriptors could be used to screen the susceptibility of hMSC to transformation when cultured on complex extracellular microenvironments modulated by combinatorial polymeric biomaterials (**Figure 5.5b & Table 5.1**). Twelve polymers with diverse physicochemical properties were used as the test set based on their ability to slow down or speed up the carcinogen induced hMSC transformation process.

Examination of the hMSC telomerase expression post 11day periodic carcinogen treated demonstrated differential degree of transformation, as shown in **Figure 5.5a.**

It was shown in **Figure 5.5a** that the hMSC transformation process was differentially modulated on these biomaterials substrates, with transformation index ranging from (0 to 0.5). Utilizing the high content nuclear feature extraction and SVM based classification approach described in the methods section; we generated a predictor for each individual biomaterial substrate that described the degree of transformation process. This predictor value was compared with the experimentally observed telomerase expression based transformation index at 11 day post-carcinogenic transformation induction for the same biomaterial substrate. A high Pearson correlation coefficient of 0.8737 was acquired between the nuclear descriptor based predictors and the 11day telomerase expression based transformation index (**Figure 5.5c**).

A

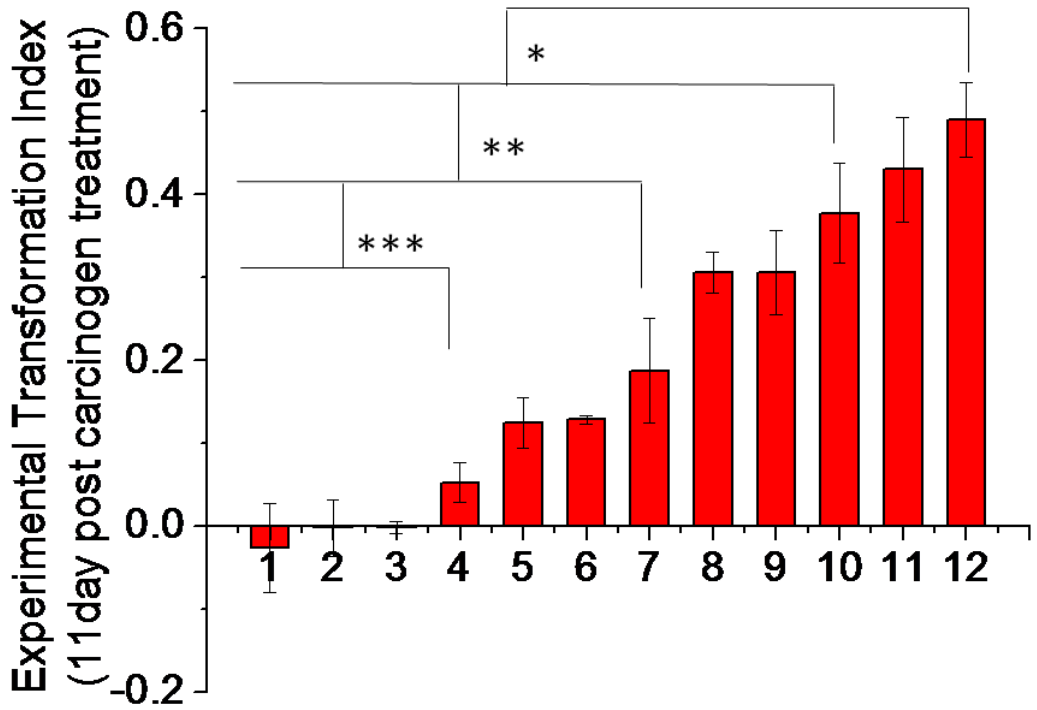

7

B

❑ polycarbonates

Poly(*x*%DTE-*co*-*y*%DT-*co*-*z*%PEG_{1000} carbonate)

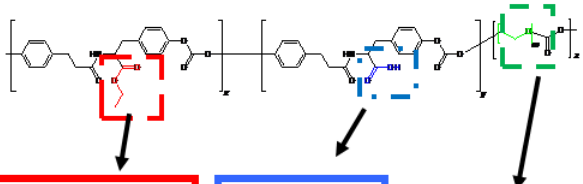

Variation in Alkyl Ester Pendent Chain	Addition of Carboxylate Group	Addition of PEG
Hydrophobicity	Hydrophilicity	Hydrophilicity
Stiffness	Anti-oxidative	Pro-oxidative
Tensile Strength	Protein Adsorption	Stiffness
		Degradation rate

❑ poly(L-lactic acid)

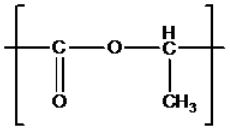

❑ polymethacrylates

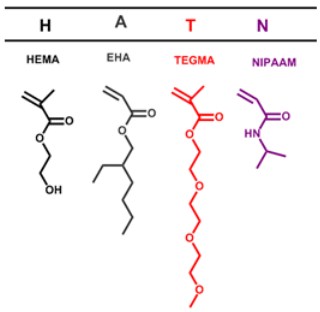

A40H35: p(40%EHA-co-35%HEMA)

A55H20: p(55%EHA-co-20%HEMA)

A40T35: p(40%EHA-co-35%TEGMA)

A25H50: p(20%EHA-co-55%HEMA)

H10N65: p(10%HEMA-co-65%NIPAAM)

H40T35: p(40%HEMA-co-35%TEGMA)

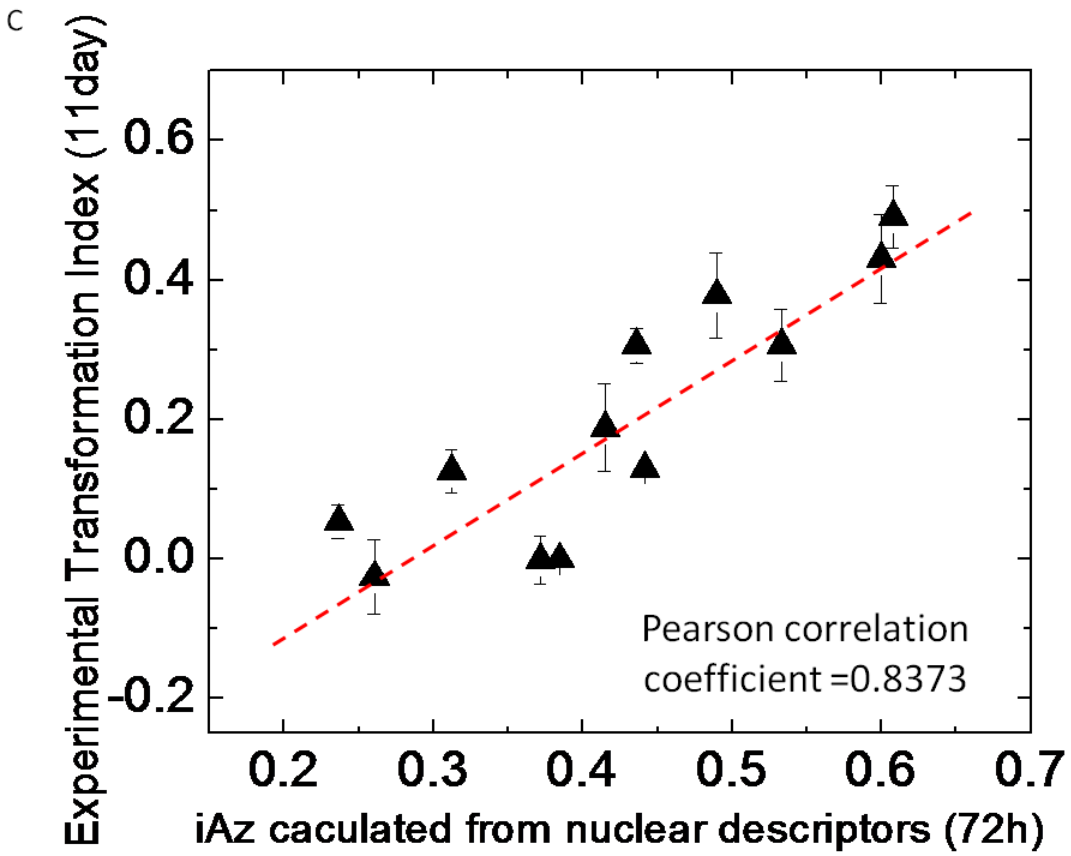

Figure 5.5: Forecasting degree of hMSC transformation using high content nuclear descriptor based profiling.

A) Quantification of telomerase based transformation index for hMSC cultured on each substrate after 11day periodic carcinogen treatment ranging from approximately 0 to 0.5. Error bars represent the standard deviation of N=2-4 experiments per substrate. **(B)** Key chemical structures of biomaterials (listed in **Table 5.1**) used in this study. **(C)** Scatter plot of iAz (X-axis) calculated from 72h high content nuclear descriptor based classification (generated as described in the methods section) vs the experimental transformation index acquired from telomerase data on 11 day carcinogen treated cells to those non-carcinogen treated cells on the same substrate (Y-axis). A high degree of correlation

between the iAz and observed transformation index was acquired (Pearson correlation coefficient = 0.8737). The Y error bars represent the standard deviation for N=2-4 independent experiments.

Table 5.1: A list of biomaterial substrates

Substrate index	Substrate name
1	poly(10%HEMA-co-65%NIPAAM)
2	poly(82%DTE-co-8%PEG-co-10%DT carbonate)
3	poly(DTE carbonate)
4	poly(40%HEMA-co-35%TEGMA)
5	poly(90%DTE-co-10%DT carbonate)
6	poly(55%EHA-co-20%HEMA)
7	poly(L-lactic acid)
8	poly(40%EHA-co-35%HEMA)
9	poly(20%EHA-co-55%HEMA)
10	coverglass
11	poly(40%EHA-co-35%TEGMA)
12	poly(92%DTE-co-8%PEG carbonate)

5.4 Discussion

Our high content imaging based profiling platform is based on the ability to identify cell populations using nuclear protein markers instead of alternative phenotypic readouts. The value of our approach is its ability to identify subtle differences of nuclear features resulting from stem cell transformation. Moreover, this approach enables prediction of long term cell behavior at the first 24-72h culture, thereby reducing the necessity of using multiple molecular

markers for characterization. As our platform is based on high content imaging and computational data mining, it could potentially be applied to various fields as long as the cell type can attach to a substrate and can be imaged with appropriate nuclear protein marker(s) stained.

The cell nuclear descriptors used in this study, which was derived mainly for a nuclear protein, NuMA, support the notion that structure and organization of the nuclear proteins and DNA in the nucleus has cell- and tissue- specific determinants, or 'signatures'. As one of the four most abundant proteins in the cell nucleus in eukaryotic cells, NuMA was found to be closely associated with cell cycle related events, such as normal proliferation and apoptosis, cancerous progression, stem cell self-renewal (symmetric division), stem cell differentiation (asymmetric division). One of the roles of NuMA that have been heavily investigated is regulation of cell cycle progression during cancerous progression. Lelievre and her colleagues reported that the degree of malignancy of breast cancer cells had committant patterns of NuMA expression and organizational features through the investigation of benign, malignant breast cancer cells, together with reversely engineered breast cancer cells[131,165,166]. Therefore, our high content nuclear descriptors could virtually capture the competition between stem cell self-renewal and oncogenic transformation. Moreover, our approach allows evaluation of substrates that differentially regulate the transformation process at early time-points.

One interesting finding of this study was that biomaterials differentially modulated cell transformation processes. Some polymeric biomaterials, such as

p(92%DTE-co-8%PEG carbonate), synergistically worked with metal carcinogen, nickel sulfate in culture, denoting a higher degree of transformation compared with other substrates (**Figure 5.5a**), while other biomaterials, such as p(DTE-co-8%PEG-co-10%DT carbonate) acted against nickel sulfate induced transformation process. The role that biomaterials played in the transformation progress is not quite clear, however, there are two possible explanations. First, it could be attributed to the modulation of reactive oxygen species (ROS) imbalance and oxidative stress, which were generally believed to have an important role in the initiation of cellular injury by triggering a cascade of radical reactions, enhancing secondary ROS generation, stimulating inflammatory cytokine production, altering gene expression and other cellular modifications and finally lead to diseases including cancer[82,86,309]. Our previous studies showed that these polymeric substrates were characterized for their intrinsic ability to generate ROS. PEG-containing substrates induced both exogenous and intracellular ROS production, whereas the charged substrates reduced production of both types, indicating coupling of exogenous ROS generation and intracellular ROS production[310]. The aforementioned reason is based on the assumption of no interaction between the nickel compound and the polymeric substrate; however, in some instances such as negatively charged DT-containing polymer substrate, it could electro-statically attract nickel ions to the polymer surface, thereby limiting the binding of nickel ions around/in target cells at site. This ionic binding event of nickel to cellular components has also been identified to be responsible for inducing cancer by International Agency for Research on

Cancer (IARC) in 1990 through mechanistic and animal studies[82-84,304]. According to IARC, DNA strand breaks, mutations, chromosomal damage, cell transformation, and disrupted DNA repair were observed in cell-culture studies with the existence of nickel compounds. The reduction-oxidation activity of the nickel ion reacting with cellular molecular may produce ROS that attack DNA or induce cell signaling pathways[82,84]. Moreover, ROS production can also result from Haber-Weiss-type mechanisms (**Equation 5-3**), where nickel ion acts a catalyst[84],

$$O_2^{\cdot -} + H_2O_2 \xrightarrow{metal^{n+1}/metal^{n+}} {}^{\cdot}OH + O_2 + OH^- \qquad \text{(Equation 5-3)}$$

Through ROS-mediated reactions, nickel compounds cause lipid peroxidation, protein modification, DNA damage and chromosome abberation, ROS have been shown to act as signal transduction messengers both alone and as activators of signal transduction pathways. Nickel compounds affect a number of receptors and genes, including growth factor receptors factors (EGF, VEGF, PDGF) Ras signaling, mitogen-activated protein kinases, nuclear transcription factors NF-kB, AP-1, p53, NFAT, and HIF-1 by both ROS-dependent and ROS-independent mechanisms[82-84,304]. Therefore, the reduced amount of nickel ion on DT containing polymer substrate could result in less physical attack to cells and DNA and subsequently less transformation. And the nuclear descriptors at 72h also showed this DT effect as demonstrated in **Figure 5.5b,** with all DT containing polymers at low end of transformation.

To note, the telomerase based transformation index showed that the degree of transformation using nickel sulfate is not high, with ~50% of genetically

transformed hMSC (**Figure 5.5a**) although growth and other functional assays did confirm the transformation process (**Figure 5.3a&b**). This could due to the use of hMSC of relatively low passage number (less than passage 20) under carcinogen treatment in this study. As shown in literature, hMSC transformation is a chronic process, usually takes place in 5-6 months of culture when hMSC reached senescence stage and are more susceptible to spontaneous or carcinogen induced transformation[33,75-77,311]. This also explains the possible reason why our early nuclear descriptors tend to over-predict the transformation process (**Figure 5.5b**), with correlation curve shifted to the right side of the origin. Therefore, longer induction may be necessary for improved predictions, however, current correlations could be used as early rank-ordering of biomaterials' susceptibility to transformation.

It is noteworthy that nuclear descriptors in this study can be used determine the degree of transformation, regardless of the methods to transform hMSC, either genetically or carcinogen induction. Stem cell transformation is a complicated process that still needs comprehensive investigation, which is further challenged by the possibility that the cancer phenotype after transformation could be more than a single cancer type. Literature reports have shown that bone marrow derived mesenchymal stem cells could give rise to a variety of tumor types, such as sarcoma, epithelial tumors, neural tumors, muscular tumors, tumors of fibroblasts, blood vessel endothelial tumors and so on[312], Therefore, using telomerase as a functional cancer marker seemed an expedient but realistically an efficient marker to identify general cell transformation. Moreover,

one of the clinical concerns is to avoid cancerous transformation of stem cells after implantation, regardless of specific cancer phenotypes stem cells will transform into. Thus, our high content nuclear descriptor based screening platform could potentially be used for biomaterials design and screening. In the future, cancer markers specific for certain molecular pathways could be used as a functional marker, and the selection of appropriate nuclear protein marker, which is more specific to that cancer phenotype could also be used apart from NuMA, whose expression and organizational features may only report global but not specific cell cycle progression as a result of the cell transformation process.

Another interesting application enabled by this method is the possibility of identifying stem-like cell subpopulation in cancer cells, given that our high content nuclear descriptors based approach could capture the stem cell self-renewal vs cancerous progression. Therefore, further studies are warranted to identify stem-like subpopulation in heterogeneous breast cancer cells and preliminary results indicate some success of our proposed high content profiling platform (data shown in Chapter 6).

To adapt this method to other applications with different cell types requires merely the availability of effective staining of nuclear proteins (not limited to NuMA but potentially other nuclear proteins as well), fluorescent imaging equipment, image-based feature extraction and data mining software (either in house or commercially available), which are cell type-independent or application-independent and represent a common set of tools enabled by the advances in microscopy, computer vision and machine learning field. In particular, our

profiling platform is highly adaptable to both two-dimensional and three-dimensional systems with more markers (some preliminary data shown in the future work section), better methods for resolving fluorescent signals, especially for 3-D applications as demonstrated in chapter 2.

5.5 Conclusion

We have demonstrated that through a “high-content” nuclear based profiling platform it is possible to identify different state of stem cells (transformed vs normal) at early time points. As a proof of concept, this platform was first built on predicting genetically transformed hMSC over normal hMSC. Further utilities were expanded to predict the degree of transformation of hMSC under carcinogen induction cultured on various extracellular stimuli as modulated by polymeric substrates. We are the first to show that organizational patterns of cell nucleus and nuclear proteins can be used to identify differences in the stem cell fate decision process amongst individual cells in a population of cells, such as the balance between self-renewal vs cancer transformation/progression. Additionally, it was also shown that substrate chemistry played a critical role in the balance of self-renewal and transformation of stem cells, shedding some light on the control of stem cell niche for regenerative medicine in cancer treatment. Moreover, the ability to identify cellular response early on may allow us to establish a timeline for cellular self-renewal/ transformation and identify critical points in cellular evolution for further screening. This platform also has the potential for identifying and separating heterogeneous cell populations that could

be useful in the future for cell sorting given sufficient incorporation with flow-cytometry related equipment. It is also worthwhile to note that this platform is so versatile that it can also be applied to rapid screening of combinatorially designed substrates for directed stem cell differentiation, or cancer drug treatment to identify customized biomaterials or anti-cancer drugs in regenerative medicine and cancer treatment.

6 Research Summary and Future Directions

6.1 Research Summary

This dissertation focuses on the development and applications of high resolution and “high-content” subcellular imaging based profiling approaches. The overall hypothesis of the thesis is that high content subcellular imaging based profiling methodology can capture the changes of cellular responses, including but not limited to cell adhesion, spreading, stem cell self-renewal, differentiation and transformation, to various extracellular stimuli in a quantitative manner and enable predictive insights of stem cell fates.

To test the above hypothesis three specific aims were addressed. First, we developed a multiphoton imaging based approach to quantitatively characterize cellular response to three-dimensional scaffolding biomaterials. This methodology was based on fluorescence multiphoton microscopy (MPM) to image and quantitatively characterize the microstructure and cell–substrate interactions within microporous scaffold substrates fabricated from synthetic biodegradable polymers. Image-based features were extracted to profile cell-biomaterial interactions, thus generating 3-D biomaterial scaffold microstructure descriptors, and pseudo-3D whole cell morphological descriptors. Second, a more comprehensive high content profiling method was examined, incorporating an expanded set of cell morphological descriptors including intensity based expression descriptors and texture/spatial organization descriptors. This high content analysis was coupled with rapid screening platforms, such as the use of

two-dimensional gradient-based polymer coated substrates, to enable simultaneous elucidation of cell response to continuous changes in surface roughness and discrete changes in surface chemistry. The gradient and high-content approaches synergized to provide rapid assessment of cell response to material composition and topography while providing in depth single cell features that responded to these material factors. Finally, the high content platform was refined further to incorporate high content information about intracellular nuclear organization that may hold clues into cellular functional fates. By selecting nuclear proteins as subcellular reporters and introducing more sophisticated data mining/modeling approach, we sought to identify and predict stem cell related behaviors, including stem cell self-renewal, differentiation, transformation, and etc. This “enhanced” version of the high content profiling platform was first built on predicting self-renewal vs differentiation behavior of mesenchymal stem cells under various culture conditions. The subsequent version was utilized to predict stem cell self-renewal vs transformation. These findings highlight the versatility of this high content imaging based profiling platform in that we are among the first to report that organizational pattern of cell nucleus and nuclear proteins can be used to identify a broad range of stem cell fate decision process, such as the balance between self-renewal vs differentiation, self-renewal vs cancer transformation/progression. Additionally, it was also shown that substrate chemistry played a critical role in the balance of self-renewal and transformation of stem cells, shedding some light on the control and harness of stem cell niche for regenerative medicine in cancer treatment.

Results from this thesis strengthen the utility of high-content subcellular imaging to capture early cell response leading to divergent different stem cell behaviors. Previous work from our laboratory by Treiser et al. have shown that incorporation of texture features with intensity and morphology features of whole cell and cytoskeleton protein actin could enhance classification of mesenchymal stem cells going into different lineages[277]. The actin based profiling however has limited applicability in dense cell culture conditions, which is more representative of physiological conditions. Moreover, cytoskeleton-based discrimination of cells also failed to identify mesenchymal stem cell self-renewal vs lineage commitment. On the other hand, researchers from cancer research community indicated the importance of cell nuclear features, using image based grey scale feature extraction with classification techniques, in aiding cancer diagnosis and prognosis[140-142,159]. One of the advantage of probing cell nucleus or nuclear proteins can minimize the need for complicated image segmentation efforts while expanding the utility of the high content platform to a broader applications where cell-cell contact are ubiquitous.

In fact, this study found that changes in nuclear features may be one alternative to probe cellular behaviors, as phenotypical changes of cells are inevitably accompanied by regulation of nuclear proteins, especially matrix proteins could play a role in the coordination of gene expression networks and signaling that link the ”outside-in signaling”. Therefore, the cell nucleus features could be utilized to identify different state of the cells, including self-renewal, differentiation, transformation, and possibly aging, apoptosis. In this study we

chose to apply our high content subcellular profiling platform to investigate human mesenchymal stem cell self-renewal, osteogenic vs adipogenic differentiation and transformation as a test case. Similar approaches could be tested to examine cellular differentiation to other lineages such as chondrogenic, myogenic, neuronal and so on[52,53,133,271,313-320]. In conclusion, this dissertation has presented a single cell based characterization approach that provides: quantitative characterization of subcellular features at early time points, prediction of different state of cells (not limited to stem cells) such as self-renewal, differentiation and transformation, identifying stem cell/precursor cells of various origins, and capture of heterogeneity of cell populations, and capability to parse cell response to complex extracellular stimuli or biomaterial substrates.

6.2 Ongoing and Future Directions

6.2.1 Analysis of Other Subcellular/Nuclear Molecules for Descriptor Generation

The study of the inner organization of the cell nucleus is emerging as a critical path to further the understanding of state change of cells, represented by controlled specific gene expression. Our study focused on profiling changes of state of the cells through high-content imaging of nuclear protein expression and organizational features within cell nucleus. A nuclear protein, NuMA was selected for the following reasons: first, its abundance in most mammalian cells makes it potentially useful for multiple applications. Second, NuMA is an essential player in cell cycle progression in that it aids mitotic spindle assembly

and maintenance. Studies have shown the different expression and organizational patterns as cells undergo different proliferation paces, such as self-renewal, transformation[136,164,165,280]. Third, NuMA and its invertebrate homologs play a similar tethering role at the cell cortex, thereby mediating essential asymmetric divisions during development[287]. Fourth, as a nuclear matrix protein, it is also a structural component of the nucleus, and is responsible for maintaining nuclear integrity, keeping appropriate genomic order and organization as well as functional identity[279-281,295]. Given the central role of NuMA, we hypothesized that high content descriptors of NuMA reflecting quantitative information of NuMA protein expression, nuclear morphology and organizational patterns, could thereby provide useful information for further cellular response. In the future, other nuclear components could also be analyzed and subjected to similar high content analysis. Candidate nuclear component molecules include the heterochromatin/euchromatin family, and splicing factor speckles that are major components in chromatin remodeling[156,160,165,166,321]. It is known that chromatin remodeling is necessary to modify expression of specific genes underlying a state change of cells. The major characteristics of these nuclear components, as reported so far, are the concentration of heterochromatin at the nuclear periphery, DNAase sensitive chromatin at the nuclear periphery, formation of larger and fewer splicing factor speckles and the presence of transcription permissive areas around splicing factor speckles (**Figure 6.1**).

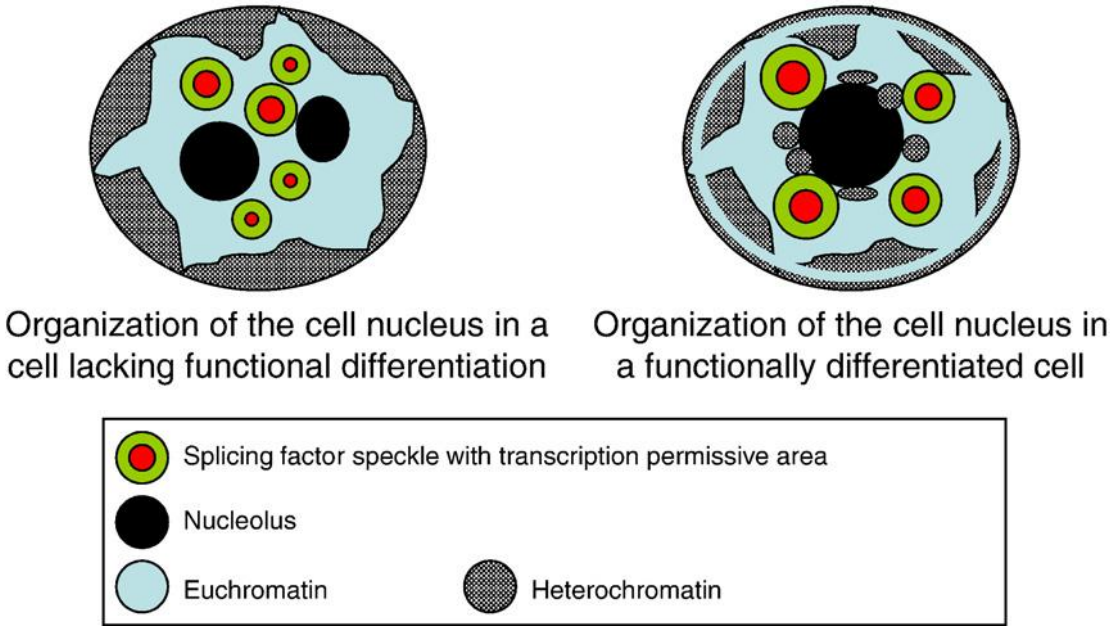

Figure 6.1: Patterns of nuclear organization depending on the differentiation stage.

A number of reports have shown that upon differentiation into functional tissues (e.g., tissues that have acquired the organization and function typically found in normally developed organs), major characteristics of nuclear organization that can be observed include large splicing factor speckles, the concentration of heterochromatin domains at the periphery of the nucleolus, and the presence of DNAse sensitive chromatin at the nuclear periphery (right drawing). Before this differentiation stage or upon loss of this differentiation stage, this typical organization was not observed (left drawing). Figure used by permission from Elsevier (License number 2554461244565).

Certain proteins whose translocation mediates the inside-out nuclear signaling may also be good candidates for the high content descriptor based approach. One such candidate is nuclear lamina, made of intermediate filament proteins, lamins A/C and B, which is associated mostly with transcriptional silencing[61,152,292-295,322]. Moreover, lamina also plays a role in mechanotransduction from outside to inside of cell nucleus. The cell nucleus has been identified to have a compartment within which mechanotrasduction could occur. Some proteins such as emrin, can bridge the actin cytoskeleton and the nuclear actin polymer via the lamina[157]. Cell substrate interactions start at the interfaces, where cells utilize integrins, adhesion receptor molecules, to initiate binding to ligands adhering to the substrate surface[135,147,159,283,285,323-327]. Integrins also represent the mechanosensory machinery of the cell. The generation of force at integrin binding site leads to local focal adhesion assembly and activation of signaling cascades and gene transcription[324,327-330]. For instance, activation of focal adhesion kinase (FAK), mitogen activated protein (MAP) kinase and the Ras GTPase superfamily, further activate a number of downstream intracellular proteins and signaling molecules and regulate cellular functions ranging from proliferation, differentiation, apoptosis to migration, all of which represent change of cell state. Thus, integrins could also serve as proteins whose organization and intensity may lend themselves to high content information extraction and modeling.

The state change of cells is a complicated process, involving biochemical and mechanical signaling from outside to inside of cell nucleus. We could

envision that communication between cell extracellular matrix, cytoskeleton and chromatin in the cell nucleus could form a large network encompassing all these factors together to guide the signaling outputs, proliferation, differentiation, and transformation. Therefore, a systems biology based approach is highly desirable to reconstruct a large scale network that mimic cellular-signaling network, but utilize high content features of probes at both nuclear level and extra-nuclear level together with gene expression profiles.

6.2.2 Expanding the Utility

The ultimate goal of the proposed high content cell imaging based profiling platform is to be useful for a wide range of clinical-related applications, not only stem cell based regenerative medicine, but also cancer treatment. In regenerative medicine, stem/progenitor cells in large-scale clinical applications are usually acquired from various sources with seemingly identical molecular marker expression, but may in fact possess different capacities for self-renewal and differentiation. The selection of appropriate stem cell/precursor cell source is especially critical for the clinical success of stem cell therapies. To this end, one potential application of our approach is to discern early differences in stem cells isolated from different regions of the central nervous system, as described next.

6.2.2.1 Identifying Precursor Cells from Different Origins

Oligodendrocyte Precursor Cells Display Divergent Self-renewal and Differentiation Potential

Oligodendrocyte-type-2 astrocyte progenitor cells (O-2A/OPCs) derived from different brain regions are expected to possess different long-term self-renewal and differentiation patterns of oligodendrocyte generation, which mirrors the timing of myelination in vivo[331]. However, O-2A/OPCs, isolated from the optic nerve, cerebral cortex, and optic chiasm, are typically antigenically indistinguishable and share similar differentiation behaviors. Ongoing efforts seek to evaluate the long term differentiation and self-renewal properties and examine determine whether O-2A/OPCs from two distinct sources of tissues, the cerebral cortex (CX) and corpus collosum (CC), have measurable intrinsic differences. O-2A/OPCs from CX and CC are closely associated in proximity as well as the timing of myelination that occurs in these brain tissues.

First, O-2A/OPCs plated at clonal density and cultured in proliferation promoting media containing 10ng/mL PDGF-AA revealed that both CX and CC derived O-2A/OPCs were responsive to the mitogen but underwent different self-renewing behaviors. Clones generated from single O-2A/OPCs originating in the CX tended to form much larger colonies on average than clones generated from single CC O-2A/OPCs (**Figure 6.2a&b**). Only 4% of clones from CX derived O-2A/OPCs contained a single oligodendrocyte whereas 20% of clones from CC derived O-2A/OPCs contained at least one oligodendrocyte. These results suggested that CX derived O-2A/OPCs were more prone to self-renewal and less prone to differentiation as compared to CC derived O-2A/OPCs in proliferation culture conditions. When media conditions favored differentiation (1ng/mL PDGF-AA + 0.49nM T3/T4), even larger differences became evident between the two

populations of O-2A/OPCs. After 7 days in differentiation media, 71% of CC-derived O-2A/OPCs contained at least one oligodendrocyte, with 22% of clones containing at least 5 oligodendrocytes(**Figure 6.2c&d**). In contrast, only 29% of clones derived from CX O-2A/OPCs contained at least a single oligodendrocyte, with just 3% containing 5 or more oligodendrocytes. Thus, marked differences were seen in self-renewal and differentiation characteristics of O-2A/OPCs isolated from cerebral cortex (CX) and corpus collosum (CC).

The varied self-renewal and differentiation properties we observed in different O2-A/OPC populations could represent a developmental progression[331-333], for which precursor cells from some specific regions possess a more mature pattern of behavior than other regions, thereby forming a developmental continuum of myelination. As all cells were isolated from animals of the same age invoking a developmental progression would require positing a different timing of this progression in each tissue, which may make these populations biologically different from each other. Further, the fact that O2-A/OPC(CX) continueed to express their characteristic potential for continuous and extended self-renewal in vitro, compared with O2-A/OPC(CC) seemed to suggest that the properties of these different populations may contribute to the diverse time courses of differentiation in different CNS regions.

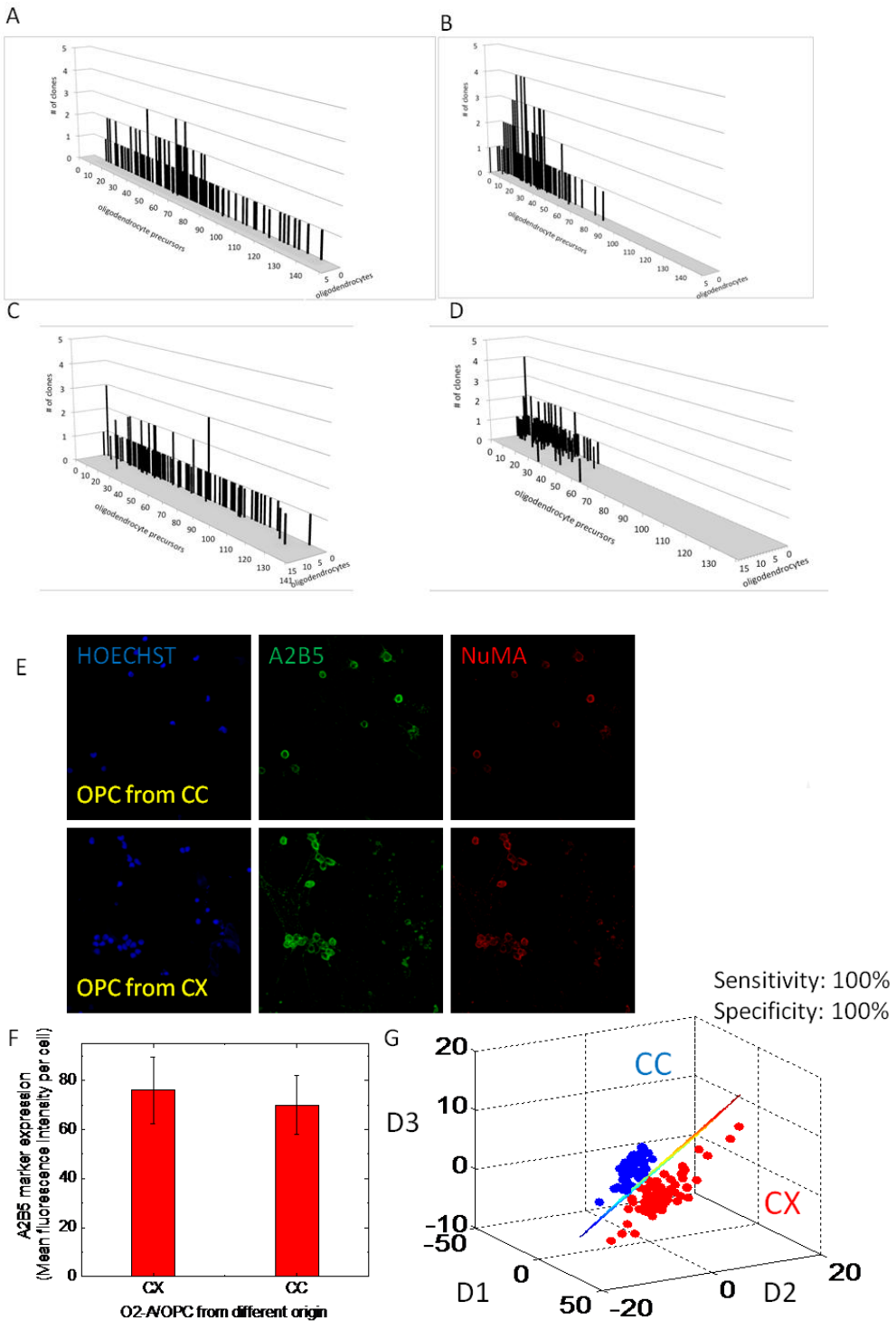

Figure 6.2: Identifying oligodendrocyte precursors from different regions of brain (cerebral cortex and corpus collosum) via long term functional assays and high content nuclear descriptors based profiling approach.

A-B) Proliferation assays performed on O-2A/OPC from cerebral cortex (A) and (B); **C-D)** Differentiation assays performed on O-2A/OPC from cerebral cortex (C) and (D); In these 3D plots, X-axis represents the number of precursors in a clone, Y-axis represents number of colonies with a specific composition, Z-axis represents the number of oligodendrocytes in a clone. **E)** Marker staining to identify olygodendrocyte precursor cells using A2B5 marker. All cells were stained with A2B5 and NuMA antibodies and Alexa488 and Alexa594 secondary antibody respectively for visualization, cell nuclei were counterstained with Hoechst 33342 dye. **F)** A2B5 marker expression failed to demonstrate difference of O-2A/OPC from cerebral cortex and corpus collosum. A2B5 expression was quantified as mean fluorescence intensity per cell. **G)** High content nuclear descriptor based approach to visualize and classify O-2A/OPC from cerebral cortex and corpus collosum, SVM-based classification returned a 100% sensitivity and specificity respectively between cerebral cortex and corpus collosum derived O-2A/OPC.

Next, we applied our high content nuclear based profiling method on these O2-A/OPCs identified through A2B5 marker staining (**Figure 6.2e**). Quantified A2B5 marker expression did not return noticeable difference between O2-A/OPC from CC and CX **(Figure 6.2f**). NuMA based uclear descriptors were extracted from NuMA and Hoechst staining. After performing nuclear feature dimension reduction and classifications, the integrated nuclear descriptors were visualized in 3-D feature space. Two distinct clusters, presumably corresponding to O-

2A/OPC(CC) and O-2A/OPC(CX) respectively(**Figure 6.2g**) were demonstrated. Further SVM-based classification was performed and results indicated a perfect separation between the two clusters, with 100% sensitivity and 100% specificity.

In this ongoing study we asked whether it is possible to help identify O-2A/OPCs with properties that might be associated with divergent patterns of development in different central nervous system (CNS) regions without performing long term proliferation or differentiation studies. Conventional means to define O-2A/OPCs is through A2B5+ staining, regardless of their origin. Examination of these A2B5+ cells revealed that all of these populations behave identically in terms of their final fate: stellate phenotype of type-2 astrocytes[334], which characterize the O2-A/OPCs. The only difference reported in literature is their different self-renewal and differentiation response as they are from different sources, such as optical nerve, cortex and optic chiasm[331]. Therefore, there is currently no reported effective way to identify the origin of O-2A/OPCs at early stages without performing long-term differentiation studies as shown above. Perhaps the most remarkable finding of this study is that high content nuclear descriptors can identify precursor cells whose self-renewal characteristics and response to inducers of differentiation differ in precursor cell origin but all give rise to oligodendrocytes and are isolated from postnatal animals of a single age. The difference of CC and CX derived O2-A/OPCs is mostly because of the intrinsic biological tendency to undergo self-renewal and their response to inducers of oligodendrocyte generation, in other words, tissue-specific properties. One possible cell-intrinsic property that regulates self-renewal and

responsiveness to induction factors is the intracellular redox (reduction/oxidation) state, as shown by other researchers[331,335,336]. It could be that the redox state modifies the ability of extracellular signaling molecules that shuttle between cell nucleus and extracellular environment, and in turn modify the balance between self-renewal and differentiation, as can be probed by NuMA protein and high content analysis, which quantitatively captures self-renewal vs differentiation.

6.2.2.2 Identifying Heterogeneous Stem-like Subpopulation in Breast Cancer Cells

The discovery of stem-like subpopulation, sometimes called cancer stem cells, in cancer cells opened up a new strategy for fighting cancer from its origin[13,337,338]. This stem-like subpopulation possesses certain stem cell properties, such as self-renewal. Moreover, these cancer stem cells can evade conventional anti-cancer drug treatment and later on result in cancer recurrence. Therefore, successful identification of the stem-like subpopulation could potentially help design anti-cancer drug that target the cancer initiating subpopulation. To this end, identifying stem-like subpopulations within breast cancer is currently being investigated as another test case.

The phenotypic and functional differences between cells that initiate human breast tumors (cancer stem-like cells) and those that comprise the tumor bulk are difficult to study using only primary tumor tissue. Since high content nuclear descriptors can capture the transformation of stem cells, another interesting question is raised: could it be used to identify stem-like population

within cancer cell population? The premise is that since NuMA is a cell cycle related protein, cancer cells that have abnormally high proliferate capability should display different nuclear signatures compared with slow growing cancer initiating cells, also known as stem-like cells within the cancer population. To address this question, breast cancer cells (SUM149) were used to train the classifier, with a known mixed population of phenotypic markers CD24+/CD44-low(~50%) and CD24-/CD44+ (~50%)[339-341]. In SUM149 cell line and other breast cancer cell lines, CD24-/CD44+ cell population was reported to have stem-cell like behavior. In this experimental setup, surface marker CD44 and CD24 were used for initial feature set identification of two subpopulations (**Figure 6.3a**); nuclear protein marker, NuMA, was used for high content nuclear descriptors profiling. Visual observation of CD24 and CD44 channel of SUM149 cell images confirmed the heterogeneity, as reported in literature[339,340]. A later step was to extract high content nuclear descriptors from NuMA channel and pinpoint the cells according to the CD24-CD44+ and CD24+CD44- subpopulations as identified from the initial phenotypic marker set. Dimension reduction and SVM-based classifier on the two subpopulations of SUM149 cells returned 96% for sensitivity and 97.06% for specificity respectively (**Figure 6.3b**). This indicated that high content nuclear descriptors could be used to identify heterogeneous subpopulation. Using the two subpopulations in SUM149 cells as training set, further validation experiment was performed on a similar breast cancer cell type, SUM159 cell line with a more homogeneous subpopulation (~90% CD24-CD44+ and ~10% CD24+CD44-)[340]. Similarly, two subpopulations

were point picked based on CD24/CD44 expression and the high content nuclear descriptors from these subpopulations were subject to SVM classifications respectively. A predictor value of 0.1341 was acquired for CD24-CD44+ subpopulations in SUM159 cells, indicating the closer relationship to the CD24-CD44+ subpopulation in SUM149 cells (**Figure 6.3c**). Comparatively, a predictor value of 0.8125 was acquired for CD24+CD44- subpopulations in SUM159 cells, indicating the closer relationship to that of SUM149 subpopulations.

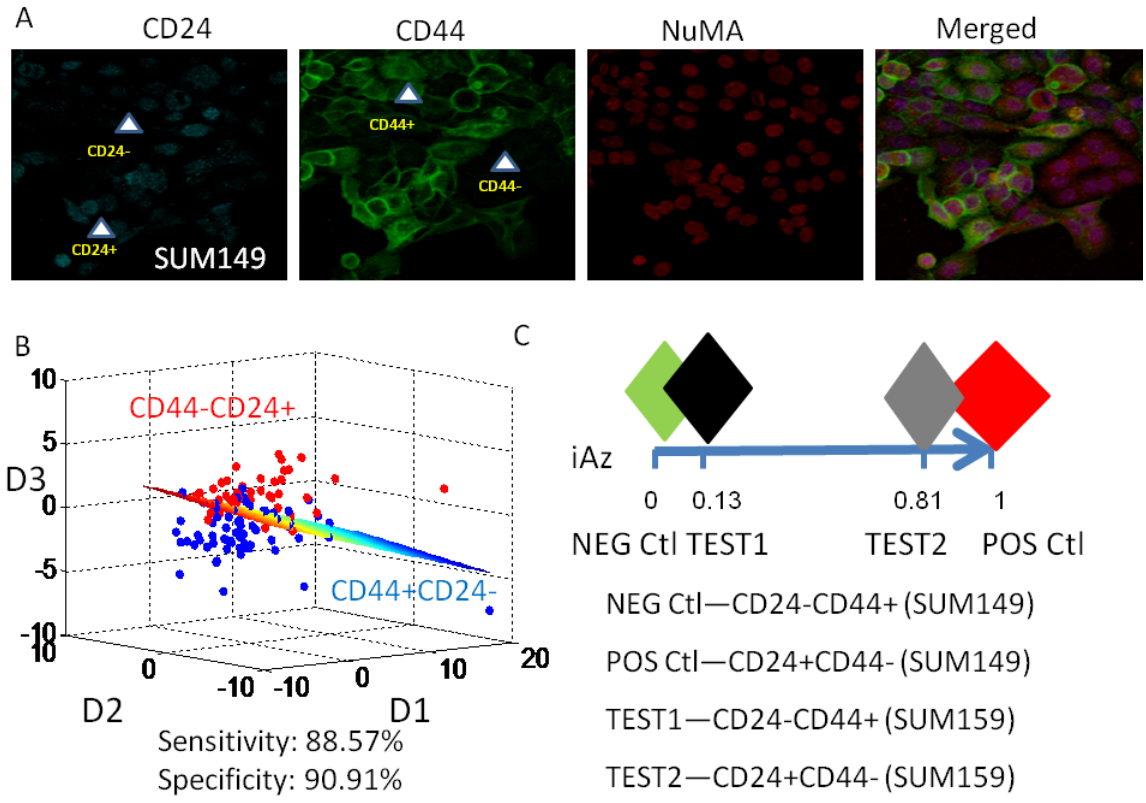

Figure 6.3: Identifying heterogeneity within breast cancer cells using surface marker expression and high content nuclear descriptors.

A) immunostaining of surface markers CD24 (left 1), CD44(left 2) and nuclear protein NuMA (right 1), with respective antibodies and alexa 647, alexa488 and alexa594 respectively and merged (right2) together. **B)** Visualization of high

content nuclear descriptors of CD24+CD44- and CD24-CD44+ subpopulation in SUM149 cells. Classification results showed 88.57% sensitivity and 90.91% specificity of the nuclear descriptors to parse out heterogeneity of breast cancer cells. **C)** Validation of high content nuclear descriptor based parsing. The two subpopulations in SUM149 were used as training sets (0: stem-like subpopulation, 1: regular cancer subpopulation). SUM159 cells, with approximately 90%CD24-CD44+ and 10% CD24+CD44- subpopulations were used as test sets. iAz values showed the location of the two test sets in the negative (0) and positive controls (1), with iAz value of 0.1341 for CD24-CD44+ subpopulation in SUM159 and 0.8125 for CD24+CD44- in SUM159.

To note, the CD44+CD24- subpopulation in the breast cancer cells have been reported by different groups to possess stem cell-like properties, including ability of self-renewal, cancer-initiating on certain circumstances[339-341]. This is consistent with our high content nuclear descriptor outcomes, which show differences between CD44+CD24- subpopulation from other subpopulations, where there are mostly rapidly proliferating cancer cells. In other words, the high content nuclear descriptors in this breast cancer cell study could capture the self-renewal behavior vs cancerous progression. On the other hand, CD44 and CD24 also serve as readouts for breast cancer cells, which can be classified into luminal-type (those express luminal keratins) and basal-type (those express stratified epithelial keratins) based on CD44 and CD24 expression[337,339-343]. CD44+/CD24- cells exhibit features of basal cells and express genes that are

involved in motility, whereas CD24+/CD44- cells exhibit features of more differentiated luminal epithelial cells and express genes involved in hormone responses. The differences of the high content nuclear descriptors of these two subpopulations may also mirror the differences of basal cell phenotype from differentiated phenotype[340,342]. Therefore, further studies are needed to delineate whether the high content descriptors report dominantly the differentiation phenotype or simply capture the self-renewal over cancer progression.

6.2.3 Pushing the High Content Profiling Platform to 3D

In the regenerative medicine or cancer research community, the ultimate goal is the ability to regenerate 3-D functional tissue. Therefore, cellular response on 2-D systems is the simplest model to start with, however, may not be representative for actual cell response in 3-D by nature. In the past few decades, 3-D studies have been focused on culture, expansion and differentiation of cells in 3-D scaffolds in a variety of applications[264,344-348]. Studies have shown the differences of cells on 3-D culture from 2-D culture, for instance, the organization and type of focal adhesions formed in 3-D environments are distinct from those formed in their 2-D counterparts. In addition, studies have demonstrated extracellular matrix forces are generally transmitted to cells differently when the cells are on two-dimensional (2-D) vs. in three-dimensional (3-D) and in turn regulate different patterns of focal adhesions, and later cell proliferation, survival, migration, and invasion[349,350]. Moreover, extensive studies have demonstrated the advantage of using 3-D culture system

for improved in vitro/ex vivo expansion and differentiation of both embryonic and adult stem cells[65,346,347,351-353]. Ongoing research efforts in the Moghe laboratory also demonstrated that certain 3-D scaffolds of specific chemistry and microstructure can modulate the in-vitro expansion and differentiation of embryonic (ES) cells and induced pluripotency (iPS) cells. Interestingly, the corresponding pseudo-3D nuclear descriptors could also capture the loss of stemness or lineage commitment, as demonstrated in **Figure 6.4** and **Figure 6.5** respectively. In the preliminary experiment, iPSCs were cultured on electrospun poly(DTE carbonate) scaffold stained with stemness marker SOX2 and nuclear protein marker NuMA and nuclei Hoechst (Images shown in **Figure 6.4a**). Our pseudo-3D nuclear descriptors demonstrated the difference between SOX2 positive and SOX2 negative cells, indicating the organizational difference between iPSCs retaining stemness vs losing stemness (**Figure 6.4b**). Further studies on variation of scaffold chemistry and geometry are necessary to calibrate these responses to the environment. On the other hand, preliminary studies on hES cell (H9) differentiation also showed that nuclear descriptors could be used to parse out lineage committed H9 cells from undifferentiated H9 cells. Shown in **Figure 6.5a**, following neurogenic induction for 3 days, hES cells became two distinct populations, with one population having stemness, as denoted by OCT4 positive cells and the other population losing stemness, as denoted by OCT4 negative cells (**Figure 6.5b**). The pseudo-3D nuclear descriptor also demonstrated a clear separation, with a sensitivity of 95.19% and specificity of 88.72%, between neuro-precursor cells and non-lineage committed

H9 cells (**Figure 6.5c**). Further studies are needed to address specific lineage commitment.

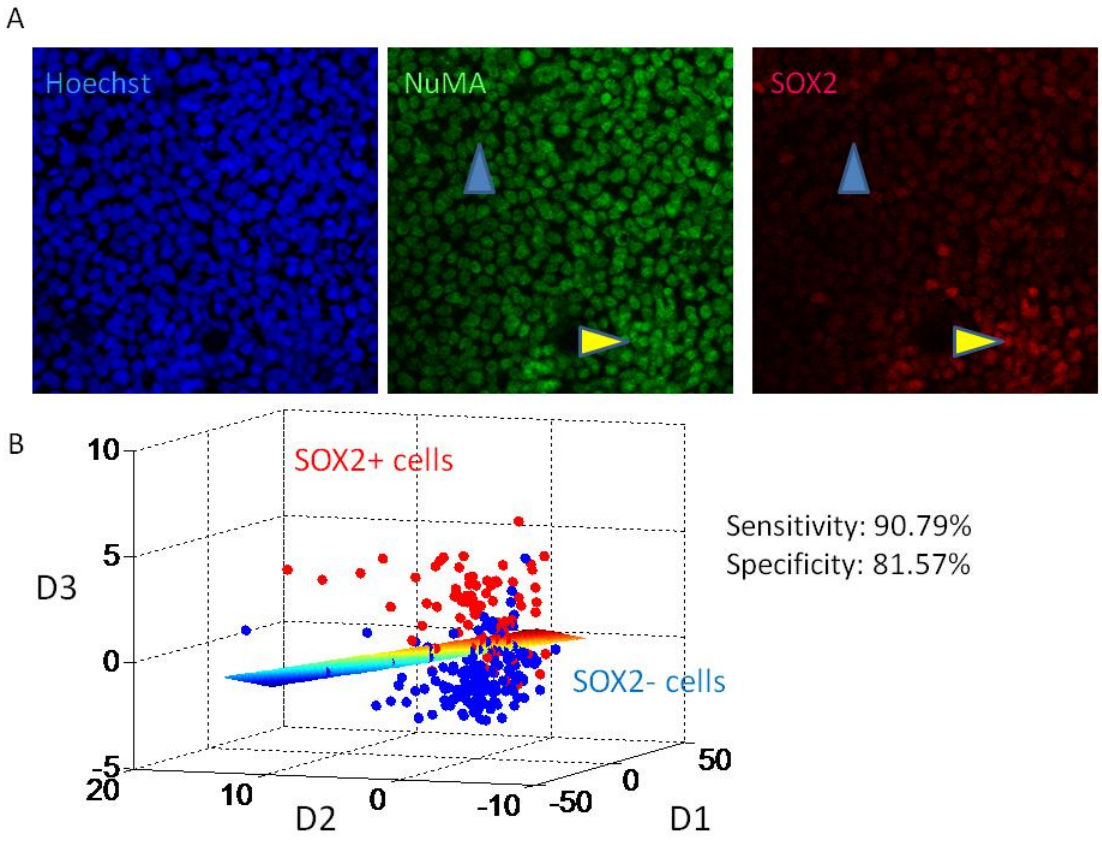

Figure 6.4: Identifying heterogeneity within iPSCs cells using marker SOX2 expression and high content nuclear descriptors.

A) Immunostaining of cell nuclesi (left), nuclear protein NuMA (middle), and stemness marker SOX2(right) labeled with primary antibodies and conjugated alexa488 and alexa594 secondary antibodies respectively. **B)** Visualization of high content nuclear descriptors of SOX2+ and SOX2- subpopulations. Classification on nuclear descriptors from SOX2+ and SOX2- subpopulation returned a sensitivity of 90.79% and specificity of 81.57% respectively.

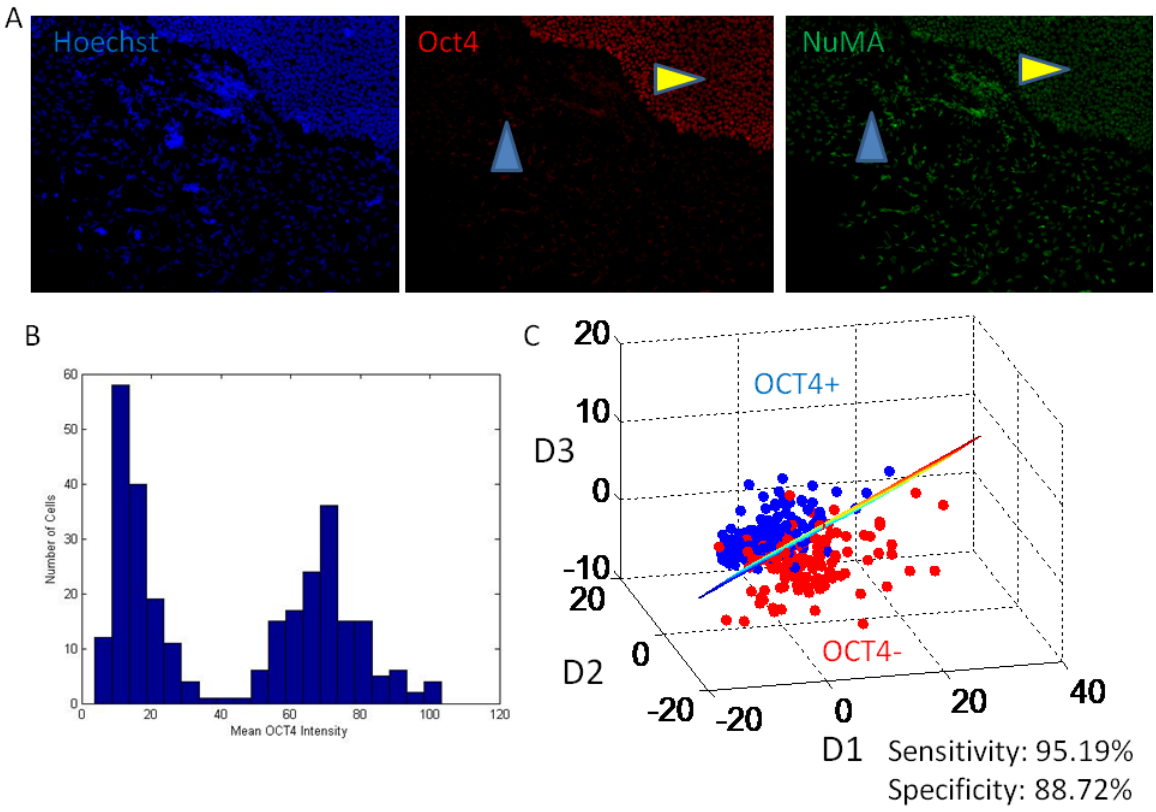

Figure 6.5: Identifying lineage committed cells within hESCs using stemness marker OCT4 expression and high content nuclear descriptors.

A) Immunostaining of cell nuclesi (left), stemness marker OCT4 (middle) and nuclear protein NuMA (right), labeled with primary antibodies and conjugated alexa4594 and alexa488 secondary antibodies respectively. **B)** Visualization of OCT4 expression within neurogenically induced (3day) hESCs. The histogram of OC4 expression showed a bi-modal distribution of cells with OCT4 high and OCT4 low subpopulation. **C)** Visualization of high content nuclear descriptors of OCT4 high and OCT4 low subpopulations. Classification on nuclear descriptors from OCT4+ and OCT4- subpopulation returned a sensitivity of 95.19% and specificity of 88.72% respectively.

Currently, our high-content descriptor based profiling platform has been demonstrated in two-dimensional cultures and some emerging 3-D applications, including deriving 3-D scaffold descriptors and pseudo-3D cell morphology descriptors due to limitation of image analysis capabilities. However, recent technical development has made it possible to derive true 3-D cell descriptors. Therefore, another challenging task for the future will be to develop mathematical model to classify and predict various cellular responses in 3-D. It would be interesting to investigate the correlations of the 2-D descriptors, pseudo-3D descriptors and true-3D descriptors to the overall cell response in 3-D. Successful prediction of the cellular response could provide a powerful alternative to characterize early cellular response in 3-D for better diagnosis/treatment in regenerative medicine and cancer research.

6.2.4 Other Thoughts

The high-content subcellular imaging based profiling methodology discussed within this dissertation represents a new approach to characterize and forecast cell response to extracellular stimuli. However, compared with other traditional techniques such as flow cytometry, the utility is limited despite its inherent advantages. The biggest limitation of our current high content profiling platform is that it relies largely on fixed attached cells instead of live cells; thereby live cell sorting is barely possible. However, live cell sorting is currently more desirable in biology related research labs or companies, representing a large market value. Therefore, there are several technical hurdles to overcome in

order for our high content profiling platform to become widely useful for the community: First, there is a great need to seek a non-invasive method to label cells that does not perturb the functions of the cells, either with endogenous fusion proteins (e.g. GFP live-act) or even using label-free cells but derive other cell descriptors using other optical imaging techniques such as phase contrast or Coherent anti-Stokes Raman spectroscopy(CARS)[354-356]. Second, a system that can locally detach selected cells (e.g. some gel system that can detach local cells given certain heat stimuli) is highly desirable for live cell sorting. Third, a seamless integration of the cell culture and processing equipment, imaging equipment, image analysis, data mining and computational modeling is also critical for the utility of this platform. Fourth, if non-attached cells could also be utilized to acquire cell descriptors that capture different cellular response, a high content flow cytometry could be developed through the combination of our high content profiling with the flow cytometer.

7 Appendix

7.1 Identification of the most influential cytoskeletal/nuclear descriptors for parsing hMSC lineage commitment (AD vs OS vs BA)

In an effort to determine critical cell descriptors for hMSC lineage commitment, PCA analysis was performed to reduce the descriptor feature space (50+ dimensions) into three non-correlated dimensions (corresponding to top three highest Eigen values), with each principal component (PC1, PC2, PC3) representing a linear combination of cytoskeletal/nuclear descriptors. The criterion to determine the most influential descriptors was based on the weighting factors of each descriptor in the linear transformation in PCA analysis. For each principal component, the descriptors were identified as influential if the weighting factor was more than half of the highest weighting factor in that transformation equation. As a result, by reviewing the weighting factors of each linear combination, a subset of cytoskeletal/nuclear descriptors were identified as influential descriptors.

PCA analysis on actin based cytoskeletal descriptors revealed that all three categories of cytoskeletal descriptors (reporter morphology, expression and spatial distribution) were of importance to parse out lineage commitment (AD, OS, BA) of hMSC (**Table 7.1**). On the first principal component, with an Eigen value of 19.2 accounting for ~50% of the variability of the original dataset, the most influential descriptors were actin morphology descriptors (mostly descriptors for diameter, perimeter and area) and actin expression descriptors (density sum and IOD). On the second principal component (Eigen value of 5.90

accounting for ~15% of variability of the original dataset), only actin morphology descriptors (mostly descriptors for diameter and area) were identified as most influential. On the third principal component, which were about equally important as the second principal component (an Eigen value of 5.12), all three categories of actin descriptors were identified as influential, such as heterogeneity and density std.dev (spatial distribution descriptors); density mean, density sum and IOD (actin expression descriptors); box X/Y, perimeter ratio (shape factor for morphology descriptors).

Similarly, all three categories of NuMA based nuclear descriptors were found to be important after PCA analysis (**Table 7.2**). On the first principal component, with corresponding Eigen value of 20.9 accounting for ~40% of the variability of the original nuclear descriptor dataset, the most influential nuclear descriptors were mostly descriptors for diameter, perimeter and area (nuclear morphology descriptors). On the second principal component (Eigen value of 6.67 accounting for ~14% of the original dataset), all three categories of nuclear descriptors were identified as influential, including heterogeneity and density std.dev and clumpiness (spatial distribution descriptors); density mean, density min, density max, density sum and IOD (NuMA expression descriptors); area/box and perimeter ratio (morphology descriptors). On the other hand, only nuclear morphology descriptors (area/box and perimeter ratio) were found to contribute to the third principal component.

After data fusion process (described in chapter 4), dimension reduced cytoskeletal descriptors (Actin PC1-3) and nuclear descriptors (NuMA PC1-3)

were combined into six dimensions and underwent further PCA based dimension reduction (results shown in **Table 7.3**). Interestingly, the final three dimensions reduced from six dimensions (three cytoskeletal and three nuclear descriptors) were of relatively the same contributions to the dataset, with Eigen values of 1.39, 1.21 and 1.00 respectively. Moreover, the descriptors identified as most influential were PC2 and PC3 from both cytoskeletal and nuclear descriptors, comprising of all three categories of descriptors (morphology, expression and spatial distribution) but less contribution from morphology descriptors (ruling out contributions of actin/nuclei perimeter descriptors while keeping only shape, area, diameter descriptors).

Table 7.1: A list of cytoskeletal descriptors identified as most influential from PCA analysis in parsing hMSC lineage commitment (AD, OS) from non-differentiated (BA) state

Descriptor categories were color-coded as blue, green and red representing morphology descriptors, actin expression descriptors and actin spatial distribution descriptors respectively.

PC1 (Eigen value=19.2)		PC2 (Eigen value=5.90)		PC3 (Eigen value=5.12)	
Top descriptors	Weight	Top descriptors	Weight	Top descriptors	Weight
Feret (mean)	0.223	Radius (min)	0.310	Heterogeneity	0.370
Perimeter (convex)	0.222	Area/Box	0.285	Density (std.dev.)	0.358
Diameter (mean)	0.217	Axis (minor)	0.260	Density (mean)	0.310
Perimeter (ellipse)	0.217	Diameter (min)	0.243	Box X/Y	0.242
Perimeter	0.214	Area (polygon)	0.171	Perimeter (ratio)	0.234
Area (polygon)	0.207	Feret (min)	0.154	Density (sum)	0.227
Area	0.207	Size (width)	0.153	IOD	0.227
Per Area (Obj./Total)	0.207	Area	0.151		
Perimeter3	0.206	Per Area (Obj./Total)	0.151		
Feret (max)	0.203				
Size (length)	0.198				
Radius (max)	0.193				
Diameter (max)	0.192				
Feret (min)	0.183				
Axis (major)	0.182				
Dendrites	0.177				
End points	0.177				
Size (width)	0.177				
Box Height	0.172				
IOD	0.169				
Density (sum)	0.169				
Perimeter2	0.169				
Dendritic length	0.166				
Axis (minor)	0.165				
Diameter (min)	0.163				

Table 7.2: A list of nuclear descriptors identified as most influential from PCA analysis in parsing hMSC lineage commitment (AD, OS) from non-differentiated (BA) state

Descriptor categories were color-coded as blue, green and red representing morphology descriptors, NuMA expression descriptors and NuMA spatial distribution descriptors respectively.

PC1 (Eigen value=20.9)		PC2 (Eigen value=6.67)		PC3 (Eigen value=5.48)	
Top descriptors	Weight	Top descriptors	Weight	Top descriptors	Weight
Perimeter (ellipse)	0.217	Density (mean)	0.270	Perimeter (ratio)	0.215
Diameter (mean)	0.217	Density (max)	0.266	Area/Box	0.158
Feret (mean)	0.216	Perimeter (ratio)	0.263		
Area	0.216	Density (std.dev.)	0.255		
Area (polygon)	0.216	IOD	0.236		
Perimeter (convex)	0.214	Density (sum)	0.236		
Perimeter	0.208	Heterogeneity	0.231		
Per Area (Obj./Total)	0.206	Density (min)	0.231		
Count (adjusted)	0.204	Area/Box	0.191		
Diameter (max)	0.200	Clumpiness	0.120		
Feret (max)	0.200				
Size (length)	0.199				
Feret (min)	0.198				
Axis (minor)	0.198				
Perimeter2	0.198				
Size (width)	0.196				
Diameter (min)	0.196				
Axis (major)	0.195				
Perimeter3	0.195				
Radius (min)	0.193				
Box Width	0.188				
Box Height	0.176				

Table 7.3: List of composite descriptors identified as most influential from PCA analysis in parsing hMSC lineage commitment (AD, OS) from non-differentiated (BA) state

Descriptor categories were color-coded as yellow and purple representing dimension reduced actin based cytoskeletal descriptors (Actin PC1-3) and NuMA based nuclear descriptors (NuMA PC1-3) respectively.

PC1 (Eigen value=1.39)		PC2 (Eigen value=1.21)		PC3 (Eigen value=1.00)	
Top descriptors	Weight	Top descriptors	Weight	Top descriptors	Weight
Actin PC2	0.598	Actin PC3	0.708	NuMA PC3	0.777
NuMA PC2	0.481	Actin PC2	0.399		

7.2 Identification of the most influential nuclear descriptors for parsing hMSC transformation

Similarly, PCA based dimension reduction was applied to NuMA based nuclear descriptors of hMSC and the transformed phenotypes (results shown in **Table 7.4**). The first principal component, with corresponding Eigen value of 19.55 accounting for ~40% of the variability of the original nuclear descriptor dataset, were composed of nuclear morphology descriptors for diameter, perimeter and area and NuMA expression descriptors (IOD and Density sum). On the second principal component (Eigen value of 6.62 accounting for ~14%), all three categories of nuclear descriptors were identified as influential, including heterogeneity and density std.dev (spatial distribution descriptors); density mean, density max, density sum and IOD (NuMA expression descriptors); per area, aspect and perimeter ratio (shape descriptors). Similarly, all three categories of descriptors contribute to the third principal component, including diameter, area, and shape descriptors from (morphology descriptors category), density mean, density min, density sum, IOD (NuMA expression descriptors category), and hole ratio, heterogeneity and density std.dev (spatial distribution descriptors). Notably, NuMA expression and spatial distribution descriptors had more contributions to the dimension-reduced dataset: IOD and Density sum appeared in all three PCs while heterogeneity and density std.dev appeared in PC2 and PC3. This may be attributed to the fact that transformed cells tend to proliferate faster than normal hMSC, whose proliferative capability can be captured by proliferation markers such as NuMA protein expression.

Table 7.4: A list of nuclear descriptors identified as most influential from PCA analysis in parsing transformed hMSC (genetically transformed or carcinogen induced) from normal hMSC

Descriptor categories were color-coded as blue, green and red representing morphology descriptors, NuMA expression descriptors and NuMA spatial distribution descriptors respectively.

PC1 (Eigen value=19.55)		PC2 (Eigen value=6.62)		PC3 (Eigen value=5.05)	
Top descriptors	Weight	Top descriptors	Weight	Top descriptors	Weight
Feret (mean)	0.222	Density (std.dev.)	0.300	Perimeter (ratio)	0.245
Perimeter (convex)	0.222	Density (max)	0.296	Density (mean)	0.235
Perimeter (ellipse)	0.221	Heterogeneity	0.289	Density (min)	0.213
Diameter (mean)	0.220	IOD	0.265	IOD	0.212
Area (polygon)	0.218	Density (sum)	0.262	Hole Ratio	0.209
Area	0.217	Per Area (Obj./Total)	0.245	Radius (min)	0.192
Perimeter	0.217	Perimeter (ratio)	0.203	Area/Box	0.187
Diameter (max)	0.215	Aspect	0.152	Box X/Y	0.148
Feret (max)	0.215	Density (mean)	0.151	Segmentation range	0.136
Size (length)	0.213			Diameter (min)	0.135
Radius (max)	0.212			Heterogeneity	0.112
Perimeter3	0.211			Density (std.dev.)	0.112
Diameter (max)	0.211			Density (min)	0.110
Perimeter2	0.209				
Feret (min)	0.191				
Size (width)	0.190				
Box Height	0.188				
Diameter (min)	0.181				
Box Width	0.175				
Radius (min)	0.167				
IOD	0.150				
Density (sum)	0.149				

7.3 Identification of the most influential nuclear descriptors for parsing O-2A/OPCs derived from cerebral cortex (CX) and corpus collosum (CC)

PCA based dimension reduction was performed on nuclear descriptors of CC or CX derived O-2A/OPCs (results shown in **Table 7.5**). The first principal component, with corresponding Eigen value of 24.91 accounting for ~50% of the variability of the original nuclear descriptor dataset, were composed of nuclear morphology descriptors (including diameter, perimeter, roundness and area descriptors). On the second principal component (Eigen value of 7.85 accounting for ~15% of the variability of the original dataset), all three categories of nuclear descriptors were identified as influential, including heterogeneity, density std.dev, clumpiness and margination (spatial distribution descriptors); density mean, density max, density min, density sum and IOD (NuMA expression descriptors); radius, dendrites and area/box (shape descriptors). The third principal component was solely composed of morphology descriptors including roundness, dendrites descriptors. To note, PC3 accounted for only ~7% of original dataset, and was not as important as the first two principal components.

Table 7.5: A list of nuclear descriptors identified as most influential from PCA analysis in parsing O-2A/OPC from different sources (CC, CX)

Descriptor categories were color-coded as blue, green and red representing morphology descriptors, NuMA expression descriptors and NuMA spatial distribution descriptors respectively.

PC1 (Eigen value=24.91)		PC2 (Eigen value=7.85)		PC3 (Eigen value=3.53)	
Top descriptors	Weight	Top descriptors	Weight	Top descriptors	Weight
Feret (mean)	0.202	Density (mean)	0.322	Roundness	0.303
Perimeter (convex)	0.202	Density (max)	0.314	Dendrites	0.271
Perimeter (ellipse)	0.201	Heterogeneity	0.314	End points	0.271
Count (adjusted)	0.199	Density (std.dev.)	0.312	Radius Ratio	0.255
Perimeter	0.199	Density (sum)	0.259	Fractal Dimension	0.253
Perimeter2,	0.199	IOD	0.259	Dendritic length	0.247
Perimeter3	0.199	Density (min)	0.255	Aspect	0.181
Area	0.198	Clumpiness	0.193		
Area (polygon)	0.197	Radius (min)	0.182		
Diameter (max)	0.197	Margination	0.176		
Feret (max)	0.197	Dendrites	0.175		
Size (length)	0.196	End points	0.175		
Radius (max)	0.196	Dendritic length	0.169		
Diameter (mean)	0.196	Diameter (min)	0.151		
Per Area (Obj./Total)	0.196	Area/Box	0.143		
Axis (major)	0.194				
Box Width	0.194				
Box Height	0.194				
Feret (min)	0.191				
Size (width)	0.190				
Axis (minor)	0.180				
Cluster	0.176				
Roundness	0.138				
Diameter (min)	0.134				

7.4 Identification of the most influential nuclear descriptors for parsing heterogeneous subpopulation of breast cancer cells

PCA based dimension reduction was performed on nuclear descriptors of two subpopulations (CD24-CD44+/CD24+CD44-) of breast cancer cell lines (including SUM149 and SUM159). The first principal component, with corresponding Eigen value of 20.54 shown in **Table 7.6**, was composed of nuclear morphology descriptors (including diameter, perimeter and area descriptors) and NuMA expression descriptors (IOD and density sum). On the second principal component (Eigen value of 6.40 accounting for ~14% of the variability of the original dataset), only morphology descriptors (diameter, area, and shape descriptors) were identified as most influential. To note, the third principal component only accounted for ~8% of total variability of the original dataset, however, it was composed of NuMA expression descriptors, including density mean, density max, density sum, IOD, and spatial distribution descriptors, including density std dev and heterogeneity.

Table 7.6: A list of nuclear descriptors identified as most influential from PCA analysis in parsing CD24-CD44+ and CD24+CD44- subpopulations within breast cancer cell lines (SUM149 and SUM159)

Descriptor categories were color-coded as blue, green and red representing morphology descriptors, NuMA expression descriptors and NuMA spatial distribution descriptors respectively.

PC1 (Eigen value=20.54)		PC2 (Eigen value=6.40)		PC3 (Eigen value=4.38)	
Top descriptors	Weight	Top descriptors	Weight	Top descriptors	Weight
Feret (mean)	0.219	Radius (min)	0.296	Density (mean)	0.433
Perimeter (convex)	0.219	Area/Box	0.282	Density (std.dev.)	0.423
Perimeter (ellipse)	0.218	Diameter (min)	0.247	Heterogeneity	0.415
Perimeter	0.217	Axis (minor)	0.217	Density (max)	0.362
Perimeter2,	0.216	Perimeter (ratio)	0.206	Density (sum)	0.216
Perimeter3	0.216	Feret (min)	0.181	IOD	0.216
Area	0.215	Size (width)	0.178		
Area (polygon)	0.215				
Diameter (mean)	0.215				
Feret (max)	0.204				
Diameter (max)	0.204				
Size (length)	0.203				
Radius (max)	0.201				
Axis (major)	0.198				
Per Area (Obj./Total)	0.196				
IOD	0.182				
Density (sum)	0.182				
Feret (min)	0.182				
Size (width)	0.181				
Axis (minor)	0.179				
Box Width	0.172				
Box Height	0.171				
Diameter (min)	0.170				

7.5 Identification of the most influential nuclear descriptors for parsing heterogeneous subpopulation of iPSCs

PCA based dimension reduction was performed on nuclear descriptors of SOX2+ and SOX2- subpopulations of iPSCs. The first principal component, with corresponding Eigen value of 23.23 shown in **Table 7.7**, was composed of nuclear morphology descriptors (including diameter, perimeter and area descriptors) and NuMA expression descriptors (IOD and density sum). On the second principal component (Eigen value of 6.62 accounting for ~18% of the variability of original dataset), morphology descriptors (shape, area, and diameter descriptors) and spatial distribution descriptors (hole ratio, heterogeneity and density std dev) were identified as most influential. The third principal component only accounted for ~9% of the variability of original dataset, however, it was a combination of NuMA expression descriptors, including density mean, density max, density min, and spatial distribution descriptors, including density std dev, heterogeneity and clumpiness.

Table 7.7: A list of nuclear descriptors identified as most influential from PCA analysis in parsing SOX2- and SOX2+ subpopulations of iPSCs

Descriptor categories were color-coded as blue, green and red representing morphology descriptors, NuMA expression descriptors and NuMA spatial distribution descriptors respectively.

PC1 (Eigen value=23.23)		PC2 (Eigen value=9.52)		PC3 (Eigen value=4.14)	
Top descriptors	Weight	Top descriptors	Weight	Top descriptors	Weight
Feret (mean)	0.204	Perimeter (ratio)	0.267	Density (mean)	0.414
Perimeter (ellipse)	0.203	Area/Box	0.240	Density (max)	0.398
Count (adjusted)	0.203	Hole Ratio	0.228	Density (min)	0.339
Diameter (mean)	0.201	Radius (min)	0.187	Density (std.dev.)	0.328
Area,	0.201	Heterogeneity	0.170	Heterogeneity	0.303
Per Area (Obj./Total)	0.201	Density (std.dev.)	0.166	Clumpiness	0.117
Area (polygon)	0.200	Diameter (min)	0.153		
Perimeter (convex)	0.197				
Diameter (max)	0.192				
Feret (max)	0.192				
IOD	0.192				
Density (sum)	0.192				
Size (length)	0.190				
Feret (min)	0.190				
Size (width)	0.186				
Radius (max)	0.186				
Axis (major)	0.186				
Axis (minor)	0.184				
Cluster	0.180				
Box Width	0.179				
Box Height	0.173				
Perimeter	0.172				
Perimeter3	0.164				
Diameter (min)	0.153				
Perimeter2	0.151				

7.6 Identification of the most influential nuclear descriptors for parsing neuronal-induced human ESCs

PCA based dimension reduction was performed on nuclear descriptors of OCT4+ and OCT4- subpopulations of human ESCs (H9). The first principal component, with corresponding Eigen value of 20.29 shown in **Table 7.8**, was composed of nuclear morphology descriptors (including diameter, perimeter and area descriptors) and NuMA expression descriptors (IOD and density sum). On the second principal component (Eigen value of 5.91 accounting for ~14% of the variability of the original dataset), only morphology descriptors (diameter, area, and shape descriptors) were identified as most influential. The third principal component was a contribution of all three categories of descriptors: including shape, area, diameter descriptors from morphology descriptors category, density mean, density max, density sum, IOD from NuMA expression descriptors category, and heterogeneity, density std.dev, clumpiness from spatial distribution descriptors.

Table 7.8: A list of nuclear descriptors identified as most influential from PCA analysis in parsing neuronal committed hESCs from non-differented hESCs

Descriptor categories were color-coded as blue, green and red representing morphology descriptors, NuMA expression descriptors and NuMA spatial distribution descriptors respectively.

PC1 (Eigen value=20.29)		PC2 (Eigen value=5.91)		PC3 (Eigen value=4.49)	
Top descriptors	Weight	Top descriptors	Weight	Top descriptors	Weight
Feret (mean)	0.220	Radius (min)	0.284	Density (std.dev.)	0.317
Perimeter (convex)	0.220	Area/Box	0.279	Density (mean)	0.310
Perimeter (ellipse)	0.218	Diameter (min)	0.258	Heterogeneity	0.304
Perimeter2,	0.216	Axis (minor)	0.203	Density (max)	0.293
Perimeter3	0.216	Perimeter (ratio)	0.192	Perimeter (ratio)	0.239
Perimeter	0.216	Per Area (Obj./Total)	0.180	Clumpiness	0.217
Area,	0.214	Feret (min)	0.155	Area/Box	0.192
Area (polygon)	0.214	Size (width)	0.154	Radius (min)	0.183
Diameter (mean)	0.213			IOD	0.178
Feret (max)	0.211			Density (sum)	0.178
Diameter (max)	0.210				
Size (length)	0.210				
Radius (max)	0.210				
Axis (major)	0.206				
Box Width	0.192				
Feret (min)	0.187				
IOD	0.185				
Density (sum)	0.185				
Size (width)	0.184				
Box Height	0.177				
Axis (minor)	0.175				

8 References

1. Badylak SF, Nerem RM. Progress in tissue engineering and regenerative medicine. Proc Natl Acad Sci U S A;107(8):3285-6.
2. Terzic A, Nelson TJ. Regenerative medicine advancing health care 2020. J Am Coll Cardiol;55(20):2254-7.
3. Fodor WL. Tissue engineering and cell based therapies, from the bench to the clinic: the potential to replace, repair and regenerate. Reprod Biol Endocrinol 2003;1:102.
4. Ringe J, Kaps C, Burmester GR, Sittinger M. Stem cells for regenerative medicine: advances in the engineering of tissues and organs. Naturwissenschaften 2002;89(8):338-51.
5. Mason C, Manzotti E. Regenerative medicine cell therapies: numbers of units manufactured and patients treated between 1988 and 2010. Regen Med;5(3):307-13.
6. Shastri VP. Future of regenerative medicine: challenges and hurdles. Artif Organs 2006;30(10):828-34.
7. Khang D, Carpenter J, Chun YW, Pareta R, Webster TJ. Nanotechnology for regenerative medicine. Biomed Microdevices;12(4):575-87.
8. Lengner CJ. iPS cell technology in regenerative medicine. Ann N Y Acad Sci;1192(1):38-44.
9. Martin I, Riboldi SA, Jakob M, Wendt D. SnapShot: Bioreactors systems in tissue engineering (TE) & regenerative medicine (RM). Biomaterials;31(11):3114-5.
10. Nicholas CR, Kriegstein AR. Regenerative medicine: Cell reprogramming gets direct. Nature;463(7284):1031-2.
11. Sheyn D, Mizrahi O, Benjamin S, Gazit Z, Pelled G, Gazit D. Genetically modified cells in regenerative medicine and tissue engineering. Adv Drug Deliv Rev;62(7-8):683-98.
12. Burness ML, Sipkins DA. The stem cell niche in health and malignancy. Semin Cancer Biol;20(2):107-15.
13. Sottoriva A, Sloot PM, Medema JP, Vermeulen L. Exploring cancer stem cell niche directed tumor growth. Cell Cycle;9(8).
14. Peerani R, Zandstra PW. Enabling stem cell therapies through synthetic stem cell-niche engineering. J Clin Invest;120(1):60-70.
15. Vazin T, Schaffer DV. Engineering strategies to emulate the stem cell niche. Trends Biotechnol;28(3):117-24.
16. surgeons Aaoo. Physician Visits for Fractures. From american academy of orthopaedic surgenons website http://www.aaos.org/Research/stats/patientstats.asp 2007.
17. Sun QY, Schatten H. Role of NuMA in vertebrate cells: review of an intriguing multifunctional protein. Front Biosci 2006;11:1137-46.
18. Foundation OI. Fast facts on osteogenesis imperfecta. From Osteogenesis imperfect foundation website http://www.oif.org/site/PageServer?pagename=FactSheetList 2003.

19. Bielack SS, Machatschek JN, Flege S, Jurgens H. Delaying surgery with chemotherapy for osteosarcoma of the extremities. Expert Opin Pharmacother 2004;5(6):1243-56.
20. Bohm P, Raecke O. [Multimodal interdisciplinary therapy to improve function and long-term survival in patients with high-grade osteosarcoma of the extremities]. Chirurg 2002;73(8):809-17.
21. Vilquin JT, Rosset P. Mesenchymal stem cells in bone and cartilage repair: current status. Regen Med 2006;1(4):589-604.
22. Hirota T, Konno K, Fujimoto T, Ohta H, Sato K, Kato S, Ohno K, Hara K. [Combined multimodal therapy for osteosarcoma--neoadjuvant chemotherapy]. Gan To Kagaku Ryoho 1999;26(8):1068-75.
23. Oldham JB, Lu L, Zhu X, Porter BD, Hefferan TE, Larson DR, Currier BL, Mikos AG, Yaszemski MJ. Biological activity of rhBMP-2 released from PLGA microspheres. Journal of Biomechanical Engineering-Transactions of the Asme 2000;122(3):289-292.
24. Brown KL, Cruess RL. Bone and cartilage transplantation in orthopaedic surgery. A review. J Bone Joint Surg Am 1982;64(2):270-9.
25. Enneking WF, Eady JL, Burchardt H. Autogenous cortical bone grafts in the reconstruction of segmental skeletal defects. J Bone Joint Surg Am 1980;62(7):1039-58.
26. Erbe EM, Marx JG, Clineff TD, Bellincampi LD. Potential of an ultraporous beta-tricalcium phosphate synthetic cancellous bone void filler and bone marrow aspirate composite graft. Eur Spine J 2001;10 Suppl 2:S141-6.
27. Fedorovich NE, Alblas J, de Wijn JR, Hennink WE, Verbout AJ, Dhert WJ. Hydrogels as extracellular matrices for skeletal tissue engineering: state-of-the-art and novel application in organ printing. Tissue Eng 2007;13(8):1905-25.
28. Kang SW, Yang HS, Seo SW, Han DK, Kim BS. Apatite-coated poly(lactic-co-glycolic acid) microspheres as an injectable scaffold for bone tissue engineering. J Biomed Mater Res A 2007.
29. Kim IY, Seo SJ, Moon HS, Yoo MK, Park IY, Kim BC, Cho CS. Chitosan and its derivatives for tissue engineering applications. Biotechnol Adv 2008;26(1):1-21.
30. Lee YM, Park YJ, Lee SJ, Ku Y, Han SB, Choi SM, Klokkevold PR, Chung CP. Tissue engineered bone formation using chitosan/tricalcium phosphate sponges. J Periodontol 2000;71(3):410-7.
31. Wahl DA, Czernuszka JT. Collagen-hydroxyapatite composites for hard tissue repair. Eur Cell Mater 2006;11:43-56.
32. Zhao G, Zinger O, Schwartz Z, Wieland M, Landolt D, Boyan BD. Osteoblast-like cells are sensitive to submicron-scale surface structure. Clin Oral Implants Res 2006;17(3):258-64.
33. Miura M, Miura Y, Padilla-Nash HM, Molinolo AA, Fu B, Patel V, Seo BM, Sonoyama W, Zheng JJ, Baker CC and others. Accumulated chromosomal instability in murine bone marrow mesenchymal stem cells leads to malignant transformation. Stem Cells 2006;24(4):1095-103.

34. Karp JM, Sarraf F, Shoichet MS, Davies JE. Fibrin-filled scaffolds for bone-tissue engineering: An in vivo study. J Biomed Mater Res A 2004;71(1):162-71.
35. Salgado AJ, Figueiredo JE, Coutinho OP, Reis RL. Biological response to pre-mineralized starch based scaffolds for bone tissue engineering. J Mater Sci Mater Med 2005;16(3):267-75.
36. Christenson L, Mikos AG, Gibbons DF, Picciolo GL. Biomaterials for tissue engineering: summary. Tissue Eng 1997;3(1):71-3; discussion 73-6.
37. El-Ghannam A. Bone reconstruction: from bioceramics to tissue engineering. Expert Rev Med Devices 2005;2(1):87-101.
38. Kneser U, Schaefer DJ, Polykandriotis E, Horch RE. Tissue engineering of bone: the reconstructive surgeon's point of view. J Cell Mol Med 2006;10(1):7-19.
39. Silver FH, Marks M, Kato YP, Li C, Pulapura S, Kohn J. Tissue compatibility of tyrosine-derived polycarbonates and polyiminocarbonates: an initial evaluation. J Long Term Eff Med Implants 1992;1(4):329-46.
40. Salgado AJ, Coutinho OP, Reis RL. Bone tissue engineering: state of the art and future trends. Macromol Biosci 2004;4(8):743-65.
41. Aliyev E, Sakallioglu U, Eren Z, Acikgoz G. The effect of polylactide membranes on the levels of reactive oxygen species in periodontal flaps during wound healing. Biomaterials 2004;25(19):4633-7.
42. Woei Ng K, Speicher T, Dombrowski C, Helledie T, Haupt LM, Nurcombe V, Cool SM. Osteogenic differentiation of murine embryonic stem cells is mediated by fibroblast growth factor receptors. Stem Cells Dev 2007;16(2):305-18.
43. Behravesh E, Yasko AW, Engel PS, Mikos AG. Synthetic biodegradable polymers for orthopaedic applications. Clin Orthop Relat Res 1999(367 Suppl):S118-29.
44. Lieb E, Tessmar J, Hacker M, Fischbach C, Rose D, Blunk T, Mikos AG, Gopferich A, Schulz MB. Poly(D,L-lactic acid)-poly(ethylene glycol)-monomethyl ether diblock copolymers control adhesion and osteoblastic differentiation of marrow stromal cells. Tissue Eng 2003;9(1):71-84.
45. Ibim SE, Ambrosio AM, Kwon MS, El-Amin SF, Allcock HR, Laurencin CT. Novel polyphosphazene/poly(lactide-co-glycolide) blends: miscibility and degradation studies. Biomaterials 1997;18(23):1565-9.
46. Laurencin CT, El-Amin SF, Ibim SE, Willoughby DA, Attawia M, Allcock HR, Ambrosio AA. A highly porous 3-dimensional polyphosphazene polymer matrix for skeletal tissue regeneration. J Biomed Mater Res 1996;30(2):133-8.
47. Treiser MD, Liu E, Dubin RA, Sung HJ, Kohn J, Moghe PV. Profiling cell-biomaterial interactions via cell-based fluororeporter imaging. BioTechniques 2007;43(3).
48. Wan YQ, Wang Y, Liu ZM, Qu X, Han BX, Bei JZ, Wang SG. Adhesion and proliferation of OCT-1 osteoblast-like cells on micro- and nano-scale topography structured pply(L-lactide). Biomaterials 2005;26(21):4453-4459.

49. Shin H, Jo S, Mikos AG. Biomimetic materials for tissue engineering. Biomaterials 2003;24(24):4353-64.
50. Cancedda R, Giannoni P, Mastrogiacomo M. A tissue engineering approach to bone repair in large animal models and in clinical practice. Biomaterials 2007;28(29):4240-50.
51. Arinzeh TL. Mesenchymal stem cells for bone repair: preclinical studies and potential orthopedic applications. Foot Ankle Clin 2005;10(4):651-65, viii.
52. Cancedda R, Mastrogiacomo M, Bianchi G, Derubeis A, Muraglia A, Quarto R. Bone marrow stromal cells and their use in regenerating bone. Novartis Found Symp 2003;249:133-43; discussion 143-7, 170-4, 239-41.
53. Caplan AI. Adult mesenchymal stem cells for tissue engineering versus regenerative medicine. J Cell Physiol 2007;213(2):341-7.
54. Pountos I, Giannoudis PV. Biology of mesenchymal stem cells. Injury 2005;36 Suppl 3:S8-S12.
55. Miura M, Miura Y, Sonoyama W, Yamaza T, Gronthos S, Shi S. Bone marrow-derived mesenchymal stem cells for regenerative medicine in craniofacial region. Oral Dis 2006;12(6):514-22.
56. De Vos J, Assou S, Tondeur S, Dijon M, Hamamah S. [Human embryonic stem cells: from the human embryo transgressed to the regenerative medicine of tomorrow]. Gynecol Obstet Fertil 2009;37(7-8):620-6.
57. Noel D, Djouad F, Jorgense C. Regenerative medicine through mesenchymal stem cells for bone and cartilage repair. Curr Opin Investig Drugs 2002;3(7):1000-4.
58. Pelled G, G T, Aslan H, Gazit Z, Gazit D. Mesenchymal stem cells for bone gene therapy and tissue engineering. Curr Pharm Des 2002;8(21):1917-28.
59. Ringe J, Haupl T, Sittinger M. [Mesenchymal stem cells for tissue engineering of bone and cartilage]. Med Klin (Munich) 2003;98 Suppl 2:35-40.
60. Schieker M, Seitz S, Gulkan H, Nentwich M, Horvath G, Regauer M, Milz S, Mutschler W. [Tissue engineering of bone. Integration and migration of human mesenchymal stem cells in colonized contructs in a murine model]. Orthopade 2004;33(12):1354-60.
61. Constantinescu D, Gray HL, Sammak PJ, Schatten GP, Csoka AB. Lamin A/C expression is a marker of mouse and human embryonic stem cell differentiation. Stem Cells 2006;24(1):177-85.
62. Tuan RS, Boland G, Tuli R. Adult mesenchymal stem cells and cell-based tissue engineering. Arthritis Res Ther 2003;5(1):32-45.
63. Xynos ID, Hukkanen MV, Batten JJ, Buttery LD, Hench LL, Polak JM. Bioglass 45S5 stimulates osteoblast turnover and enhances bone formation In vitro: implications and applications for bone tissue engineering. Calcif Tissue Int 2000;67(4):321-9.
64. Hong F, Fang F, He X, Cao X, Chipperfield H, Xie D, Wong WH, Ng HH, Zhong S. Dissecting early differentially expressed genes in a mixture of

differentiating embryonic stem cells. PLoS Comput Biol 2009;5(12):e1000607.
65. Holy CE, Shoichet MS, Davies JE. Engineering three-dimensional bone tissue in vitro using biodegradable scaffolds: investigating initial cell-seeding density and culture period. J Biomed Mater Res 2000;51(3):376-82.
66. Petrakova KV, Tolmacheva AA, AIa F. [Bone Formation Occurring in Bone Marrow Transplantation in Diffusion Chambers.]. Biull Eksp Biol Med 1963;56:87-91.
67. Friedenstein AJ, Chailakhyan RK, UV G. Bone marrow osteogenic stem cells: in vitro cultivation and transplantation in diffusion chambers. Cell Tissue Kinet. 1987;20(3):263-72.
68. Caplan AI. Mesenchymal stem cells. J Orthop Res 1991;9(5):641-50.
69. Caplan AI. The mesengenic process. Clin Plast Surg 1994;21(3):429-35.
70. Temenoff JS, Mikos AG. Injectable biodegradable materials for orthopedic tissue engineering. Biomaterials 2000;21(23):2405-12.
71. Boo JS, Yamada Y, Okazaki Y, Hibino Y, Okada K, Hata K, Yoshikawa T, Sugiura Y, Ueda M. Tissue-engineered bone using mesenchymal stem cells and a biodegradable scaffold. J Craniofac Surg 2002;13(2):231-9; discussion 240-3.
72. Crane GM, Ishaug SL, Mikos AG. Bone tissue engineering. Nat Med 1995;1(12):1322-4.
73. Holtorf HL, Jansen JA, Mikos AG. Modulation of cell differentiation in bone tissue engineering constructs cultured in a bioreactor. Adv Exp Med Biol 2006;585:225-41.
74. Funes JM, Quintero M, Henderson S, Martinez D, Qureshi U, Westwood C, Clements MO, Bourboulia D, Pedley RB, Moncada S and others. Transformation of human mesenchymal stem cells increases their dependency on oxidative phosphorylation for energy production. Proc Natl Acad Sci U S A 2007;104(15):6223-8.
75. Gou S, Wang C, Liu T, Wu H, Xiong J, Zhou F, Zhao G. Spontaneous differentiation of murine bone marrow-derived mesenchymal stem cells into adipocytes without malignant transformation after long-term culture. Cells Tissues Organs;191(3):185-92.
76. Popov BV, Petrov NS, Mikhailov VM, Tomilin AN, Alekseenko LL, Grinchuk TM, Zaichik AM. [Spontaneous transformation and immortalization of mesenchymal stem cells in vitro]. Tsitologiia 2009;51(2):91-102.
77. Rosland GV, Svendsen A, Torsvik A, Sobala E, McCormack E, Immervoll H, Mysliwietz J, Tonn JC, Goldbrunner R, Lonning PE and others. Long-term cultures of bone marrow-derived human mesenchymal stem cells frequently undergo spontaneous malignant transformation. Cancer Res 2009;69(13):5331-9.
78. Shima Y, Okamoto T, Aoyama T, Yasura K, Ishibe T, Nishijo K, Shibata KR, Kohno Y, Fukiage K, Otsuka S and others. In vitro transformation of

mesenchymal stem cells by oncogenic H-rasVal12. Biochem Biophys Res Commun 2007;353(1):60-6.
79. Wild L, Funes JM, Boshoff C, Flanagan JM. In Vitro Transformation of Mesenchymal Stem Cells Induces Gradual Genomic Hypomethylation. Carcinogenesis.
80. Balzer BL, Weiss SW. Do biomaterials cause implant-associated mesenchymal tumors of the breast? Analysis of 8 new cases and review of the literature. Hum Pathol 2009;40(11):1564-70.
81. Kirkpatrick CJ, Alves A, Kohler H, Kriegsmann J, Bittinger F, Otto M, Williams DF, Eloy R. Biomaterial-induced sarcoma: A novel model to study preneoplastic change. Am J Pathol 2000;156(4):1455-67.
82. Valko M, Rhodes CJ, Moncol J, Izakovic M, Mazur M. Free radicals, metals and antioxidants in oxidative stress-induced cancer. Chem Biol Interact 2006;160(1):1-40.
83. Lu H, Shi X, Costa M, Huang C. Carcinogenic effect of nickel compounds. Mol Cell Biochem 2005;279(1-2):45-67.
84. Leonard SS, Harris GK, Shi X. Metal-induced oxidative stress and signal transduction. Free Radic Biol Med 2004;37(12):1921-42.
85. Storz P. Mitochondrial ROS--radical detoxification, mediated by protein kinase D. Trends Cell Biol 2007;17(1):13-8.
86. Fruehauf JP, Meyskens FL, Jr. Reactive oxygen species: a breath of life or death? Clin Cancer Res 2007;13(3):789-94.
87. Stevens MM, George JH. Exploring and engineering the cell surface interface. Science 2005;310(5751):1135-8.
88. Ratner BD, Bryant SJ. Biomaterials: where we have been and where we are going. Annu Rev Biomed Eng 2004;6:41-75.
89. Charest JL, Eliason MT, Garcia AJ, King WP. Combined microscale mechanical topography and chemical patterns on polymer cell culture substrates. Biomaterials 2006;27(11):2487-94.
90. Dadsetan M, Jones JA, Hiltner A, Anderson JM. Surface chemistry mediates adhesive structure, cytoskeletal organization, and fusion of macrophages. J Biomed Mater Res A 2004;71(3):439-48.
91. Tziampazis E, Kohn J, Moghe PV. PEG-variant biomaterials as selectively adhesive protein templates: model surfaces for controlled cell adhesion and migration. Biomaterials 2000;21(5):511-20.
92. Brocchini S. Combinatorial chemistry and biomedical polymer development. Adv Drug Deliv Rev 2001;53(1):123-30.
93. Weber N, Bolikal D, Bourke SL, Kohn J. Small changes in the polymer structure influence the adsorption behavior of fibrinogen on polymer surfaces: validation of a new rapid screening technique. J Biomed Mater Res A 2004;68(3):496-503.
94. Meier MAR, Schubert US. Selected successful approaches in combinatorial materials research. Soft Matter 2006;2(5):371-376.
95. Hubbell JA. Biomaterials science and high-throughput screening. Nat Biotechnol 2004;22(7):828-9.

96. Abramson SD, Alexe G, Hammer PL, Kohn J. A computational approach to predicting cell growth on polymeric biomaterials. J Biomed Mater Res A 2005;73(1):116-24.
97. Brocchini S, James K, Tangpasuthadol V, Kohn J. Structure-property correlations in a combinatorial library of degradable biomaterials. Journal of Biomedical Materials Research 1998;42(1):66-75.
98. Meredith JC, Sormana JL, Keselowsky BG, Garcia AJ, Tona A, Karim A, Amis EJ. Combinatorial characterization of cell interactions with polymer surfaces. J Biomed Mater Res A 2003;66(3):483-90.
99. Schubert US, Amis EJ. Combinatorial and High-Throughput Approaches in Polymer and Materials Science: Hype or Real Paradigm Shift? Macromolecular Rapid Communications 2004;25(1):19.
100. Bailey LO, Becker ML, Stephens JS, Gallant ND, Mahoney CM, Washburn NR, Rege A, Kohn J, Amis EJ. Cellular response to phase-separated blends of tyrosine-derived polycarbonates. J Biomed Mater Res A 2006;76(3):491-502.
101. Sung HJ, Su J, Berglund JD, Russ BV, Meredith JC, Galis ZS. The use of temperature-composition combinatorial libraries to study the effects of biodegradable polymer blend surfaces on vascular cells. Biomaterials 2005;26(22):4557-67.
102. Zapata P, Su J, Garcia AJ, Meredith JC. Quantitative high-throughput screening of osteoblast attachment, spreading, and proliferation on demixed polymer blend micropatterns. Biomacromolecules 2007;8(6):1907-17.
103. Washburn NR, Simon CG, Weir MD, Bailey LO, Kennedy SB, Amis EJ. Combinatorial screen of cell-material interactions. Abstracts of Papers of the American Chemical Society 2004;227:U557-U557.
104. Hwang YS, Polak JM, Mantalaris A. In vitro direct osteogenesis of murine embryonic stem cells without embryoid body formation. Stem Cells Dev 2008;17(5):963-70.
105. Lin-Gibson S, Landis FA, Drzal PL. Combinatorial investigation of the structure-properties characterization of photopolymerized dimethacrylate networks. Biomaterials 2006;27(9):1711-7.
106. Becker ML, Bailey LO, Stephens LS, Rege A, Kohn J, Amis EJ. Cellular response to phase-separated blends of tyrosine-derived polycarbonates. Abstracts of Papers of the American Chemical Society 2005;230:U3786-U3786.
107. Wang YJ, Zhao Y, Meredith J, Phillips JE, Theilmann DA, Brock HW. Mutational analysis of the C-terminus in ion transport peptide (ITP) expressed in Drosophila Kc1 cells. Arch Insect Biochem Physiol 2000;45(3):129-38.
108. Bickle M. The beautiful cell: high-content screening in drug discovery. Anal Bioanal Chem.
109. Bickle M. High-content screening: a new primary screening tool? IDrugs 2008;11(11):822-6.

110. Zanella F, Lorens JB, Link W. High content screening: seeing is believing. Trends Biotechnol;28(5):237-45.
111. Abraham VC, Taylor DL, Haskins JR. High content screening applied to large-scale cell biology. Trends Biotechnol 2004;22(1):15-22.
112. Thomas N. High-content screening: a decade of evolution. J Biomol Screen;15(1):1-9.
113. Conrad C, Gerlich DW. Automated microscopy for high-content RNAi screening. J Cell Biol;188(4):453-61.
114. Naumann U, Wand MP. Automation in high-content flow cytometry screening. Cytometry A 2009;75(9):789-97.
115. Niederlein A, Meyenhofer F, White D, Bickle M. Image analysis in high-content screening. Comb Chem High Throughput Screen 2009;12(9):899-907.
116. Donaldson LA, Lausberg MJF. Comparison of conventional transmitted light and confocal microscopy for measuring wood cell dimensions by image analysis. Iawa Journal 1998;19(3):321-336.
117. Morishige N, Seki K, Chikama TI, Nishida T. Comparison between confocal microscopy and light microscopy for histopathologic observation of the corneal lesions associated with luetic interstitial keratitis. Investigative Ophthalmology & Visual Science 2003;44:U297-U297.
118. Szaflik JP. Comparison of in vivo confocal microscopy of human cornea by white light scanning slit and laser scanning systems. Cornea 2007;26(4):438-445.
119. Boyde A, Haroon Y, Jones SJ, Riggs CM. Three dimensional structure of the distal condyles of the third metacarpal bone of the horse. Equine Vet J 1999;31(2):122-9.
120. Chang CC, Lieberman SM, Moghe PV. Leukocyte spreading behavior on vascular biomaterial surfaces: consequences of chemoattractant stimulation. Biomaterials 1999;20(3):273-281.
121. Deng X, Gan X, Gu M. Monte Carlo simulation of multiphoton fluorescence microscopic imaging through inhomogeneous tissuelike turbid media. J Biomed Opt 2003;8(3):440-9.
122. Liu E, Treiser MD, Johnson PA, Patel P, Rege A, Kohn J, Moghe PV. Quantitative biorelevant profiling of material microstructure within 3D porous scaffolds via multiphoton fluorescence microscopy. J Biomed Mater Res B Appl Biomater 2007;82(2):284-97.
123. Shah AK, Sinha RK, Hickok NJ, Tuan RS. High-resolution morphometric analysis of human osteoblastic cell adhesion on clinically relevant orthopedic alloys. Bone 1999;24(5):499-506.
124. Anselme K, Bigerelle M, Noel B, Dufresne E, Judas D, Iost A, Hardouin P. Qualitative and quantitative study of human osteoblast adhesion on materials with various surface roughnesses. J Biomed Mater Res 2000;49(2):155-66.
125. Dalby MJ, Riehle MO, Johnstone HJ, Affrossman S, Curtis AS. Polymer-demixed nanotopography: control of fibroblast spreading and proliferation. Tissue Eng 2002;8(6):1099-108.

126. Kapur R, Rudolph AS. Cellular and cytoskeleton morphology and strength of adhesion of cells on self-assembled monolayers of organosilanes. Exp Cell Res 1998;244(1):275-85.
127. Kato S, Kidoaki S, Matsuda T. Substrate-dependent cellular behavior of Swiss 3T3 fibroblasts and activation of Rho family during adhesion and spreading processes. J Biomed Mater Res A 2004;68(2):314-24.
128. Perlman ZE, Slack MD, Feng Y, Mitchison TJ, Wu LF, Altschuler SJ. Multidimensional drug profiling by automated microscopy. Science 2004;306(5699):1194-8.
129. Price JH, Goodacre A, Hahn K, Hodgson L, Hunter EA, Krajewski S, Murphy RF, Rabinovich A, Reed JC, Heynen S. Advances in molecular labeling, high throughput imaging and machine intelligence portend powerful functional cellular biochemistry tools. J Cell Biochem Suppl 2002;39:194-210.
130. Tanaka M, Bateman R, Rauh D, Vaisberg E, Ramachandani S, Zhang C, Hansen KC, Burlingame AL, Trautman JK, Shokat KM and others. An unbiased cell morphology-based screen for new, biologically active small molecules. PLoS Biol 2005;3(5):e128.
131. Abad PC, Lewis J, Mian IS, Knowles DW, Sturgis J, Badve S, Xie J, Lelievre SA. NuMA influences higher order chromatin organization in human mammary epithelium. Mol Biol Cell 2007;18(2):348-61.
132. Boyan BD, Bonewald LF, Paschalis EP, Lohmann CH, Rosser J, Cochran DL, Dean DD, Schwartz Z, Boskey AL. Osteoblast-mediated mineral deposition in culture is dependent on surface microtopography. Calcif Tissue Int 2002;71(6):519-29.
133. Fu WY, Lu YM, Piao YJ. Differentiation and telomerase activity of human mesenchymal stem cells. Di Yi Jun Yi Da Xue Xue Bao 2001;21(11):801-805.
134. Kawaguchi J, Mee PJ, Smith AG. Osteogenic and chondrogenic differentiation of embryonic stem cells in response to specific growth factors. Bone 2005;36(5):758-69.
135. Lelievre S, Weaver VM, Bissell MJ. Extracellular matrix signaling from the cellular membrane skeleton to the nuclear skeleton: a model of gene regulation. Recent Prog Horm Res 1996;51:417-32.
136. Lelievre SA. Contributions of extracellular matrix signaling and tissue architecture to nuclear mechanisms and spatial organization of gene expression control. Biochim Biophys Acta 2009;1790(9):925-35.
137. Lukashev ME, Werb Z. ECM signalling: orchestrating cell behaviour and misbehaviour. Trends Cell Biol 1998;8(11):437-41.
138. McBeath R, Pirone DM, Nelson CM, Bhadriraju K, Chen CS. Cell shape, cytoskeletal tension, and RhoA regulate stem cell lineage commitment. Dev Cell 2004;6(4):483-95.
139. Rodriguez JP, Gonzalez M, Rios S, Cambiazo V. Cytoskeletal organization of human mesenchymal stem cells (MSC) changes during their osteogenic differentiation. J Cell Biochem 2004;93(4):721-31.

140. Cusmano L. The significance of the nuclear structure in the vaginal secretion cells as a means for cancer diagnosis. Am J Obstet Gynecol 1949;57(2):411.
141. Kortenhorst MS, Isharwal S, van Diest PJ, Chowdhury WH, Marlow C, Carducci MA, Rodriguez R, Veltri RW. Valproic acid causes dose- and time-dependent changes in nuclear structure in prostate cancer cells in vitro and in vivo. Mol Cancer Ther 2009;8(4):802-8.
142. Zink D, Fischer AH, Nickerson JA. Nuclear structure in cancer cells. Nat Rev Cancer 2004;4(9):677-87.
143. Mansergh FC, Daly CS, Hurley AL, Wride MA, Hunter SM, Evans MJ. Gene expression profiles during early differentiation of mouse embryonic stem cells. BMC Dev Biol 2009;9:5.
144. Handwerger S, Aronow B. Dynamic changes in gene expression during human trophoblast differentiation. Recent Prog Horm Res 2003;58:263-81.
145. Milioni D, Sado PE, Stacey NJ, Roberts K, McCann MC. Early gene expression associated with the commitment and differentiation of a plant tracheary element is revealed by cDNA-amplified fragment length polymorphism analysis. Plant Cell 2002;14(11):2813-24.
146. Huang H, Starodub O, McIntosh A, Kier AB, Schroeder F. Liver fatty acid-binding protein targets fatty acids to the nucleus. Real time confocal and multiphoton fluorescence imaging in living cells. J Biol Chem 2002;277(32):29139-51.
147. Juliano RL. Signal transduction by cell adhesion receptors and the cytoskeleton: functions of integrins, cadherins, selectins, and immunoglobulin-superfamily members. Annu Rev Pharmacol Toxicol 2002;42:283-323.
148. Lelievre SA, Weaver VM, Nickerson JA, Larabell CA, Bhaumik A, Petersen OW, Bissell MJ. Tissue phenotype depends on reciprocal interactions between the extracellular matrix and the structural organization of the nucleus. Proc Natl Acad Sci U S A 1998;95(25):14711-6.
149. Lelievre SA, Bissell MJ, Pujuguet P. Cell nucleus in context. Crit Rev Eukaryot Gene Expr 2000;10(1):13-20.
150. Mammoto A, Huang S, Moore K, Oh P, Ingber DE. Role of RhoA, mDia, and ROCK in cell shape-dependent control of the Skp2-p27kip1 pathway and the G1/S transition. J Biol Chem 2004;279(25):26323-30.
151. Nobes CD, Hall A. Rho, rac, and cdc42 GTPases regulate the assembly of multimolecular focal complexes associated with actin stress fibers, lamellipodia, and filopodia. Cell 1995;81(1):53-62.
152. Gieni RS, Hendzel MJ. Mechanotransduction from the ECM to the genome: are the pieces now in place? J Cell Biochem 2008;104(6):1964-87.
153. Sikavitsas VI, Temenoff JS, Mikos AG. Biomaterials and bone mechanotransduction. Biomaterials 2001;22(19):2581-93.

154. Warren DT, Zhang Q, Weissberg PL, Shanahan CM. Nesprins: intracellular scaffolds that maintain cell architecture and coordinate cell function? Expert Rev Mol Med 2005;7(11):1-15.
155. Wilhelmsen K, Litjens SH, Kuikman I, Tshimbalanga N, Janssen H, van den Bout I, Raymond K, Sonnenberg A. Nesprin-3, a novel outer nuclear membrane protein, associates with the cytoskeletal linker protein plectin. J Cell Biol 2005;171(5):799-810.
156. Akhtar A, Gasser SM. The nuclear envelope and transcriptional control. Nat Rev Genet 2007;8(7):507-17.
157. McDonald D, Carrero G, Andrin C, de Vries G, Hendzel MJ. Nucleoplasmic beta-actin exists in a dynamic equilibrium between low-mobility polymeric species and rapidly diffusing populations. J Cell Biol 2006;172(4):541-52.
158. Antoniou M, Carmo-Fonseca M, Ferreira J, Lamond AI. Nuclear organization of splicing snRNPs during differentiation of murine erythroleukemia cells in vitro. J Cell Biol 1993;123(5):1055-68.
159. Bissell MJ, Weaver VM, Lelievre SA, Wang F, Petersen OW, Schmeichel KL. Tissue structure, nuclear organization, and gene expression in normal and malignant breast. Cancer Res 1999;59(7 Suppl):1757-1763s; discussion 1763s-1764s.
160. Dillon N, Festenstein R. Unravelling heterochromatin: competition between positive and negative factors regulates accessibility. Trends Genet 2002;18(5):252-8.
161. Krystosek A, Puck TT. The spatial distribution of exposed nuclear DNA in normal, cancer, and reverse-transformed cells. Proc Natl Acad Sci U S A 1990;87(17):6560-4.
162. Olson MO, Hingorani K, Szebeni A. Conventional and nonconventional roles of the nucleolus. Int Rev Cytol 2002;219:199-266.
163. Pajerowski JD, Dahl KN, Zhong FL, Sammak PJ, Discher DE. Physical plasticity of the nucleus in stem cell differentiation. Proc Natl Acad Sci U S A 2007;104(40):15619-24.
164. Gribbon C, Dahm R, Prescott AR, Quinlan RA. Association of the nuclear matrix component NuMA with the Cajal body and nuclear speckle compartments during transitions in transcriptional activity in lens cell differentiation. Eur J Cell Biol 2002;81(10):557-66.
165. Chandramouly G, Abad PC, Knowles DW, Lelievre SA. The control of tissue architecture over nuclear organization is crucial for epithelial cell fate. J Cell Sci 2007;120(Pt 9):1596-606.
166. Kaminker P, Plachot C, Kim SH, Chung P, Crippen D, Petersen OW, Bissell MJ, Campisi J, Lelievre SA. Higher-order nuclear organization in growth arrest of human mammary epithelial cells: a novel role for telomere-associated protein TIN2. J Cell Sci 2005;118(Pt 6):1321-30.
167. Long F, Peng H, Sudar D, Lelievre SA, Knowles DW. Phenotype clustering of breast epithelial cells in confocal images based on nuclear protein distribution analysis. BMC Cell Biol 2007;8 Suppl 1:S3.

168. Bacakova L, Filova E, Rypacek F, Svorcik V, Stary V. Cell adhesion on artificial materials for tissue engineering. Physiol Res 2004;53 Suppl 1:S35-45.
169. De Deyne PG, Kladakis SM. Bioscaffolds in tissue engineering: a rationale for use in the reconstruction of musculoskeletal soft tissues. Clin Podiatr Med Surg North Am 2005;22(4):521-32, v.
170. Hammond JS, Beckingham IJ, Shakesheff KM. Scaffolds for liver tissue engineering. Expert Rev Med Devices 2006;3(1):21-7.
171. Hollister SJ. Porous scaffold design for tissue engineering. Nat Mater 2005;4(7):518-24.
172. Wu L, Zhang H, Zhang J, Ding J. Fabrication of three-dimensional porous scaffolds of complicated shape for tissue engineering. I. Compression molding based on flexible-rigid combined mold. Tissue Eng 2005;11(7-8):1105-14.
173. Yoshikawa H, Myoui A. Bone tissue engineering with porous hydroxyapatite ceramics. J Artif Organs 2005;8(3):131-6.
174. Sachlos E, Czernuszka JT. Making tissue engineering scaffolds work. Review: the application of solid freeform fabrication technology to the production of tissue engineering scaffolds. Eur Cell Mater 2003;5:29-39; discussion 39-40.
175. Mikos AG, Thorsen AJ, Czerwonka LA, Bao Y, R L. preparation and characterisation of poly(L-lactic acide) foams. Polymer 1994(35):1068-1077.
176. Mooney DJ, Baldwin DF, Suh NP, Vacanti JP, Langer R. Novel approach to fabricate porous sponges of poly(D,L-lactic-co-glycolic acid) without the use of organic solvents. Biomaterials 1996;17(14):1417-22.
177. Mikos AG, Bao Y, Cima LG, Ingber DE, Vacanti JP, Langer R. Preparation of poly(glycolic acid) bonded fiber structures for cell attachment and transplantation. J Biomed Mater Res 1993;27(2):183-9.
178. Lo H, Ponticiello MS, KW L. Fabrication of controlled release biodegreadable foams by phase seperation. Tissue Eng 1995(1):15-28.
179. Thomson RC, Yaszemski MJ, Powers JM, Mikos AG. Fabrication of biodegradable polymer scaffolds to engineer trabecular bone. J Biomater Sci Polym Ed 1995;7(1):23-38.
180. Whang K, Thomas C.K, Nuber G, KE H. A novel method to fabricate bioabsorbable scaffolds. Polymer 1995;36(4):837-842.
181. Schmitz JP, Hollinger JO. A preliminary study of the osteogenic potential of a biodegradable alloplastic-osteoinductive alloimplant. Clin Orthop Relat Res 1988(237):245-55.
182. Lin CY, Kikuchi N, Hollister SJ. A novel method for biomaterial scaffold internal architecture design to match bone elastic properties with desired porosity. J Biomech 2004;37(5):623-36.
183. Knackstedt MA, Arns CH, Senden TJ, Gross K. Structure and properties of clinical coralline implants measured via 3D imaging and analysis. Biomaterials 2006;27(13):2776-86.

184. Ho ST, Hutmacher DW. A comparison of micro CT with other techniques used in the characterization of scaffolds. Biomaterials 2006;27(8):1362-76.
185. Mariani M, Rosatini F, Vozzi G, Previti A, Ahluwalia A. Characterization of Tissue-Engineered Scaffolds Microfabricated with PAM. Tissue Eng 2006.
186. Safinia L, Mantalaris A, Bismarck A. Nondestructive technique for the characterization of the pore size distribution of soft porous constructs for tissue engineering. Langmuir 2006;22(7):3235-42.
187. Cho SH, Oh SH, Lee JH. Fabrication and characterization of porous alginate/polyvinyl alcohol hybrid scaffolds for 3D cell culture. J Biomater Sci Polym Ed 2005;16(8):933-47.
188. Thurner P, Muller R, Raeber G, Sennhauser U, Hubbell JA. 3D morphology of cell cultures: a quantitative approach using micrometer synchrotron light tomography. Microsc Res Tech 2005;66(6):289-98.
189. Guan J, Fujimoto KL, Sacks MS, Wagner WR. Preparation and characterization of highly porous, biodegradable polyurethane scaffolds for soft tissue applications. Biomaterials 2005;26(18):3961-71.
190. Liu TT, Kishimoto T, Hatakeyama H, Nemoto T, Takahashi N, Kasai H. Exocytosis and endocytosis of small vesicles in PC12 cells studied with TEPIQ (two-photon extracellular polar-tracer imaging-based quantification) analysis. J Physiol 2005;568(Pt 3):917-29.
191. Cicerone MT, Dunkers JP, Washburn NR, Landis FA, Cooper JA. Optical Coherence Microscopy for In-situ Monitoring of Cell Growth in Scaffold Constructs. Proceedings of the 7th World Biomaterials Congress. Sidney, Australia. 2004:584.
192. Dunkers JD, Cicerone MT, Washburn NR. Collinear Optical Coherence and Confocal Fluorescence Microscopies for Tissue Engineering. Optics Express 2003;11(23):3074-3079.
193. Dunkers JP, Cicerone MT. Scaffold Structure and Cell Function Through Multimodal Imaging and Quantitative Visualization. Biomaterials Forum 2003;25(3):8.
194. Maspero FA, Ruffieux K, Muller B, Wintermantel E. Resorbable defect analog PLGA scaffolds using CO2 as solvent: structural characterization. J Biomed Mater Res 2002;62(1):89-98.
195. Sahoo SK, Panda AK, Labhasetwar V. Characterization of porous PLGA/PLA microparticles as a scaffold for three dimensional growth of breast cancer cells. Biomacromolecules 2005;6(2):1132-9.
196. Che S, Lund K, Tatsumi T, Iijima S, Joo SH, Ryoo R, Terasaki O. Direct observation of 3D mesoporous structure by scanning electron microscopy (SEM): SBA-15 silica and CMK-5 carbon. Angew Chem Int Ed Engl 2003;42(19):2182-5.
197. Blacher S, Maquet V, Schils F, Martin D, Schoenen J, Moonen G, Jerome R, Pirard JP. Image analysis of the axonal ingrowth into poly(D,L-lactide) porous scaffolds in relation to the 3-D porous structure. Biomaterials 2003;24(6):1033-40.

198. Tjia JS, Moghe PV. Analysis of 3-D microstructure of porous poly(lactide-glycolide) matrices using confocal microscopy. J Biomed Mater Res 1998;43(3):291-9.
199. Casper CL, Yamaguchi N, Kiick KL, Rabolt JF. Functionalizing electrospun fibers with biologically relevant macromolecules. Biomacromolecules 2005;6(4):1998-2007.
200. Gossl M, Bentley MD, Lerman LO. Review - 3D Micro CT Imaging of Renal Micro-Structural Changes. Nephron Clin Pract 2006;103(2):c66-70.
201. Rajagopalan S, Lu L, Yaszemski MJ, Robb RA. Optimal segmentation of microcomputed tomographic images of porous tissue-engineering scaffolds. J Biomed Mater Res A 2005;75(4):877-87.
202. Gauthier O, Muller R, von Stechow D, Lamy B, Weiss P, Bouler JM, Aguado E, Daculsi G. In vivo bone regeneration with injectable calcium phosphate biomaterial: a three-dimensional micro-computed tomographic, biomechanical and SEM study. Biomaterials 2005;26(27):5444-53.
203. De Graef B, Cnudde V, Dick J, De Belie N, Jacobs P, Verstraete W. A sensitivity study for the visualisation of bacterial weathering of concrete and stone with computerised X-ray microtomography. Sci Total Environ 2005;341(1-3):173-83.
204. Jiang Y, Zhao J, White DL, Genant HK. Micro CT and Micro MR imaging of 3D architecture of animal skeleton. J Musculoskelet Neuronal Interact 2000;1(1):45-51.
205. Shimko DA, Shimko VF, Sander EA, Dickson KF, Nauman EA. Effect of porosity on the fluid flow characteristics and mechanical properties of tantalum scaffolds. J Biomed Mater Res B Appl Biomater 2005;73(2):315-24.
206. Lin AS, Barrows TH, Cartmell SH, Guldberg RE. Microarchitectural and mechanical characterization of oriented porous polymer scaffolds. Biomaterials 2003;24(3):481-9.
207. Cartmell S, Huynh K, Lin A, Nagaraja S, Guldberg R. Quantitative microcomputed tomography analysis of mineralization within three-dimensional scaffolds in vitro. J Biomed Mater Res A 2004;69(1):97-104.
208. Dunkers JP, Sanders, D. P., Hunston, D. L., Everett, M. J., and Green, W. H. Comparison of Optical Coherence Tomography, X-Ray Computed Tomography, and Confocal Microscopy Results From an Impact Damaged Epoxy/E-Glass Composite. Journal of Adhesion 2002;78(2):129-154.
209. Chu TM, Hollister SJ, Halloran JW, Feinberg SE, Orton DG. Manufacturing and characterization of 3-d hydroxyapatite bone tissue engineering scaffolds. Ann N Y Acad Sci 2002;961:114-7.
210. Chu CR, Monosov AZ, Amiel D. In situ assessment of cell viability within biodegradable polylactic acid polymer matrices. Biomaterials 1995;16(18):1381-4.
211. Jones CW, Smolinski D, Keogh A, Kirk TB, Zheng MH. Confocal laser scanning microscopy in orthopaedic research. Prog Histochem Cytochem 2005;40(1):1-71.

212. Halbhuber KJ, Konig K. Modern laser scanning microscopy in biology, biotechnology and medicine. Ann Anat 2003;185(1):1-20.
213. Rodriguez A, Ehlenberger D, Kelliher K, Einstein M, Henderson SC, Morrison JH, Hof PR, Wearne SL. Automated reconstruction of three-dimensional neuronal morphology from laser scanning microscopy images. Methods 2003;30(1):94-105.
214. Masters BR, So PT, Kim KH, Buehler C, Gratton E. Multiphoton excitation microscopy, confocal microscopy, and spectroscopy of living cells and tissues; functional metabolic imaging of human skin in vivo. Methods Enzymol 1999;307:513-36.
215. Masters BR, So PT, Gratton E. Multiphoton excitation microscopy of in vivo human skin. Functional and morphological optical biopsy based on three-dimensional imaging, lifetime measurements and fluorescence spectroscopy. Ann N Y Acad Sci 1998;838:58-67.
216. Emptage NJ. Fluorescent imaging in living systems. Curr Opin Pharmacol 2001;1(5):521-5.
217. Gustafsson MG. Extended resolution fluorescence microscopy. Curr Opin Struct Biol 1999;9(5):627-34.
218. Piston DW, Knobel SM. Quantitative imaging of metabolism by two-photon excitation microscopy. Methods Enzymol 1999;307:351-68.
219. Centonze VE, White JG. Multiphoton excitation provides optical sections from deeper within scattering specimens than confocal imaging. Biophys J 1998;75(4):2015-24.
220. Smith PJ, Blunt N, Wiltshire M, Hoy T, Teesdale-Spittle P, Craven MR, Watson JV, Amos WB, Errington RJ, Patterson LH. Characteristics of a novel deep red/infrared fluorescent cell-permeant DNA probe, DRAQ5, in intact human cells analyzed by flow cytometry, confocal and multiphoton microscopy. Cytometry 2000;40(4):280-91.
221. Zipfel WR, Williams RM, Christie R, Nikitin AY, Hyman BT, Webb WW. Live tissue intrinsic emission microscopy using multiphoton-excited native fluorescence and second harmonic generation. Proc Natl Acad Sci U S A 2003;100(12):7075-80.
222. Helmchen F, Denk W. New developments in multiphoton microscopy. Curr Opin Neurobiol 2002;12(5):593-601.
223. Williams RM, Zipfel WR, Webb WW. Multiphoton microscopy in biological research. Curr Opin Chem Biol 2001;5(5):603-8.
224. Gratton E, Barry NP, Beretta S, Celli A. Multiphoton fluorescence microscopy. Methods 2001;25(1):103-10.
225. Bourke SL, Kohn J. Polymers derived from the amino acid L-tyrosine: polycarbonates, polyarylates and copolymers with poly(ethylene glycol). Adv Drug Deliv Rev 2003;55(4):447-66.
226. Bourke SL, Kohn J, Dunn MG. Preliminary development of a novel resorbable synthetic polymer fiber scaffold for anterior cruciate ligament reconstruction. Tissue Eng 2004;10(1-2):43-52.

227. Yarlagadda PK, Chandrasekharan M, Shyan JY. Recent advances and current developments in tissue scaffolding. Biomed Mater Eng 2005;15(3):159-77.
228. Griffith LG, Naughton G. Tissue engineering--current challenges and expanding opportunities. Science 2002;295(5557):1009-14.
229. Zipfel WR, Williams RM, Webb WW. Nonlinear magic: multiphoton microscopy in the biosciences. Nat Biotechnol 2003;21(11):1369-77.
230. Korobkin DV, Yablonovitch E. Two fold spatial resolution enhancement by two-photon exposure of photographic film. Optical Engineering 2002;41(7):1729 -1732.
231. Schilders SP, Gu M. Limiting Factors on Image Quality in Imaging through Turbid Media under Single-photon and Two-photon Excitation. Microsc Microanal 2000;6(2):156-160.
232. Rubart M. Two-photon microscopy of cells and tissue. Circ Res 2004;95(12):1154-66.
233. Centonze VE. Introduction to multiphoton excitation imaging for the biological sciences. Methods Cell Biol 2002;70:129-48.
234. Periasamy A, Day RN. Visualizing protein interactions in living cells using digitized GFP imaging and FRET microscopy. Methods Cell Biol 1999;58:293-314.
235. Cavanaugh TJ, Nauman EB. Particulate growth in phase-separated polymer blends. Journal of Polymer Science Part B: Polymer Physics 1998;36(12):2191–2196.
236. Fortenly I, Zivny A, Juza J. Cosening of the phase structure in immiscible polymer blends. J Polym Sci. Part B: Polym Phys 1999;37:181-187.
237. Chen H, Nauman EB. Phase ripening in partculate binary polymer blends. J Polym Sci. Part B: Polym Phys 2004;42:603-612.
238. He Q, Nauman EB. On spinodal decomposition of binary polymer blends under shear flows. Chem Eng Sci. 1997;52:481-496.
239. Sadtler V, Imbert P, Dellacherie E. Ostwald ripening of oil-in-water emulsions stabilized by phenoxy-substituted dextrans. J Colloid Interface Sci 2002;254:355-361.
240. Hou Q, Grijpma DW, Feijen J. Preparation of interconnected highly porous polymeric structures by a replication and freeze-drying process. J Biomed Mater Res B Appl Biomater 2003;67(2):732-40.
241. Moore MJ, Jabbari E, Ritman EL, Lu L, Currier BL, Windebank AJ, Yaszemski MJ. Quantitative analysis of interconnectivity of porous biodegradable scaffolds with micro-computed tomography. J Biomed Mater Res A 2004;71(2):258-67.
242. Murphy WL, Dennis RG, Kileny JL, Mooney DJ. Salt fusion: an approach to improve pore interconnectivity within tissue engineering scaffolds. Tissue Eng 2002;8(1):43-52.
243. Hedberg EL, Kroese-Deutman HC, Shih CK, Lemoine JJ, Liebschner MA, Miller MJ, Yasko AW, Crowther RS, Carney DH, Mikos AG and others. Methods: a comparative analysis of radiography, microcomputed

tomography, and histology for bone tissue engineering. Tissue Eng 2005;11(9-10):1356-67.
244. Ranucci CS, Moghe PV. Substrate microtopography can enhance cell adhesive and migratory responsiveness to matrix ligand density. J Biomed Mater Res 2001;54(2):149-61.
245. Ranucci CS, Moghe PV. Polymer substrate topography actively regulates the multicellular organization and liver-specific functions of cultured hepatocytes. Tissue Eng 1999;5(5):407-20.
246. Min BM, Jeong L, Nam YS, Kim JM, Kim JY, Park WH. Formation of silk fibroin matrices with different texture and its cellular response to normal human keratinocytes. Int J Biol Macromol 2004;34(5):281-8.
247. Spiteri CG, Pilliar RM, Kandel RA. Substrate porosity enhances chondrocyte attachment, spreading, and cartilage tissue formation in vitro. J Biomed Mater Res A 2006;78(4):676-83.
248. Kohn J. New approaches to biomaterials design. Nat Mater 2004;3(11):745-7.
249. Becker ML. Combinatorial Biomaterials: opportunites beyond synthesis. Biomat Forum 2006;3:8-11.
250. Lin NJ, Drzal PL, Lin-Gibson S. Two-dimensional gradient platforms for rapid assessment of dental polymers: A chemical, mechanical and biological evaluation. Dent Mater 2007;23(10):1211-20.
251. Meredith JC, Smith AP, Karim A, Amis EJ. Combinatorial Materials Science for Polymer Thin-Film Dewetting. Macromolecules 2000;33(26):9747-9756.
252. Ertel SI, Kohn J. Evaluation of a series of tyrosine-derived polycarbonates as degradable biomaterials. J Biomed Mater Res 1994;28(8):919-30.
253. Stafford CM, Roskov KE, Epps TH, Fasolka MJ. Generating thickness gradient of thin polymer films via flow coating. Rev. Sci. Instrum. 2006;77(2):023908-7.
254. Anderson DG, Putnam D, Lavik EB, Mahmood TA, Langer R. Biomaterial microarrays: rapid, microscale screening of polymer-cell interaction. Biomaterials 2005;26(23):4892-7.
255. Washburn NR, Yamada KM, Simon CG, Jr., Kennedy SB, Amis EJ. High-throughput investigation of osteoblast response to polymer crystallinity: influence of nanometer-scale roughness on proliferation. Biomaterials 2004;25(7-8):1215-24.
256. Chan CM, Ko TM, Hiraoka H. Polymer surface modification by plasmas and photons. Surface Science Reports 1996;24(1/2):1-54.
257. Murthy NS, Prabhu RD, Martin JJ, Zhou L, Headrick RL. Self-assembled and etched cones on laser ablated polymer surfaces. Journal of Applied Physics 2006;100(2):023538/1-023538/12.
258. Marletta G, Ciapetti G, Satriano C, Perut F, Salerno M, Baldini N. Improved osteogenic differentiation of human marrow stromal cells cultured on ion-induced chemically structured poly-epsilon-caprolactone. Biomaterials 2007;28(6):1132-40.

259. James K, Levene H, Parsons JR, Kohn J. Small changes in polymer chemistry have a large effect on the bone-implant interface: evaluation of a series of degradable tyrosine-derived polycarbonates in bone defects. Biomaterials 1999;20(23-24):2203-12.
260. Simon CG, Jr., Eidelman N, Kennedy SB, Sehgal A, Khatri CA, Washburn NR. Combinatorial screening of cell proliferation on poly(L-lactic acid)/poly(D,L-lactic acid) blends. Biomaterials 2005;26(34):6906-15.
261. Wilson CJ, Clegg RE, Leavesley DI, Pearcy MJ. Mediation of biomaterial-cell interactions by adsorbed proteins: a review. Tissue Eng 2005;11(1-2):1-18.
262. Ryan PL, Foty RA, Kohn J, Steinberg MS. Tissue spreading on implantable substrates is a competitive outcome of cell-cell vs. cell-substratum adhesivity. Proc Natl Acad Sci U S A 2001;98(8):4323-7.
263. Deng Y, Lin XS, Zheng Z, Deng JG, Chen JC, Ma H, Chen GQ. Poly(hydroxybutyrate-co-hydroxyhexanoate) promoted production of extracellular matrix of articular cartilage chondrocytes in vitro. Biomaterials 2003;24(23):4273-81.
264. Wang YW, Wu Q, Chen GQ. Attachment, proliferation and differentiation of osteoblasts on random biopolyester poly(3-hydroxybutyrate-co-3-hydroxyhexanoate) scaffolds. Biomaterials 2004;25(4):669-75.
265. Foster R, Hu KQ, Lu Y, Nolan KM, Thissen J, Settleman J. Identification of a novel human Rho protein with unusual properties: GTPase deficiency and in vivo farnesylation. Mol Cell Biol 1996;16(6):2689-99.
266. Prendergast GC, Davide JP, deSolms SJ, Giuliani EA, Graham SL, Gibbs JB, Oliff A, Kohl NE. Farnesyltransferase inhibition causes morphological reversion of ras-transformed cells by a complex mechanism that involves regulation of the actin cytoskeleton. Mol Cell Biol 1994;14(6):4193-202.
267. Hall A. Rho GTPases and the actin cytoskeleton. Science 1998;279(5350):509-14.
268. Ridley AJ, Hall A. The small GTP-binding protein rho regulates the assembly of focal adhesions and actin stress fibers in response to growth factors. Cell 1992;70(3):389-99.
269. Chen CS, Mrksich M, Huang S, Whitesides GM, Ingber DE. Geometric control of cell life and death. Science 1997;276(5317):1425-8.
270. Huang S, Ingber DE. A discrete cell cycle checkpoint in late G(1) that is cytoskeleton-dependent and MAP kinase (Erk)-independent. Exp Cell Res 2002;275(2):255-64.
271. Delorme B, Charbord P. Culture and characterization of human bone marrow mesenchymal stem cells. Methods Mol Med 2007;140:67-81.
272. Jiang Y, Jahagirdar BN, Reinhardt RL, Schwartz RE, Keene CD, Ortiz-Gonzalez XR, Reyes M, Lenvik T, Lund T, Blackstad M and others. Pluripotency of mesenchymal stem cells derived from adult marrow. Nature 2002;418(6893):41-9.
273. Snykers S, Vanhaecke T, Papeleu P, Henkens T, Vinken M, Elaut G, Van Riet I, Rogiers V. In vitro multipotency of human bone marrow (mesenchymal) stem cells. ALTEX 2006;23 Suppl:400-5.

274. Pittenger MF, Mackay AM, Beck SC, Jaiswal RK, Douglas R, Mosca JD, Moorman MA, Simonetti DW, Craig S, Marshak DR. Multilineage potential of adult human mesenchymal stem cells. Science 1999;284(5411):143-7.
275. Curran JM, Chen R, Hunt JA. The guidance of human mesenchymal stem cell differentiation in vitro by controlled modifications to the cell substrate. Biomaterials 2006;27(27):4783-93.
276. Reilly GC, Engler AJ. Intrinsic extracellular matrix properties regulate stem cell differentiation. J Biomech 2010;43(1):55-62.
277. Treiser MD, Yang EH, Gordonov S, Cohen DM, Androulakis IP, Kohn J, Chen CS, Moghe PV. Cytoskeleton-based forecasting of stem cell lineage fates. Proc Natl Acad Sci U S A;107(2):610-5.
278. Compton DA, Cleveland DW. NuMA, a nuclear protein involved in mitosis and nuclear reformation. Curr Opin Cell Biol 1994;6(3):343-6.
279. He D, Zeng C, Brinkley BR. Nuclear matrix proteins as structural and functional components of the mitotic apparatus. Int Rev Cytol 1995;162B:1-74.
280. Mancini MA, He D, Ouspenski, II, Brinkley BR. Dynamic continuity of nuclear and mitotic matrix proteins in the cell cycle. J Cell Biochem 1996;62(2):158-64.
281. Tang TK, Tang CJ, Chao YJ, Wu CW. Nuclear mitotic apparatus protein (NuMA): spindle association, nuclear targeting and differential subcellular localization of various NuMA isoforms. J Cell Sci 1994;107 (Pt 6):1389-402.
282. Gama-Carvalho M, Carmo-Fonseca M. The rules and roles of nucleocytoplasmic shuttling proteins. FEBS Lett 2001;498(2-3):157-63.
283. Arnaout MA, Goodman SL, Xiong JP. Structure and mechanics of integrin-based cell adhesion. Curr Opin Cell Biol 2007;19(5):495-507.
284. El-Bahrawy M, Talbot I, Poulsom R, Alison M. Variable nuclear localization of alpha-catenin in colorectal carcinoma. Lab Invest 2002;82(9):1167-74.
285. Ingber D. How cells (might) sense microgravity. FASEB J 1999;13 Suppl:S3-15.
286. Ingber DE, Prusty D, Sun Z, Betensky H, Wang N. Cell shape, cytoskeletal mechanics, and cell cycle control in angiogenesis. J Biomech 1995;28(12):1471-84.
287. Radulescu AE, Cleveland DW. NuMA after 30 years: the matrix revisited. Trends Cell Biol;20(4):214-22.
288. D'Angelo MA, Hetzer MW. Structure, dynamics and function of nuclear pore complexes. Trends Cell Biol 2008;18(10):456-66.
289. Yasuhara N, Oka M, Yoneda Y. The role of the nuclear transport system in cell differentiation. Semin Cell Dev Biol 2009;20(5):590-9.
290. Vasu SK, Forbes DJ. Nuclear pores and nuclear assembly. Curr Opin Cell Biol 2001;13(3):363-75.
291. Azuma Y, Dasso M. The role of Ran in nuclear function. Curr Opin Cell Biol 2000;12(3):302-7.

292. Dechat T, Pfleghaar K, Sengupta K, Shimi T, Shumaker DK, Solimando L, Goldman RD. Nuclear lamins: major factors in the structural organization and function of the nucleus and chromatin. Genes Dev 2008;22(7):832-53.
293. Libotte T, Zaim H, Abraham S, Padmakumar VC, Schneider M, Lu W, Munck M, Hutchison C, Wehnert M, Fahrenkrog B and others. Lamin A/C-dependent localization of Nesprin-2, a giant scaffolder at the nuclear envelope. Mol Biol Cell 2005;16(7):3411-24.
294. Mislow JM, Holaska JM, Kim MS, Lee KK, Segura-Totten M, Wilson KL, McNally EM. Nesprin-1alpha self-associates and binds directly to emerin and lamin A in vitro. FEBS Lett 2002;525(1-3):135-40.
295. Krauss SW, Lo AJ, Short SA, Koury MJ, Mohandas N, Chasis JA. Nuclear substructure reorganization during late-stage erythropoiesis is selective and does not involve caspase cleavage of major nuclear substructural proteins. Blood 2005;106(6):2200-5.
296. Nielsen JA, Hudson LD, Armstrong RC. Nuclear organization in differentiating oligodendrocytes. J Cell Sci 2002;115(Pt 21):4071-9.
297. Kunzler TP, Drobek T, Schuler M, Spencer ND. Systematic study of osteoblast and fibroblast response to roughness by means of surface-morphology gradients. Biomaterials 2007;28(13):2175-82.
298. Feister HA, Onyia JE, Miles RR, Yang X, Galvin R, Hock JM, Bidwell JP. The expression of the nuclear matrix proteins NuMA, topoisomerase II-alpha, and -beta in bone and osseous cell culture: regulation by parathyroid hormone. Bone 2000;26(3):227-34.
299. Taimen P, Viljamaa M, Kallajoki M. Preferential expression of NuMA in the nuclei of proliferating cells. Exp Cell Res 2000;256(1):140-9.
300. Liu E, Treiser MD, Patel H, Sung HJ, Roskov KE, Kohn J, Becker ML, Moghe PV. High-content profiling of cell responsiveness to graded substrates based on combinyatorially variant polymers. Comb Chem High Throughput Screen 2009;12(7):646-55.
301. Liu E, Gordonov S, Treiser MD, Moghe PV. Parsing the early cytoskeletal and nuclear organizational cues that demarcate stem cell lineages. Cell Cycle;9(11).
302. Getzenberg RH, Pienta KJ, Ward WS, Coffey DS. Nuclear structure and the three-dimensional organization of DNA. J Cell Biochem 1991;47(4):289-99.
303. Li N, Yang R, Zhang W, Dorfman H, Rao P, Gorlick R. Genetically transforming human mesenchymal stem cells to sarcomas: changes in cellular phenotype and multilineage differentiation potential. Cancer 2009;115(20):4795-806.
304. Rani AS, Qu DQ, Sidhu MK, Panagakos F, Shah V, Klein KM, Brown N, Pathak S, Kumar S. Transformation of immortal, non-tumorigenic osteoblast-like human osteosarcoma cells to the tumorigenic phenotype by nickel sulfate. Carcinogenesis 1993;14(5):947-53.
305. Li JY, La XY, Luo Y, Sun J, Yu J, Lan JP, Zhu YY, Tan YM, Lin MF, Huang H. [Telomerase activity of human bone marrow mesenchymal stem cells]. Zhejiang Da Xue Xue Bao Yi Xue Ban 2004;33(6):481-5.

306. Greaves M. Is telomerase activity in cancer due to selection of stem cells and differentiation arrest? Trends Genet 1996;12(4):127-8.
307. Shay JW, Wright WE. Telomeres and telomerase in normal and cancer stem cells. FEBS Lett;584(17):3819-25.
308. Artandi SE, DePinho RA. Telomeres and telomerase in cancer. Carcinogenesis;31(1):9-18.
309. Behrend L, Henderson G, Zwacka RM. Reactive oxygen species in oncogenic transformation. Biochem Soc Trans 2003;31(Pt 6):1441-4.
310. Sung HJ, Chandra P, Treiser MD, Liu E, Iovine CP, Moghe PV, Kohn J. Synthetic polymeric substrates as potent pro-oxidant versus anti-oxidant regulators of cytoskeletal remodeling and cell apoptosis. J Cell Physiol 2009;218(3):549-57.
311. Torsvik A, Rosland GV, Svendsen A, Molven A, Immervoll H, McCormack E, Lonning PE, Primon M, Sobala E, Tonn JC and others. Spontaneous malignant transformation of human mesenchymal stem cells reflects cross-contamination: putting the research field on track - letter. Cancer Res;70(15):6393-6.
312. Liu C, Chen Z, Zhang T, Lu Y. Multiple tumor types may originate from bone marrow-derived cells. Neoplasia 2006;8(9):716-24.
313. Boeuf S, Kunz P, Hennig T, Lehner B, Hogendoorn P, Bovee J, Richter W. A chondrogenic gene expression signature in mesenchymal stem cells is a classifier of conventional central chondrosarcoma. J Pathol 2008;216(2):158-66.
314. Chamberlain G, Fox J, Ashton B, Middleton J. Concise review: mesenchymal stem cells: their phenotype, differentiation capacity, immunological features, and potential for homing. Stem Cells 2007;25(11):2739-49.
315. Hui JH, Ouyang HW, Hutmacher DW, Goh JC, Lee EH. Mesenchymal stem cells in musculoskeletal tissue engineering: a review of recent advances in National University of Singapore. Ann Acad Med Singapore 2005;34(2):206-12.
316. Jorgensen C, Gordeladze J, Noel D. Tissue engineering through autologous mesenchymal stem cells. Curr Opin Biotechnol 2004;15(5):406-10.
317. Kemp KC, Hows J, Donaldson C. Bone marrow-derived mesenchymal stem cells. Leuk Lymphoma 2005;46(11):1531-44.
318. Marie PJ, Fromigue O. Osteogenic differentiation of human marrow-derived mesenchymal stem cells. Regen Med 2006;1(4):539-48.
319. Mauney JR, Volloch V, Kaplan DL. Role of adult mesenchymal stem cells in bone tissue engineering applications: current status and future prospects. Tissue Eng 2005;11(5-6):787-802.
320. Mendes SC, Tibbe JM, Veenhof M, Bakker K, Both S, Platenburg PP, Oner FC, De Bruijn JD, Van Blitterswijk CA. Bone tissue-engineered implants using human bone marrow stromal cells: Effect of culture conditions and donor age. Tissue Engineering 2002;8(6):911-920.

321. Plachot C, Lelievre SA. DNA methylation control of tissue polarity and cellular differentiation in the mammary epithelium. Exp Cell Res 2004;298(1):122-32.
322. Jauregui HO. Cell adhesion to biomaterials. The role of several extracellular matrix components in the attachment of non-transformed fibroblasts and parenchymal cells. ASAIO Trans 1987;33(2):66-74.
323. Ben-Yosef T, Francomano CA. Characterization of the human talin (TLN) gene: genomic structure, chromosomal localization, and expression pattern. Genomics 1999;62(2):316-9.
324. Chen J, Fabry B, Schiffrin EL, Wang N. Twisting integrin receptors increases endothelin-1 gene expression in endothelial cells. Am J Physiol Cell Physiol 2001;280(6):C1475-84.
325. Gregg D, de Carvalho DD, Kovacic H. Integrins and coagulation: a role for ROS/redox signaling? Antioxid Redox Signal 2004;6(4):757-64.
326. Humphries JD, Wang P, Streuli C, Geiger B, Humphries MJ, Ballestrem C. Vinculin controls focal adhesion formation by direct interactions with talin and actin. J Cell Biol 2007;179(5):1043-57.
327. Ingber DE. Mechanosensation through integrins: cells act locally but think globally. Proc Natl Acad Sci U S A 2003;100(4):1472-4.
328. Balaban NQ, Schwarz US, Riveline D, Goichberg P, Tzur G, Sabanay I, Mahalu D, Safran S, Bershadsky A, Addadi L and others. Force and focal adhesion assembly: a close relationship studied using elastic micropatterned substrates. Nat Cell Biol 2001;3(5):466-72.
329. Meyer CJ, Alenghat FJ, Rim P, Fong JH, Fabry B, Ingber DE. Mechanical control of cyclic AMP signalling and gene transcription through integrins. Nat Cell Biol 2000;2(9):666-8.
330. Riveline D, Zamir E, Balaban NQ, Schwarz US, Ishizaki T, Narumiya S, Kam Z, Geiger B, Bershadsky AD. Focal contacts as mechanosensors: externally applied local mechanical force induces growth of focal contacts by an mDia1-dependent and ROCK-independent mechanism. J Cell Biol 2001;153(6):1175-86.
331. Power J, Mayer-Proschel M, Smith J, Noble M. Oligodendrocyte precursor cells from different brain regions express divergent properties consistent with the differing time courses of myelination in these regions. Dev Biol 2002;245(2):362-75.
332. Warrington AE, Barbarese E, Pfeiffer SE. Differential myelinogenic capacity of specific developmental stages of the oligodendrocyte lineage upon transplantation into hypomyelinating hosts. J Neurosci Res 1993;34(1):1-13.
333. Banik NL, Smith ME. Protein determinants of myelination in different regions of developing rat central nervous system. Biochem J 1977;162(2):247-55.
334. Raff MC, Miller RH, Noble M. A glial progenitor cell that develops in vitro into an astrocyte or an oligodendrocyte depending on culture medium. Nature 1983;303(5916):390-6.

335. Noble M. Implications for CNS repair of redox modulation of cell survival, division and differentiation. Curr Alzheimer Res 2006;3(1):37-47.
336. Noble M, Mayer-Proschel M, Proschel C. Redox regulation of precursor cell function: insights and paradoxes. Antioxid Redox Signal 2005;7(11-12):1456-67.
337. Oliveira LR, Jeffrey SS, Ribeiro-Silva A. Stem cells in human breast cancer. Histol Histopathol;25(3):371-85.
338. Reya T, Morrison SJ, Clarke MF, Weissman IL. Stem cells, cancer, and cancer stem cells. Nature 2001;414(6859):105-11.
339. Hwang-Verslues WW, Kuo WH, Chang PH, Pan CC, Wang HH, Tsai ST, Jeng YM, Shew JY, Kung JT, Chen CH and others. Multiple lineages of human breast cancer stem/progenitor cells identified by profiling with stem cell markers. PLoS One 2009;4(12):e8377.
340. Fillmore CM, Kuperwasser C. Human breast cancer cell lines contain stem-like cells that self-renew, give rise to phenotypically diverse progeny and survive chemotherapy. Breast Cancer Res 2008;10(2):R25.
341. Ponti D, Zaffaroni N, Capelli C, Daidone MG. Breast cancer stem cells: an overview. Eur J Cancer 2006;42(9):1219-24.
342. Nakshatri H, Srour EF, Badve S. Breast cancer stem cells and intrinsic subtypes: controversies rage on. Curr Stem Cell Res Ther 2009;4(1):50-60.
343. Park SY, Lee HE, Li H, Shipitsin M, Gelman R, Polyak K. Heterogeneity for stem cell-related markers according to tumor subtype and histologic stage in breast cancer. Clin Cancer Res;16(3):876-87.
344. Battista S, Guarnieri D, Borselli C, Zeppetelli S, Borzacchiello A, Mayol L, Gerbasio D, Keene DR, Ambrosio L, Netti PA. The effect of matrix composition of 3D constructs on embryonic stem cell differentiation. Biomaterials 2005;26(31):6194-207.
345. Costa-Pinto AR, Salgado AJ, Correlo VM, Sol P, Bhattacharya M, Charbord P, Reis RL, Neves NM. Adhesion, proliferation, and osteogenic differentiation of a mouse mesenchymal stem cell line (BMC9) seeded on novel melt-based chitosan/polyester 3D porous scaffolds. Tissue Eng Part A 2008;14(6):1049-57.
346. Gerlach JC, Hout M, Edsbagge J, Bjorquist P, Lubberstedt M, Miki T, Stachelscheid H, Schmelzer E, Schatten G, Zeilinger K. Dynamic 3D culture promotes spontaneous embryonic stem cell differentiation in vitro. Tissue Eng Part C Methods;16(1):115-21.
347. Li J, Tao R, Wu W, Cao H, Xin J, Guo J, Jiang L, Gao C, Demetriou AA, Farkas DL and others. 3D PLGA scaffolds improve differentiation and function of bone marrow mesenchymal stem cell-derived hepatocytes. Stem Cells Dev.
348. Tan KK, Aminuddin BS, Tan GH, Sabarul Afian M, Ng MH, Fauziah O, Ruszymah BH. Strategy for generating tissue-engineered human bone construct. Med J Malaysia 2004;59 Suppl B:43-4.
349. Pedersen JA, Swartz MA. Mechanobiology in the third dimension. Ann Biomed Eng 2005;33(11):1469-90.

350. Wozniak MA, Modzelewska K, Kwong L, Keely PJ. Focal adhesion regulation of cell behavior. Biochim Biophys Acta 2004;1692(2-3):103-19.
351. Mohan N, Nair PD, Tabata Y. A 3D biodegradable protein based matrix for cartilage tissue engineering and stem cell differentiation to cartilage. J Mater Sci Mater Med 2009;20 Suppl 1:S49-60.
352. Pek YS, Wan AC, Ying JY. The effect of matrix stiffness on mesenchymal stem cell differentiation in a 3D thixotropic gel. Biomaterials;31(3):385-91.
353. Yang F, Cho SW, Son SM, Hudson SP, Bogatyrev S, Keung L, Kohane DS, Langer R, Anderson DG. Combinatorial extracellular matrices for human embryonic stem cell differentiation in 3D. Biomacromolecules;11(8):1909-14.
354. Holtom GR, Thrall BD, Chin BY, Wiley HS, Colson SD. Achieving molecular selectivity in imaging using multiphoton Raman spectroscopy techniques. Traffic 2001;2(11):781-8.
355. Ogilvie JP, Beaurepaire E, Alexandrou A, Joffre M. Fourier-transform coherent anti-Stokes Raman scattering microscopy. Opt Lett 2006;31(4):480-2.
356. Zhang Y, Hong H, Cai W. Imaging with Raman spectroscopy. Curr Pharm Biotechnol 2010;11(6):654-61.

9 CURRICULUM VITAE

ER LIU
erliu@rci.rutgers.edu

EDUCATION

RUTGERS, THE STATE UNIVERSITY OF NEW JERSEY, New Brunswick, NJ
Doctor of Philosophy in Biomedical Engineering: Degree Received Jan. 2011

WUHAN UNIVERSITY OF TECHNOLOGY, Wuhan, HUBEI, CHINA
Master of Science in Biomedical Engineering: Degree Received May 2004

WUHAN UNIVERSITY OF TECHNOLOGY, Wuhan, HUBEI, CHINA
Bachelor of Science in Chemical Engineering: Degree Received May 2001

EXPERIENCE

09/2005-present Research Assistant, Department of Biomedical Engineering, Rutgers University, New Jersey

06/2006-09/2006 Summer Research Fellow, The New Jersey Center for Biomaterials, Rutgers University, New Jersey

03/2005-08/2005 Lab Researcher, Department of Biomedical Engineering, Rutgers University, New Jersey

09/2004-05/2005 Graduate fellow, Department of Biomedical Engineering, Rutgers University, New Jersey

JOURNAL PUBLICATIONS

1. Er Liu, et al. *High content imaging based mapping stem cell phenotypes*. In preparation.
2. Hak-Joon Sung, Arnold Luk, Sanjeeva Murthy, Er Liu, Malasa Jois, Abraham Joy, Jared Bushman, Prabhas Moghe and Joachim Kohn. *Poly(ethylene glycol) as a sensitive regulator of cell survival fate on polymeric biomaterials: The interplay of cell adhesion- and pro-oxidant signaling mechanisms.* Soft Matter. In Press.
3. Er Liu, Simon Gordonov, Matthew Treiser, and Prabhas Moghe. *Parsing the early cytoskeletal and nuclear organizational cues that demarcate stem cell lineages.* Cell Cycle. 9: 2108 – 2117 (2010)

4. Liu, E., M.D. Treiser, H. Patel, H.J. Sung, K.E. Roskov, J. Kohn, M.L. Becker, and P.V. Moghe, *High-content profiling of cell responsiveness to graded substrates based on combinatorially variant polymers* Combinatorial Chemistry and High-throughput Screening - Special Issue on Combinatorial and High-Throughput Screening of Cell Response to Biomaterials, 2009. **12**(6).
5. Sung, H.J., P. Chandra, M.D. Treiser, E. Liu, C.P. Iovine, P.V. Moghe, and J. Kohn, *Synthetic polymeric substrates as potent pro-oxidant versus anti-oxidant regulators of cytoskeletal remodeling and cell apoptosis.* J Cell Physiol, 2009. **218**(3): p. 549-57.
6. Liu, E., M.D. Treiser, P.A. Johnson, P. Patel, A. Rege, J. Kohn, and P.V. Moghe, *Quantitative biorelevant profiling of material microstructure within 3D porous scaffolds via multiphoton fluorescence microscopy.* J Biomed Mater Res B Appl Biomater, 2007. **82**(2): p. 284-97.
7. Treiser, M.D., E. Liu, R.A. Dubin, H.J. Sung, J. Kohn, and P.V. Moghe, *Profiling cell-biomaterial interactions via cell-based fluororeporter imaging.* Biotechniques, 2007. **43**(3): p. 361-6, 368.

PUBLICATIONS (BOOKS/CHAPTERS)

8. Er Liu, Sebastian Vega, Matt Treiser, Hak-Joon Sung, Prabhas Moghe. *Fluorescent imaging of cell-biomaterial interactions.* Editors: Ducheyne P and Kirkpatrick J, Elsevier, In Press (2010).